Ab Initio Studies on 2D Array Of Acidic Surface Groups as a Model For Polymer Electrolyte Membranes

by

Sudha P Narasimachary

M.Sc., (Chemistry), Madurai Kamaraj University, 1998
B.Sc., Madurai Kamaraj University, 1996

Thesis Submitted in Partial Fulfillment of the

Requirements for the Degree of

Doctor of Philosophy

in the

Department of Chemistry

Faculty of Science

SIMON FRASER UNIVERSITY

Fall 2014

Approval

Name: **Sudha P Narasimachary**

Degree: **Doctor of Philosophy (Chemistry)**

Title of Thesis: **Ab Initio Studies on 2D Array of Acidic Surface Groups as a Model for Polymer electrolyte membranes**

Examining Committee:

Chair: **Dr. Krzyztof Starosta**
Associate Professor

Dr. Michael H. Eikerling
Senior Supervisor
Professor

Dr. Steven Holdcroft
Supervisor
Professor

Dr. Zuo-Gang Ye
Supervisor
Professor

Dr. Barbara Frisken
Internal Examiner
Professor
Department of Physics

Dr. Perla Balbuena
External Examiner
Professor
Department of Chemical Engineering
Texas A & M University

Date Defended: August 25th , 2014

Partial Copyright Licence

Abstract

Polymer electrolyte fuel cells (PEFCs) are touted as the next generation of energy delivering devices. Within a decade, PEFC-driven powertrains are expected to become a viable alternative to internal combustion engines in vehicles. Moreover, PEFCs could provide power to a plethora of portable and stationary applications. The critical component in a PEFC is the polymer electrolyte membrane (PEM). Current PEMs require a high level of hydration in order to provide sufficient proton conduction. Of particular interest in this field is the synthesis of advanced functional membranes that could attain high proton mobility at minimal hydration and at elevated temperature (> 100ºC). At these temperatures, structural correlations and proton dynamics at acid-functionalized polymer aggregates could be vital for membrane operation. Theoretical predictions should guide the efforts in the design of advanced PEMs. Our model system consists of a minimally hydrated interfacial array of acid-terminated surface groups. The density of these surface groups is the main variable parameter of the model; moreover, we have evaluated different chemical architectures of surface groups. We have employed ab initio calculations based on density functional theory to study interfacial energies, structural correlations and transitions in the hydrogen bonded network of hydronium ions and protogenic surface groups.

The first part of this thesis focuses on rationalizing the effect of various parameters of highly acid-functionalized interfaces in PEMs, such as density, chemical architecture, and conformational flexibility of acidic surface groups on interfacial structural correlations and transitions. At high surface group density and under minimal hydration, with one water molecule per surface group, sulfonic acid head groups are perfectly dissociated. They assemble into a highly ordered condensed surface state with two sublattices; one of them is formed by hexagonally ordered sulfonate anions; the other sublattice corresponds to interstitial hydronium ions. Sulfonate anions and hydronium ions form a hydrogen bonded network. The saturation of hydrogen bonds renders the network in a superhydrophobic state. Lowering the surface group density triggers a sequence of transitions to states with decreasing long range order, decreasing the number of interfacial hydrogen bonds and the degree of dissociation. Moreover, the interface becomes hydrophilic. The same sequence of transitions was found for arrays with varying length and chemical structure of surface groups. These findings emphasize the importance of 2D correlation effects at polymer-water interfaces in PEMs. The second part of the thesis focuses on the impact of a second monolayer of water molecules on stability, interfacial structural correlations and and transitions of the hydrated array of acidic surface groups. Upon increasing the surface group spacing, the bonding energy of additional water increases, undergoing a transition from superhydrophobic to hydrophilic wettability. At sufficiently large surface group separation, a hydronium ion is seen to transfer from the minimally hydrated interfacial network to the second water layer, where it is then observed to form a Zundel ion.

Keywords: polymer electrolyte fuel cells; minimally hydrated array of protogenic surface groups; *ab initio* molecular dynamics; density functional theory; structural correlations and transitions at interface.

Dedication

In the Memory of the late Mr. A. R. Seshadri.

Acknowledgements

First and foremost, I would like to express my deepest gratitude to my senior supervisor, Prof. Dr. Michael Eikerling for his support and insight while pursuing my degree. I am very thankful for all the opportunities he provided me with, such as presenting at international conferences and poster competitions in our department, as well as for supporting me through many assistantships. With very good supervision and a friendly attitude, he made me feel very lucky throughout my studies.

I would like to thank my supervisory committee members, Prof. Dr. Steven Holdcroft and Prof. Dr. Zuo-Gang Ye, for their constructive criticism.

I would like to express my gratitude to Dr. Ata Roudgar, with whom I started this project and who guided me in my learning the computational methods. Without him I would never have known VASP and CPMD. I would like to thank all members of my group for their kind nature and friendly attitude.

This thesis would not be possible without the emotional support of my husband, Madhu at very hard times in my life.

I am thankful to my family who encouraged me, provided me with a good environment, strength and instilled positive attitude that made me to complete the studies during the hard times in my life.

Finally yet importantly, I would like to thank Dr. Ana Siu for proof reading my thesis and providing valuable advice.

Table of Contents

List of Tables

List of Figures

List of Symbols

c^{a}_{ox}	Concentration of oxidized species in bulk solution (mol L^{-1})
c^{a}_{red}	Concentration of reduced species in bulk solution (mol L^{-1})
D	Diffusion coefficient (cm^2s^{-1})
E^{eq}	Equilibrium electromotive force (V)
E^{0}	Electrode potential (V)
E^{uc}_{f}	Formation energy per unit cell (eV)
F	Faraday constant, 9.648 533 99 24 × 10^4 (C mol^{-1})
ΔG	Gibb's free energy of reaction (kJ mol^{-1})
ΔH	Enthaply of reaction (kJ mol^{-1})
IEC	Ion exchange capacity (meq mol^{-1})
R	Molar gas constant (8.314 J K^{-1} mol^{-1})
RH	Relative Humidity
T_g	Glass transition temperature
$\left\|Y_{lm}\right\rangle$	Spherical harmonics
$\left\|lm\right\rangle$	Eigen state of the atomic pseudo-Hamiltonian
$\hat{V}_{loc}$	Local pseudopotential (operator)
$\hat{V}_{SL}$	Semi-local pseudopotential (operator)
$\hat{V}_{KB}$	Kleinman-Bylander pseudopotential (operator)
V_{eff}	Effective potential (eV)
φ_P	Polymer volume fraction
φ_W	Water volume fraction

Greek Symbols

λ	Water content in the membrane (ratio of moles of water to moles of sulfonic acid groups)
σ	Proton conductivity (Scm^{-1})
γ	Thermal efficiency of energy conversion device
ε	Microscopic swelling parameter
η	Overpotential
β	Specific surface area per polar group
π	Surface Pressure
δΔV	Ellipsometry angle

Chapter 1. Introduction

1.1. Global Energy Challenge

Over the past century, seemingly unlimited resources and ever-increasing production of fossil fuels such as coal, petroleum and natural gas have spurred economic growth in industrialized countries. The burning of fossil fuels has supplied energy to factories, homes and vehicles. Over the same period, it has been observed that atmospheric pollution levels have increased and the global warming phenomenon has been stipulated as a major global concern. In particular, the proposed correlations between rising global temperature and the increased rate of release of CO_2 and other greenhouse gases into the atmosphere caused major concern and heated debates at all levels of society.

The looming depletion of cheap oil as well as escalating concerns over the global energy and climate challenges drive major efforts in research and development of alternative energy sources and infrastructures. At the same time, energy supply has to keep pace with population and economic growth. The development of a highly efficient and sustainable energy infrastructure and society that could address these challenges hinges on scientific progress and the introduction of innovative technologies.

There is a widespread consensus that in the future energy supply will rely on a mix of conventional sources as well as, increasingly, renewable sources, including solar, wind, geothermal, hydro, and bio mass energy generation. A common global goal is to reduce the carbon footprint of the energy input for electricity generation and transportation applications. Alternative technologies should rely on earth-abundant materials and they should be cost-competitive with incumbent technologies. In this regard, a technology that has received tremendous attention over the last decades and

that is nowadays rapidly moving towards commercialization is fuel cell technology which is a type of electrochemical energy conversion device.

The unique advantage of electrochemical energy conversion devices such as fuel cells over thermal energy conversion lies in the higher thermodynamic efficiency. Fuel cell technology has gained attention and support around the world in past decades due to the advantages provided by electrochemical energy conversion, the anticipated positive impact on environment, and the expected large market potential of electric devices and vehicles powered by fuel cells. There are many types of fuel cells available that are distinguished by their electrolyte, operating temperature and fuel. One of the most promising fuel cell technologies for transportation, power supply to laptops, cellphones etc, is low temperature polymer electrolyte fuel cell.

In this chapter, the main focus will be on giving an overview of previous modelling works done in various groups and lack in understanding proton transport mechanism in polymer electrolyte membranes at minimal hydration condition. Before going into the details of other works, I first would like to introduce main concepts pertaining to polymer electrolyte fuel cell.

1.2. Polymer Electrolyte Fuel Cell Technology

Developments in solid polymer electrolyte fuel cell technology for transportation and stationary applications have been rapid in the last 20 years. PEFC convert hydrogen and oxygen into water according to the chemical reaction

$$H_2 + {}^{1}\!/\!_{2} O_2 \rightarrow H_2O \qquad \textbf{1.1}$$

The thermodynamic efficiency γ, of an energy conversion device is defined as the ratio of the Gibbs free energy of the reaction ΔG, which is the maximum amount of work that could be extracted from it, to the enthalpy of the reaction, ΔH

$$\gamma = {}^{\Delta G}\!/\!_{\Delta H}. \qquad \textbf{1.2}$$

The difference $T\Delta S = \Delta H - \Delta G$ is released as heat. A fuel cell harvests the Gibbs free energy as electrical energy by inserting an electrical device between negative and positive electrodes, equivalent to the function of a battery. The highest practical efficiency is attained under near open circuit conditions (OCV). The maximum electrical work, W_{el} obtainable in a fuel cell operating at constant pressure and temperature is given by ΔG,

$$\Delta G = W_{el} = -nFE^{eq}. \qquad \textbf{1.3}$$

The value of the maximal theoretical efficiency depends on the type of reactants, their concentrations or partial pressures, and the temperature. The Nernst equation relates these quantities to the fuel cell voltage,

$$E^{eq} = E^{O} + RT/2F \ln\left(p_{H_2}/p_{H_2O}\right) + RT/2F \ln\left[p_{O_2}^{1/2}\right]. \qquad \textbf{1.4}$$

If the reactants and products are in the standard state, then

$$\Delta G^{o} = -nFE^{o}, \qquad \textbf{1.5}$$

where E^{o} is the standard equilibrium cell voltage, obtained for standard conditions and concentrations of reactants. Furthermore, R is the molar gas constant, F is the Faraday constant ($9.64853399 * 10^{4}$ C mol^{-1}) and n is the number of electrons transferred in the overall reaction. The combined parameter RT / F that appears in many electrochemical equations has a value of 25.6 mV at 25°C (298.15 K). The standard equilibrium voltage of a cell operating reversibly on pure hydrogen and oxygen is $E^{0} = 1.299$ V.

The voltage efficiency of the ideal fuel cell V_{ideal} is expressed as the ratio of operating cell voltage, V_{actual} to the ideal cell voltage. The practical efficiency based on the higher heating value of hydrogen is given by

$$\gamma_{real} = \Delta G/\Delta H * V_{actual}/V_{ideal}. \qquad \textbf{1.6}$$

The voltage V_{actual} at a specific current density determines the fuel cell efficiency. Decreasing the current density increases the cell voltage, thereby increasing the fuel cell efficiency. In order to generate power densities of 1 – 2 Wcm^2, the electrical device needs to draw a current density per unit fuel cell surface area in the order of j = 1 Acm^2 [1] .

Operation of PEFCs at these current densities incurs a number of irreversible voltage losses, caused by Ohmic losses of electron and proton transport in conducting media, mass transport losses due to reactant supply through porous media and electrokinetic losses due to the required activation of electrocatalytic processes at metal|electrolyte interfaces. Overpotential losses and the corresponding voltage efficiency of the cell depend on external conditions and the operating current density, as well as on the structure and properties of materials used in the cell and the overall cell design.

Under operation at current densities in the range of 0.2-1.0 Acm^{-2}, cell voltages between 1V and 0.5V are achieved. In order to increase voltage and power output of a PEFC, single cells are connected in series to form fuel cell stack. Under identical conditions for each cell in the stack of N cells the stack voltage is N times the single cell voltage and the stack power density is N times the single cell power density. Voltage and power density of single cells and stacks are functions of the current densities, $E(j_0)$ and $P(j_0)$, which depend on layout of cells and stacks, the structure and properties of materials, as well as the operating conditions. Power density is given by:

$$P = j_0 * V_{actual} \qquad \textbf{1.7}$$

1.3. Layout of Polymer Electrolyte Fuel Cells

The layout of a polymer electrolyte fuel cell (PEFC) is shown schematically in Figure 1.1. This cell design employs a solid proton conducting polymer electrolyte membrane (PEM) [2]. The operating temperature of this type of fuel cell is 30-80°C. It was first developed in the 1960s for the NASA Gemini program. Voltage efficiencies for this type of fuel cell are in the range of 50-70 %. The advantages of using low temperature PEFCs are fast start

up times and high power densities. Fuel cells have two electrodes, one positive electrode, the cathode, along with gas diffusion layers (GDLs) and flow fields (FFs) and one negative electrode, the anode with a similar layout [4] Sandwiched between the electrodes is the proton-conducting PEM in PEFCs.

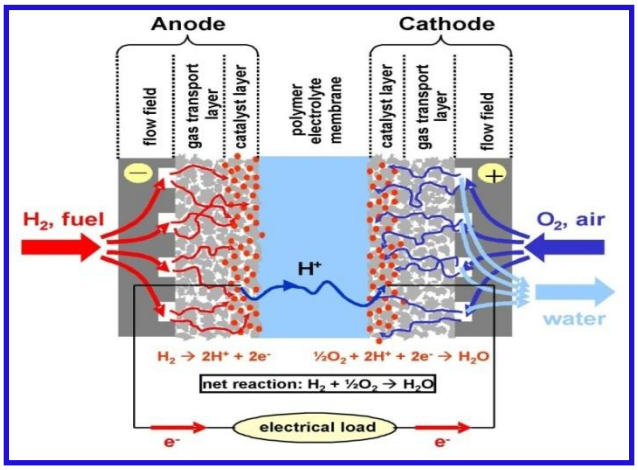

Figure 1.1: Principal lay-out and operation of a polymer electrolyte fuel cell.

At the anode, hydrogen or hydrocarbon-based fuels are supplied through FF and porous media to the anode catalyst layer (ACL), where the hydrogen gas is oxidized in the hydrogen oxidation reaction (HOR). The generated protons and electrons travel via PEM and external circuit, respectively, to the cathode catalyst layer (CCL). At the cathode, oxygen is supplied through FF and porous media to perform the oxygen reduction reaction (ORR) at the cathode catalyst layer (CCL), by combination with protons and electrons. The overall reaction produces water and it releases heat and electricity. The half reactions at anode and cathode are

$$H_2 + \frac{1}{2}O_2 \rightarrow H_2O_{(l)} \ , \qquad E^o = 0 \ , \qquad \textbf{1.8}$$

$$4H^+ + O_2 + 4e^- \ \rightarrow \ 2H_2O \ , \qquad E^o = 1.299 \text{ V (SHE)} \ , \qquad \textbf{1.9}$$

Despite many successful demonstrations of polymer electrolyte fuel cell technology, commercialization of the same still poses numerous challenges to be addressed. Major practical concerns are related to (i) the cost of materials, (ii)

elimination of fluoride to decrease metal plate corrosion problems, thus enabling the use of more affordable plate materials, as well as (iii) the need for polymer electrolyte membranes with improved conductivity at low relative humidity, enhanced lifetime, and high durability.

Although thinner membranes (20-30 μm) enable high power density, the requirements on their chemical and mechanical stability are significantly demanding compared to those imposed on thicker membranes (~200 μm). Standard polymers used in PEFCs are made from perfluorosulfonic acid (PFSA) ionomers are chemically stable; yet, they are known to degrade in the fuel cell via radical attack [3]. The mechanism of chemical degradation of PFSA ionomers depends on several factors including chemical structure, catalyst components, relative humidity and temperature, to name a few.

PEFC typically use Pt to catalyze the HOR. The Pt loading on the anode side could be reduced to 0.05 mg cm^{-2} due to the fast kinetics of the H_2 oxidation reaction at Pt-based catalysts. However, the sluggish oxygen reduction reaction (ORR) on the cathode side demands Pt loadings of 0.4 mg cm^{-2} to meet the performance target of 0.7 V for the fuel cell voltage at a current density of 1 A cm^{-2} and attain a power density of 15-2.0 kW L^{-1}. In order to achieve the target of the specific Pt mass of 0.2 g kW^{-1}, the Pt demand at the cathode must be reduced to 0.1 mg cm^{-1}. For this purpose, better cathode catalysts are being developed. Platinum cobalt and other Pt alloys yield an activity improvement by a factor of 2 compared to carbon-supported Pt; the use of such catalysts enables lowering of the cathode Pt loading to 0.1 mg cm^{-1} with an additional voltage loss of less than 20 mV. The specific Pt mass could be reduced to 0.19 g kW^{-1}, bringing down the catalyst cost to roughly $7 per kW [4]. The durability of Pt-alloy catalysts under automotive conditions is yet to be demonstrated. In summary, the currently used PFSA-type membranes and Pt-based catalysts are in principle able to meet the performance targets for high volume automotive applications. To enable fuel cell commercialization, further materials improvements and an enhanced understanding of the pertinent degradation mechanisms are needed.

1.4. Thermodynamic Principles and Overpotentials

The energy conversion and power density characteristics of fuel cells follow directly from the thermodynamic and kinetic formulations for chemical reactions as adapted to electrochemical reactions. Useful electrical work is obtained from a fuel cell only when a reasonable current is drawn, whereby the actual cell potential decreases from the equilibrium potential (E_{eq}) to the real potential (E). The difference between E and E_{eq} is known as overpotential losses or polarization losses,

$$E_{eq} - E = \eta$$

or

$$E = E_{eq} - \eta. \qquad \textbf{1.10}$$

Different sources contribute to the total loss, η. These losses are depicted in Figure 1.2 which shows a plot of fuel cell voltage vs. current density. For the electrode surface processes, η is related to the current density, j, through the Butler-Volmer equation, which reads in oversimplified form,

$$j = j^0 \bullet \left\{ \exp\left[\alpha \frac{nF\eta}{RT}\right] - \exp\left[(1-\alpha)\frac{nF\eta}{RT}\right] \right\}. \qquad \textbf{1.11}$$

Polarization is really a physical property, but used indefinitely. In most cases it means the voltage difference between metal electrodes in an electrochemical cell.

The first and second terms in the bracket of Equation 1.11 correspond to anodic and cathodic current contribution to the overall reaction current at the electrode. The exchange current density j^0 and the electron transfer coefficient α are kinetic parameters in the Butler-Volmer equation.

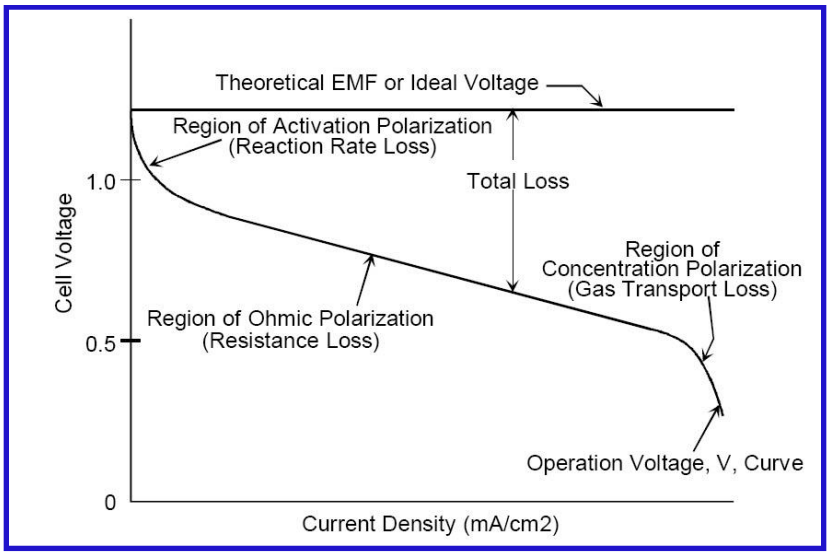

Figure 1.2: Ideal and actual fuel cell voltage-current characteristics. Adapted from Fuel Cell Handbook, Fourth edition, U. S. Department of Energy, 1998.

The main voltage loss contributions stem from (i) activation polarization or losses (η_{act}), (ii) resistance polarization or losses (η_{ohm}), (iii) concentration polarization or mass transport losses (η_{conc}).

Activation losses

The activation loss is dominant at low current density (1-100 mA^2). Activation losses increase with the current density. This type of polarization occurs when the rate of an electrochemical reaction at an electrode surface is controlled by electrode kinetics. There is a close similarity between electrochemical and chemical reactions in that both involve an activation barrier that must be overcome. In an electrochemical reaction, the activation barrier decreases by a value that is proportional to the overpotential

$$\Delta G_{act}(\eta) = \Delta G^{0}_{act} - \alpha F \eta \qquad \textbf{1.12}$$

The Tafel equation for voltage losses due to activation polarization is given by,

$$\eta_{act} = \frac{RT}{\alpha\, n\, F} \ln \frac{j}{j^0} \qquad \textbf{1.13}$$

For the cathode, we have,

$$\eta_{act,c} = -\frac{RT}{(\alpha_{red,c})\, n\, F} \ln \frac{j}{j^0}, \qquad \textbf{1.14}$$

and for the anode we have to use both the terms in Equation 1.11.

$$\eta_{act,a} = -\frac{RT}{(\alpha_{ox,a})\, n\, F} \ln \frac{j}{j^0},$$

where α is the electron transfer coefficient of the electrode (either cathode or anode). For a hydrogen-oxygen fuel cell, the cathode activation losses $\eta_{act,c}$ are dominant and hence anode activation losses $\eta_{act,a}$ are generally neglected.

Tafel plots are used to find the exchange current density. Since, Equation 1.13 can be rewritten in the form

$$\eta_{act} = a + b \log j,$$

where

$$a = -\frac{2.3RT}{anF} \log j^0. \qquad \textbf{1.15}$$

The exchange current density can be obtained from a plot of $\log j$ vs. η_{act} as the intercept with the ordinate ($\eta_{act} = 0$). The term b is the Tafel parameter and is obtained from the slope of this plot. A typical Tafel plot is given in Figure 1.3. For an electrochemical reaction, the Tafel slope is about 100 mV per decade at room temperature. Thus, a tenfold increase in current density causes an increase by ~ 100 mV in activation polarization. Other processes that give rise to activation losses include,

adsorption of reactant species, transfer of electron across the double layer, desorption of product species, and nature of electrode surface.

Resistance or Ohmic losses (η_{ohm})

Ohmic or resistance losses occur because of resistance to the flow of ions in the electrolyte and of electrons in the solid electrode materials. Ohmic losses are proportional to the current density. The Ohmic loss of the electrolyte can be reduced by decreasing electrode separation or by enhancing the ionic conductivity of the electrolyte. The drop in potential due to Ohmic losses in the electrolyte is expressed by the equation

$$\eta_{ohm} = jR, \qquad \textbf{1.16}$$

where R is the total ohmic resistance.

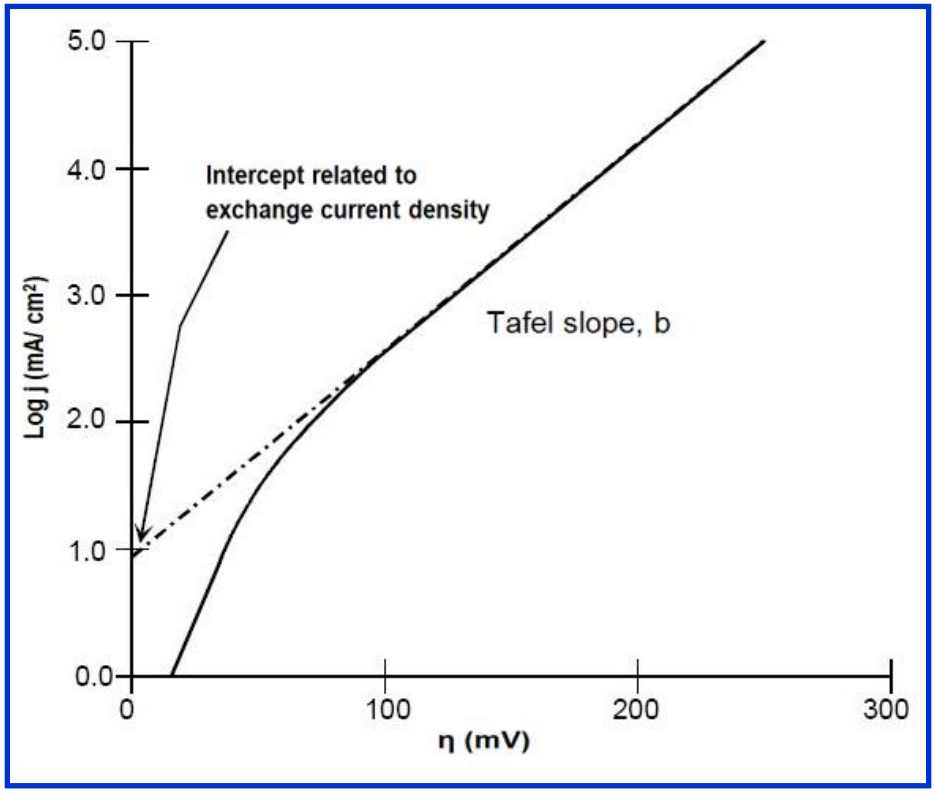

Figure 1.3: Sample Tafel plot. Adapted from Fuel Cell Handbook, Fifth edition, U. S. Department of Energy, 2000.

Concentration losses (η_{conc})

As the reactant is consumed at the electrode by the electrochemical reaction, there is a loss of potential due to the inability of the porous diffusion medium to maintain the bulk concentration. A concentration gradient forms that causes the concentration polarization. At practical current densities, slow transport of reactants/products to/from the electrochemical reaction site is a major contributor to polarization losses. Fick's first law relates the diffusive flux to the concentration under the assumption of steady stateAt electrodes, the rate of mass transport to an electrode surface can be described by Fick's first law of diffusion, which is given in finite difference approximation. For planar layer with thickness δ,

$$j_{diff} = \frac{nFD(C_B - C_S)}{\delta}, \qquad \textbf{1.17}$$

where D is the diffusion coefficient of the reacting species, C_B its bulk concentration, C_S its surface concentration, and δ the thickness of the diffusion layer. The diffusion limited current density j_L is a measure of the maximum rate at which a reactant can be supplied to an electrode. Assuming C_S= 0, one gets,

$$j_L = \frac{nFD(C_B)}{\delta} \qquad \textbf{1.18}$$

1.5. Water Management in Polymer Electrolyte Fuel Cells

Water management is crucial to performance of PEFCs. Too much water will flood the cell, too little will dry it; in both cases, power output will drop. Water management is a very difficult subject in PEM systems, primarily because water in the membrane is dragged toward the cathode of the cell at high relative humidity. Maintaining the optimal hydration of the membrane requires additional water management, adding cost and complexity to the fuel cell system.

Water is generally assumed to exist in three distinguishable states in PEFCs.

I. Water absorbed by the membrane.

II. Liquid water in the electrodes.

III. Water vapor.

Water absorbed by the membrane: Maintaining a sufficient level of hydration is mandatory for good PEM performance. This demands proper water management inside the operating PEFC. Under operation, a non-uniform water concentration profile inside the membrane is due to the so-called electro-osmotic drag effect [5]. This effect involves the transport of water molecules along with protons that migrate from anode to cathode. The corresponding electro-osmotic water flux density is proportional to the proton flux density. Therefore, as the fuel cell current density is increased the electro-osmotic flux density increases as well. This coupling leads to the membrane dehydration on the anode side. It could moreover lead to water accumulation in the cathode, resulting in cathode flooding, if efficient water removal is not achieved. Because of the water content gradient between anode and cathode that establishes due to electro-osmotic drag a water back flux from cathode to anode is generated by hydraulic permeation that partially compensates the electro-osmotic flux, Figure. 1.4. Refer [6] for the figure below.

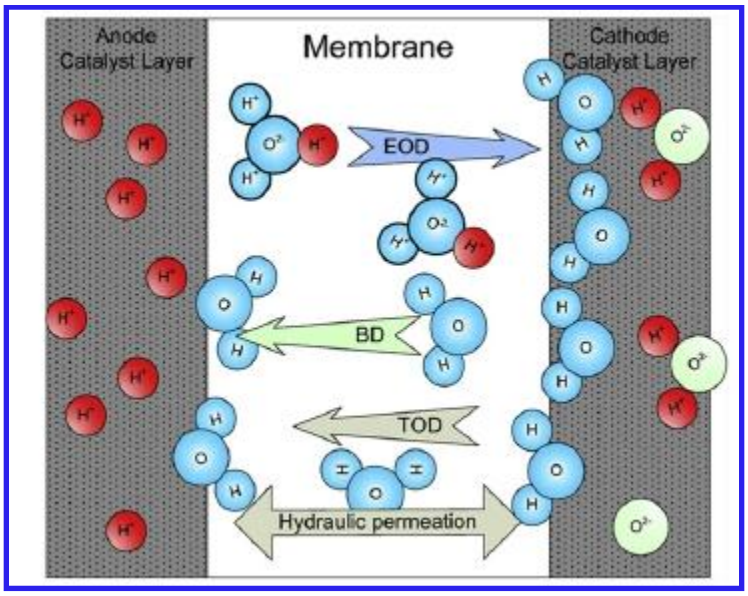

Figure 1.4: Various modes of water transport in proton exchange membrane, Electro osmotic drag (EOD), Back diffusion (BD) and Thermal osmotic drag (TOD) are depicted. Adapted from Wei Dai, Haijiang Wang, Xiao-Zi Yuan, Jonathan J. Martin, Daijun Yang, Jinli Qiao,and Jianxin Ma, Int. *J. hydrogen energy,* 2009, 34, 9461 with permission. International Association of Hydrogen Energy. Copyright 2009.

At high current densities, the water content at the anode side of the PEM drops to a threshold value, known as the percolation threshold, below which the proton conductivity dramatically decreases corresponding to a strong increase in the Ohmic resistance of the PEM. It is therefore a major challenge for membrane design and optimization of operating conditions to maintain a sufficient level of hydration for the target range of current densities.

One method of improving water management is to pass humidified gases through the electrodes. This can be done by passing cooling water through integrated stack of humidified gases or by using membranes with wicks [7, 8]. Several membranes were synthesized in order to reduce the electro-osmotic drag while maintaining an acceptable level of conductivity. Nafion doped with phosphoric acid [9] and phosphoric acid doped poly benzimidazole (PBI) [10] and was found to exhibit conductivity of 0.01 S cm^{-1} at room temperature and a value of 0.26 S cm^{-1} at 200°C with suppressed electro-osmotic drag.

Liquid water in porous electrode layers (CCL, MPLs, and GDLs): Accumulation of liquid water (flooding) is generally a concern on the cathode side due to the production of water there. Evaporation transforms liquid water into water vapour. A high rate of vaporization is desirable in view of alleviating the flooding problem as well as removing heat in the form of latent heat of water vapour. On the anode side, dehydration is of greater concern as water is available only from the humidified hydrogen stream or from back transport of water from the cathode side.

Water vapour within the gas streams: In a mixture of gas and water vapour, the amount of water vapour is determined by its partial pressure, which cannot exceed the saturation vapour pressure of water at the mixture temperature. Decrease in the temperature or increase in the humidity ratio of the gas stream due to either depletion of the reactants or introduction of water vapour from the electrochemical reaction beyond the saturation limit, results in flooding of the pore space.

1.6. Objectives and Motivation of the Thesis

Membranes that could provide high rates of proton transport with very low amount of water are of particular interest for PEFC technologies that need to provide high power density, as required by the automotive industry. Current PEMs depends entirely on bulk-like water content in order to provide desired proton conductivity. This motivates vast research in experimental synthesis and characterization of novel PEMs [11, 12] that are suitable for operation at high temperature ($T > 90^{\circ}$ C) and at low relative humidity in order to attain high rates of proton transport with minimal amount of water that is tightly bound to stable host polymer [13-15]. Thus, a better understanding of proton and water transport phenomena is required under these conditions. Various computational methods were employed in order to understand the structure and properties of water in swollen membranes and in particular Nafion® membranes that include quantum mechanical [16-18], classical [19-27] and coarse grained simulations [28-30]. Quantum mechanical simulations focused on simulating systems under minimal hydration condition utilized either an experimental studied crystal structure such as trifluoromethane sulfonic acid mono hydrate [188]. Such regular structures formed the proper basis for studying controlled *abinitio* molecular dynamic simulations.

Rearrangement of neighboring sulfonate groups led to the formation of an activated state with activation energy ~0.3 eV. These calculations suggested that an approxiamate flexibility of anionic side chains could be vital for high proton mobility in PEMs under conditions of minimal hydration and high anion density. However, in this crystal, both the composition and number of water molecules are fixed, implying only minimal hydration could be considered.

Molecular level simulations in PEM based on density functional theory utilized by Elliott and Paddison in different papers [18, 31, 32] in order to study side chain correlations and examine direct proton exchange between water of hydration and surface groups. These calculations included several side chains attached to a single polymer backbone. They however did not include correlation effects of side chains in the interface that arise in 2D conformations.

Car-Parrinello molecular dynamics study and path integral formalism of CPMD utilized by the group of Hayes *et al* [198, 199] in order to simulate the trifluoromethane sulfonic acid in mono hydrate, di and tetrahydrate systems that revealed quantum effects that facilitate proton transfer to “presolvated” water or sulfonic acid in the first solvation shell and favour the formation of Zundel ion ($H_5O_2^+$) in all the defects studied. Long range proton transport in these systems was not observed due to the imposed constraints.

In view of the development of new PEM materials, it is of primary interest to understand the interactions between ionomer material and water. This defines a need for studies at the molecular level that aim to rationalize the impact of ionomer chemistry and self-organized ionomer structures on acid dissociation, proton distribution and proton transport mechanisms. For this purpose, we have introduced a model that consists of a 2D hexagonal array of protogenic surface groups. The model system is versatile in that it allows varying important chemical structural parameters like density of surface groups, SGs, length of side chain, as well as the degree of hydration of the interfacial array. In this thesis, we studied the effect of chemical groups, length of the side chains, and increasing state of hydration using our model system. We utilize *abinitio* calculations based on density functional theory to study structural correlations and transitions in PEM

at minimal hydration. We also provided elementary mechanism of proton transfer in this model system.

In this thesis, chapter 2 will focus on design of new membrane materials and transport properties of PEM. The main focus of the chapter 3 will be on PT in the PEM type membranes and in bio-membranes, chapter 4 will discuss about our model system and parameters, while chapter 5 focuses on computational methodologies utilized in our calculation and chapter 6 will provide the results of the simulation and conclusion and outlook form the chapter 7.

Chapter 2. Structure, Properties and Design of PEM

2.1. Transport Properties of PEM

The main type of PEM developed and utilized over the last 50 years are perfluorinated sulfonic acid (PFSA) ionomers like Nafion®, invented at E. I. Dupont de Nemours® [33-35]. Nafion® reaches a conductivity of $\sigma \approx 0.1$ Scm^{-1} at room temperature and when $\lambda > 15$ where λ is defined as the ratio of the number of moles of water molecules to the number of moles of sulfonic acid groups in the sample [36]. PFSA-type PEM requires sufficient hydration in order to maintain their conductivity. Evaporation of water at temperatures > 90º drastically diminishes the proton conductivity. The effect of hydration on the conductivity of Nafion®117 is depicted in Figure 2.1.

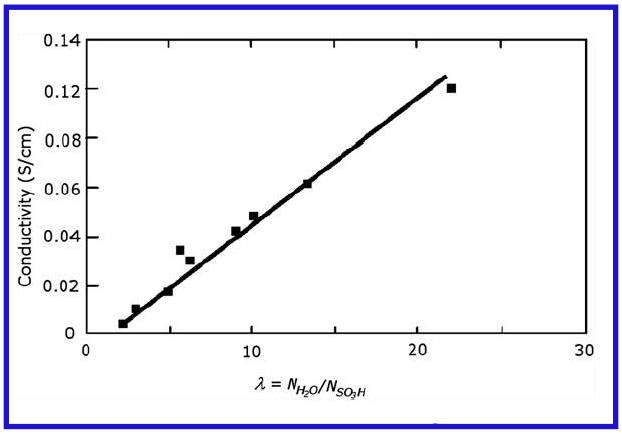

Figure 2.1: Conductivity of Nafion® at 30°C as a function of λ adapted from T. A. Zawodzinski Jr., C. Derouin. S. Radzinski, R. J. Sherman, V. T. Smith, T. E. Springer and S. Gottesfeld, *J. Electrochem. Soc*., 1993, 140, 1041. Reproduced with permission from Electrochemical Society. Copyright 1993.

At a given value of λ, the conductivity increases with T, following Arrhenius type dependence, as depicted in Figure 2.2 [37].

PFSA ionomer membranes, including the famous Nafion® produced by DuPont® and similar perfluorinated ionomer materials, meet most of the requirements of fuel cell developers [33-35]. The perfluorinated ionomer backbone confers a high chemical stability to these membranes. The backbones have perfluoroether sidechains attached to them that are terminated by sulfonic acid groups, as shown in Figure 2.3. These acid groups impart hydrophilic characteristics.

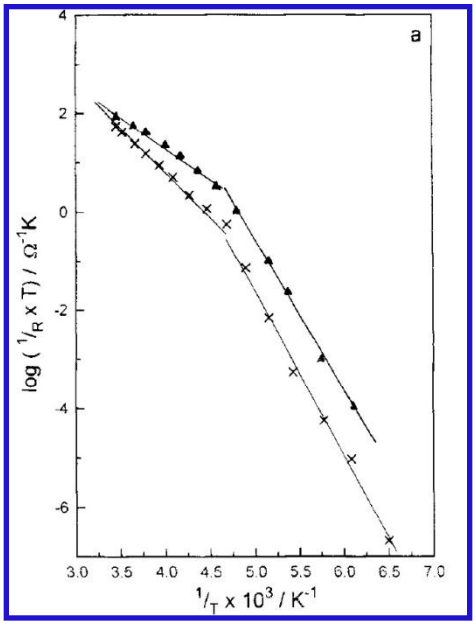

Figure 2.2: Arrhenius plot of conductance for Nafion®117 for λ=0 (x) and λ=4.5 (triangles) Reprinted from M. Cappadonia, J. W. Ering Seyedeh M. Saberi Niaki, and U. Stimming, *Solid State Ionics* 1995, 77, 65. Copyright (1995) with permission from Elsevier.

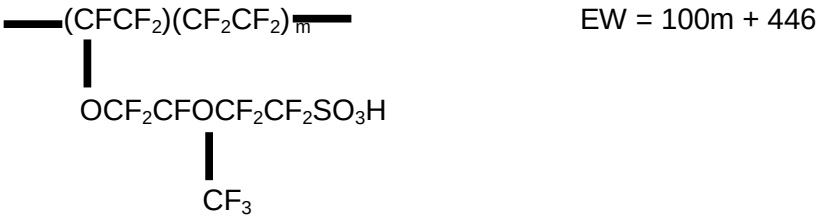

Figure 2.3: Chemical structure of Nafion®

The ion exchange capacity (IEC), is the multiplicative inverse of the equivalent weight (EW) of the membrane,

$$IEC = 1 / EW, \qquad \textbf{2.1}$$

where the equivalent weight is the number of grams of dry Nafion® per mole of sulfonic acid groups. The most commonly used Nafion® membrane has an equivalent weight of 1100 $gmol^{-1}$ with m = 6.5. Similar perfluorinated ionomers are being produced by Asahi chemicals under the brand name Aciplex® and by Asahi Glass under the name Flemion®. Dow chemical's produced a membrane which was very similar in chemical structure to Nafion® but with a shorter sidechain. Instead of two ether oxygens as in Nafion®, it contain only one ether oxygen. Recently Solvay Solexis manufactured a new ionomer under the trade name Aquivion® formerly known as "Hyflon Ion" which is similar in structure and properties to the Dow® membrane [38]. All of these PFSA-type ionomer membranes have a similar chemical architecture and morphology in the hydrated state.

2.2. Morphological Models of Nafion® from Scattering Studies

In the past decades, a wealth of information pertaining to the morphology of Nafion® has been reported in order to define accurately the molecular organization. Although the quality and quantity of data from state-of-the art scattering studies have grown tremendously, a universally accepted morphological model of Nafion® is yet to be defined. Earlier work by Gierke and co-workers in 1981 [39-41] formed the basis for explaining transport of protons and water based on small-angle X-ray scattering (SAXS) studies. They inferred that clusters of sulfonate-terminated perfluoroalkylether groups

form inverted micelles with diameters of ~40 Å. Clusters were considered to be connected by channels with diameter of 10 Å, as illustrated in Figure 2.4. Following Gierke's cluster network model many extensive studies were carried out and alternate morphologies for Nafion® were proposed.

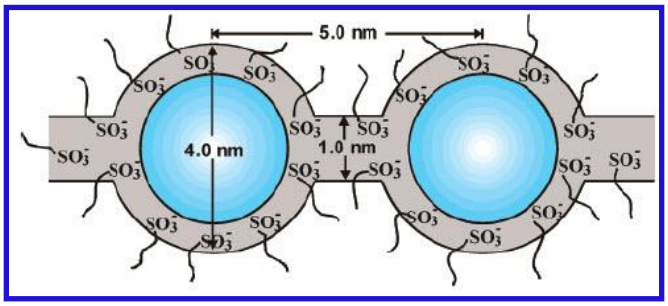

Figure 2.4: Cluster network model proposed by Hsu and Gierke. Adapted with permission from W. Y. Hsu, and T. D. Gierke *J. Membr. Sci*., 1983, 13, 307. Copyright 1983. Elsevier.

At the same time as Gierke's model, Yeager et al [42] proposed a three-phase model, shown in Figure 2.5. In contrast to Gierke's model, Yeager's model of ionic clusters did not presuppose a strict geometrical ordering and there is a transitional region of interphase between microcrystalline fluorocarbon backbone and ionic clusters of sulfonate anions, water and cations. These three phases are supposed to be (A) a hydrophobic region that is partially crystalline that consists of fluorocarbon backbone (B) an interfacial region between region A and C that consists of pendant side chain and lone ion pairs that are not part of ionic aggregates and (C) a hydrophilic region made up of ionic aggregates of the sulfonate exchange site that contains most of the absorbed water and counter ions.

Roche et al [43, 44] studied the physical properties of Nafion® membranes using small-angle neutron scattering (SANS) and small-angle X-ray scattering (SAXS) in acid as well as in salt forms. Three scattering peaks were noticed in the as received state of Nafion® assigned respectively to a crystalline phase, ionic phase and an inhomogeneous phase that is similar to Yeager's three phase model. The acid form of the membrane exhibited two scattering peaks.

The first peak at lower scattering angles with Bragg spacing of 180 Å was assigned to the interference between crystalline structures in membranes. The second peak at higher scattering angles was thought to arise from ion-containing regions swollen with water. Nafion® was swollen with mixtures of H_2O and D_2O to enhance the ionic scattering peak features. They also used quenched samples to eliminate features pertaining to crystalline regions. Utilizing SAXS, they could study the enhancing features of the second peak at lower scattering angles upon increasing the water content. The origin of the so-called ionomer peak was explained using an intra-particle scattering model, in which the scattering maximum is due to the characteristic distance between structural elements inside the membrane.

Various morphological models [45, 46] were proposed based on the scattering studies, that includes a twophase model proposed by Cooper et al [47] a core-shell model from Stein, MacKnight *et al* [48, 49], Starkweather's bilayer hexagonally packed planar zigzag chain model using oriented fiber samples [50], Kumar and Pineri's non-interacting hard sphere model [51] and a local order model from Dreyfus *et al* [52]. Lee et al in his model suggested that predominant interactions at low water content is between acid functionalized head groups (SGs) and water using both small and wide angle X-ray diffraction studies.

Predominant interactions between acidic surface groups and water at low content were propsed from the model of Lee *et al* [53]. The nature and structure of Nafion® in water and in ethanol was studied by Aldebert *et al* [54] using SANS studies. They utilized Nafion® with low ion exchange capacity or high equivalent weight membranes. The distance between scattering object, d, varied with the volume fraction of polymer, φ_P (where, $\varphi_P = 1- \varphi_W$). A contrast variation method of SANS and SAXS was utilized by Loppinet *et al* [55, 56] in polar solvents for both Dow® (SPC) and Nafion® (LPC).

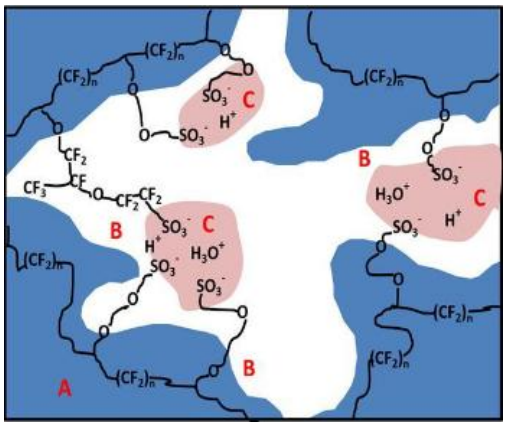

Figure 2.5: Yeager's three phase model indicating fluorocarbon region, A; interfacial region, B; ionic clusters, C. Reproduced with permission from H. L. Yeager and A. Steck, *J. Electrochem. Soc.,* 1981, 128, 1880. Copyright 1981.

An extended scattering analysis of Dow® membranes utilizing SAXS and SANS was performed by Gebel and Moore. They probed the low angle scattering maximum that is related to the crystallinity in membranes. They extracted values of the surface area per sulfonate anion for EW in the range from 635 to 1269 [57]. From the asymptotic behaviour at large scattering angles, the area per polar head group at the polymer solvent interface, β was deduced,

$$\beta = \frac{v_o \Sigma}{1-\varphi_W}, \qquad \textbf{2.2}$$

where Σ is the total surface to volume ratio, v_o average volume per ionic group, and φ_W the water volume fraction.

Similar to Nafion®**,** the ionomer peak in SAXS was found to shift to lower q as the EW decreased. Due to the increase in water uptake per polar head group, inter ionic domain distances increased. Kratky plots of Iq^2 vs. q were employed to further analyze the SAXS data. The data revealed several features PEMs with EW = 1096 and 1269 had almost identical scattering vector range, q above 0.08 $Å^{-1}$ except that the membrane with the higher EW gave a more intense small-angle upturn due to a large contribution from crystalline regions. This modifies slightly both the position and the intensity of the

ionomer peak. The ionomer peak intensity increased with decreasing EW. Porod analysis i.e. a representation of Iq^4 as a function of q indicated the existence of a sharp polymer-water interface. Regardless of large water content variation due to the considered wide EW, they found that, the specific area β remains constant. They suggested that at low water content, the swelling of the ionic aggregates involves a continuous increase of the number of ionic groups per aggregate in order to keep the specific surface constant. A structural reorganization occurs inducing a decrease of the total number of water pores and an increase of the inter-cluster distance significantly larger than the observed linear macroscopic expansion.

Gebel and co-workers in Grenoble [58] studied the structural evolution process from membrane to solution state during dissolution. The swollen membrane's structure was examined using SAXS and SANS techniques. Variation of ionic conductivity and the swelling properties with solvent was studied and results were compared with that of the solutions. Based on the analysis of scattering data over a range of water contents, a conceptual model for swelling was proposed. Using a high temperature swelling process, water-swollen membranes with water volume fractions ranging from $\varphi_W = 0.3$ to $\varphi_W = 0.93$ were obtained. For water-swollen membranes, the scattering profiles showed a prominent shift of the ionomer peak to lower q-values with increasing water content in good agreement with previous studies.

In the qualitative model proposed by this group, the dry membrane is described as containing isolated, spherical ionic clusters with diameters of ~ 15 Å and a centre-centre separation distance ~ 27 Å. With the absorption of water, the clusters swell to hold pools of water surrounded by ionic groups at the polymer-water interface in order to minimize the interfacial energy. As the water content increases to between $\varphi_W = 0.3$ to $\varphi_W = 0.5$, structural reorganization occurs to keep constant the specific surface area, and the onset of percolation achieved by the formation of connecting cylinders of water between the swollen, spherical clusters. At $\varphi_W > 0.5$, an inversion of the structure occurs such that the structure resembles a connected network of rods. Finally, as the membrane "dissolves" into solution, the rods separate to yield a colloidal dispersion of isolated rods.

SAXS combined with USAXS and SANS studies of Nafion® to explore length scales in the range 10 Å to 10000 Å with φ_P in the range of 10 % to 90 % were carried out by Rubatat *et al* [59]. From the contrast variation method and SANS technique, the structure between 100 Å to 1000 Å was described as consisting of elongated aggregates. Water uptake increases the space between these aggregates. They claimed that their model of elongated polymeric aggregates could consistently describe the evolution of polymer structure as a function of water content. However, to explain the shift in swelling behaviour observed at $\varphi_P \approx 0.6$ with the rod-like morphology of scattering particles, they proposed that the aggregates are more ribbon-like than rod-like with cross-sectional thickness of 2 nm and width ~8 nm. For the distance between the aggregates > 8 nm, the orientation distribution of the particles becomes isotropic.

Expanding on the basic structure of elongated polymeric aggregates surrounded by hydrated ionic groups [59], the spatial organization of these aggregates in polymer dispersions and films with various contents was described by Rubatat *et al* in a follow-up publication [60]. They used both the scattering and microscopic techniques to characterize the complex Nafion® structure over a large range of length scales. It was found that the form factor for cylinders fitted well the scattering curve at low scattering angle. Elongated particles were assumed to be packed and aligned backbones with the pendant sulfonic acid groups located at the periphery. The diameter of these cylindrical aggregates was found to vary from 30 Å to 50 Å depending upon the solvent used. At high dilution, these aggregates were thought to be dispersed in the solvent. The evidence for this type of polymeric aggregation in diluted suspension was presented using both atomic force microscopy (AFM) and transmission electron microscopy (TEM). Both AFM and TEM images revealed the presence of entangled rod like aggregates as shown schematically in Figure 2.6 [60].

Orfino and Holdcroft performed SAXS studies of the acid form of Nafion® 117 samples in both dry and in wet states [61]. Based on their studies, upon hydration, the number of ionic clusters decreases while their size increases. Using the scattering details it was found that 89 % of ionic sites were calculated to be residing in the cores whose diameter was estimated to be ~41 Å. There were 74 SO_3H groups per cluster and the average length of the channels between the neighbouring clusters was found to be

between 3 Å to 8 Å. Cores can only be connected by single ionic site due to the very low channel length and hence the concept of pore has no meaning on this scale.

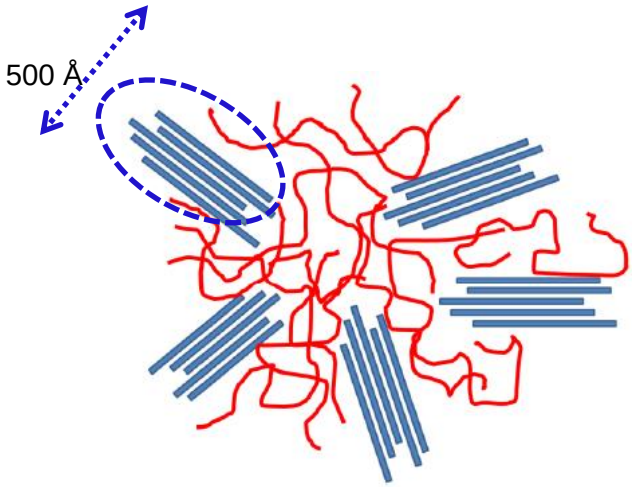

Figure 2.6: Schematic view of correlated polymer aggregates- a bundle. Position and orientation order inside the bundle is characterized by ionomer peak and the correlation length (between 50 and 100 nm) characterized by the USAXS upturn. Adapted with permission from L. Rubatat, G. Gebel, and O. Diat. *Macromolecules* 2004, 37, 7772. Copyright American Chemical Society 2004.

James *et al* [62] performed tapping mode AFM phase analysis on Nafion®115 PEM. Both the membrane and AFM were placed in a specially constructed environmental chamber to control the humidity. From their AFM phase imaging, hydrophobic and hydrophilic regions on the surface of Nafion® were identified. In the humidity range 9 % to 34 % the images support cluster model for the hydrophilic regions of Nafion®. The clusters were found to have sizes in the range from 5 nm to 30 nm, significantly larger than the structures proposed from X-ray studies. The energy dissipation that is linearly related to the sine of the phase angle was plotted against hydration. Their studies demonstrated that, with increase in hydration, the number of clusters decrease while the size of the average cluster increased similar to previous findings.

The morphology of the membranes is expected to depend on processing method, thickness and prehistory and as well on water content. Kim *et al* [63] observed

that the degree of crystallinity was related to membrane thickness. Thicker membranes exhibited a broad crystalline peak while thinner membranes did not; for instance, extruded Nafion®117 exhibited a crystalline peak at around $q = 0.03$ Å^{-1} due to non-isothermal cooling from melt while extruded Nafion®112 or solution cast as received Nafion®112 did not. The crystalline peak shifted to lower q as the thickness increased from 89 μm to 254 μm. Correspondingly, the long spacing $L_c = \frac{2\pi}{q}$ increased from 183 Å to 500 Å. This might be due to the difference in thermal history of the samples. Thick membranes from their precursor form take longer time to cool from melt and stay at crystallization temperature, T_C longer than thinner membranes. The peak position and its breadth represent most probable L_c and crystallization thickness, both of which depend on the thermal history. The position of the ionic peak is independent of the thickness of the membrane. The inter-ionic domain peak, $L_{ion} = \frac{2\pi}{q_{ion}}$, $q_{ion} < 0.1$ Å for extruded thinner membranes show a power law dependence with q with the slope of -1 in agreement with Rubatat's previous works. The value of the slope is characteristic of rod-like structures that suggest extended ionic domains that form fringed micelles due to extrusion process whereas the solution cast membranes did not show any -1 slope. In addition, the steep rise in the SANS scattering profiles from thicker samples at $q < 0.01$ Å^{-1} extends to the low q region, $q = 0.001$ Å^{-1} for both thick (183 μm and 254 μm) and thin membrane (51 μm) due to clustering of crystalline domains that form various structural features on large scale such as spherulite, bundled fringed micelles or stacked lamellae. Based on the crystallization process and the dependence of crystallization of Nafion® membranes on thickness, different possible morphologies were proposed with the aid of SANS and USANS profiles.

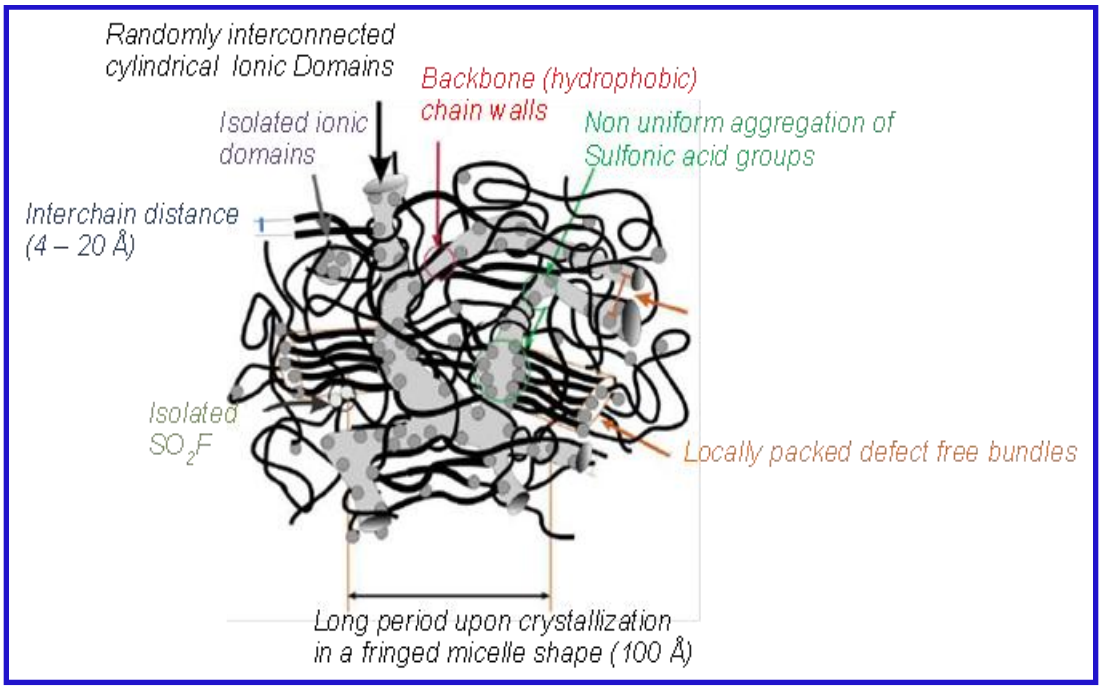

Figure 2.7: Crystallization in fringed Micelle shape of Nafion® as suggested by Kim and Grot. Reprinted with permission from M. H. Kim, C. J. Glinka, S. A. Grot, and W. G. Grot, *Macromolecules* 2006, 39, 4775. Copyright American Chemical Society 2006.

The structure of backbone depends highly on the distribution of sidechains [63]. Two extreme cases were assumed for the distribution of sidechains on the backbone and morphology was proposed based on this assumption. If the sidechains of Nafion® are distributed heterogeneously with long sequences of sidechain-free backbone then the backbones assemble into lamellar-like crystalline phase domains. When the sidechains are distributed more uniformly backbones cannot fold back due to steric and electrostatic repulsion of sidechains. This forces the membrane to crystallize in domains of fringed micelles, with parallel arrangement of backbones and sidechains that will be expelled out of the crystalline phase giving a slope of -1 in SANS. A possible structure for the amorphous membrane with thickness < 5 µm is shown in Figure. 2.7.

SAXS curves were simulated by Rohr *et al* [64]. They utilized a previously introduced numerical Fourier transformation from a given scattering density distribution [65]. A model that features long parallel water channels in cylindrical inverted micelles was found to reproduce all SAXS features at hydration levels that are typical in fuel-cell

applications. The structure assumed to be made up of parallel cylindrical water channels of diameter ~ 2.4 nm (at 20 volume % of water) lined by hydrophilic groups (Figure 2.8). These channels are locally parallel and resemble cylindrical inverted micelles that are stabilized on the outside by helical stiff backbone segments as observed by NMR [66, 67]. With persistence length of at least 5 nm for the Nafion® backbone, backbone aggregates were expected to have a persistence length of tens of nanometers. The authors were able to reproduce the entire experimental SAXS spectrum with observed power laws such as q^{-1} and q^{-4}. The minimum thickness of polymer layers was assumed to be ~ 0.7 nm. In conclusion, their new and simple water-channel model could explain the scattering data of not only unoriented samples, but also of oriented fibres with their meridional intensity for both the ionomer peak and the small-angle upturn. This model is consistent with properties of Nafion® such as high proton conductivity and water permeability [68].

Pore size distributions in ionomers such as Nafion® and their impact on proton conducting properties of PEM were studied using the method of Standard Porosimetry, SPM [69, 70]. Volfkovich *et al* [71] utilized SPM to study the structural and sorption properties of Nafion® membranes with various thicknesses and an analogue of these membranes made in Russia (MF4SK) at ambient temperature, 20°C and at 80°C.

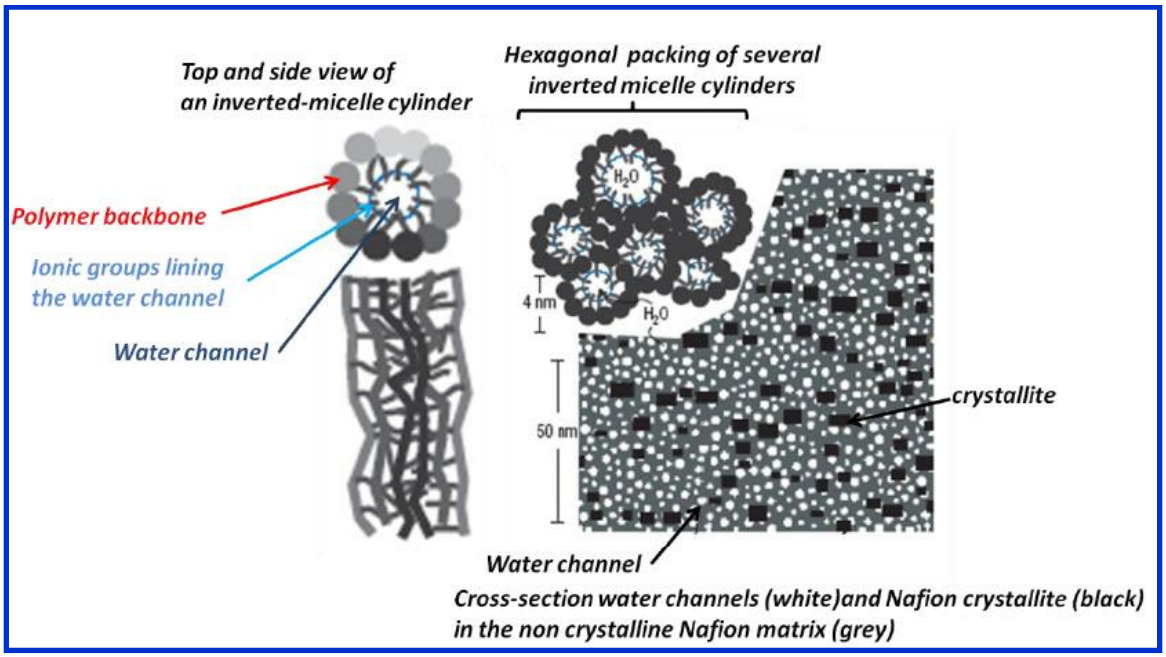

Figure 2.8: Parallel water channel model of Nafion® developed by Rohr and Chen. Adapted with permission from K. S. Rohr, and Q. Chen, *Nature Mat.,*2008, 7, 75. Copyright Nature publishing group 2008.

2.3. Water Sorption Studies and Theoretical Water Sorption Studies

Water sorption studies are a standard method of PEM characterization [71-75]. In these measurements the water content λ is measured as a function of water vapour partial pressure, $P^{v}_{H_2O}$ activity a_{H_2O}, or relative humidity, $P^{V}_{H_2O}/P^{S}$, where $P^{S}(T)$ is the saturated vapour pressure of water. It was found that isopiestic water sorption isotherms determined in this way depend on ionomer morphology, pre-treatment history and temperature.

Upon uptake of water, PFSA membranes undergo nanophase separation into hydrophilic and hydrophobic regions, creating a highly interconnected random pore network. Any sorption model should consistently describe (i) the continuous reorganization of the polymeric phase upon water uptake, (ii) the difference in uptake of water when the membranes is equilibrated with vapour vs. when it is equilibrated with

liquid water and (iii) the water back flux from cathode to anode generated by hydraulic permeation that partially compensates the electro osmotic flux.

Understanding the mechanisms of water equilibration is important in view of understanding how PEM responds to changes in external conditions. Thermodynamic model of equilibrium water sorption should consider conditions of thermal, chemical and mechanical equilibrium. Mechanical equilibrium should account for capillary, elastic and osmotic pressures. A thermodynamic model based on the effect of swelling pressure within the membrane on the chemical potential of water and hence their sorption characteristic was proposed by Choi et al [92]. Later on these authors proposed a water sorption model based on Flory-Huggins theory, including a pressure correction term for the chemical potential of water [93]. Weber et al [94] presented physical model in terms of capillary phenomena that takes into account all the relevant interactions, energies and forces associated with it. However, these models did not account for the swelling involving the mechanical equilibrium in individual membrane pores.

The model of Eikerling and Berg [95] consistently describes effects of ion exchange capacity, distribution of anionic wall charges, dielectric properties of pores, elastic properties of the polymer, temperature and gas pressure on water sorption and swelling. Their poroelectroelastic model introduces a mechanism of PEM water sorption that is based on thermodynamic principles. It relates a microscopic swelling parameter to the thermodynamic conditions and microscopic properties, including the density of anionic groups at pore walls, the dielectric permittivity of water in pores and the elastic properties of the polymer in a single pore. The single pore swelling was linked to ensemble effects through an integral expression for the macroscopic volumetric expansion of the pore network upon water uptake. Equation 2.3 involves a convolution of the microscopic swelling parameter, ε which accounts for the pressure balance in a single pore with wall charge density σ_0, with the density distribution n(σ_0) in the pore ensemble that accounts for the heterogeneous PEM microstructure, giving the macroscopic volumetric expansion of the PEM,

$$\frac{\Delta V}{V_0} = \frac{1}{N_{uc}} \int_0^{\sigma_{0,c}} d\sigma_0 n(\sigma_0) \varepsilon(\sigma_0, \sigma_{0,c}), \qquad \textbf{2.3}$$

where $0 < \sigma_{0,c} < \sigma_0^{max}$.

$\sigma_{0,c}$ in the largest pore in which capillary equilibrium prevails. N_{uc} is the number of unit cell in a sample of dry volume, V_0.

2.4. Design of New Membrane Materials

Due to inherent difficulties faced by Nafion® membrane materials at high temperature and at low RH, modifications were proposed in order to design, synthesize materials that could provide acceptable proton conductivity (~0.09 Scm^{-1}) at high temperature and at low RH. In coming paragraphs, various modifications made to PFSA type membranes such as, short side chain membranes, hybrid membranes, hydrocarbon membranes and block copolymer membranes will be discussed.

Poor proton conductivity at low relative humidity was addressed by producing PEM with short sidechains and high IEC such as Aquivion®, which improve water retention. Replacing water with nonaqueous and low-volatile media has been met with some success. Development of hydrocarbon membranes, hybrid membranes and block co-polymers membranes have been pursued as well. Finally, theoretical calculations that shed light into effect of various chemical modifications on conductivity are discussed.

2.4.1. Short Sidechain Ionomers

Short sidechain (SSC) PEMs were originally synthesized by Dow chemical company in the 1980s but their development was discontinued because of its complicated and costly synthesis. Nowadays, SSC PEM is commercialized by Solvay Solexis under the name Aquivion® [96]. The chemical structure is shown in Figure. 2.9. Aquivion® membranes possess shorter sidechains and higher ratio of SO_3H to CF_2 compared to Nafion® [91] their properties are similar to those of Dow ionomers [93]. Compared to LSC PFSA ionomers, these ionomers exhibit higher degree of crystallinity, enhanced proton conductivity and higher glass transition temperature, T_g [96], that gives this membrane improved mechanical stability, greater fuel cell efficiency and enable higher temperature

operation. Studies pertaining to SSC PFSA ionomers including 3M membranes are reported in [97].

SSC PFSA ionomers with different IECs were characterized with respect to water sorption, proton conductivity, electro-osmotic drag, water diffusion and microstructure as a function of temperature and degree of hydration by Kreuer et al [101]. The results were compared with that of a long sidechain (LSC) PFSA, Nafion®1100. It was reported that SSC PFSA membranes displayed almost similar water and proton transport and similar hydrophobic/hydrophilic phase separation as a function of water volume fraction. The superior performance of SSC PFSA was assigned to its higher elastic modulus. Low equivalent weight ionomers are possible due to high crystallinity and hence better mechanical properties. This leads to higher concentration of protonic charge carriers.

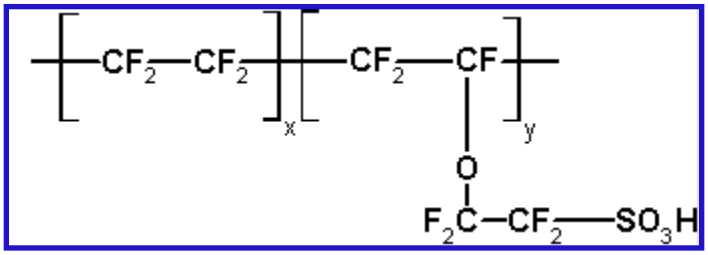

Figure 2.9: Chemical Structure of SSC PFSA (Aquivion®). Redrawn from A. Stassi, L. Gatto, E. Passalacqua, V. Antonucci, and A. S. Arico. *J. Power Sources* 2011, 196, 8925.

Better performance of low equivalent weight SSC PFSA membranes in hydrogen fuel cells was linked to improved solvent permeation from cathode to anode and higher IEC. Higher stability of membrane electrode assemblies was related to better morphological stability of SSC PFSA. The higher glass transition temperature of SSC PFSA ionomers gives stability to the electrode|electrolyte interfaces at higher temperatures where Nafion® seems to undergo severe conformational changes.

2.4.2. Hybrid Nafion® Membranes

In order to improve the performance of Nafion® and water retention at higher temperatures, composite membrane made of Nafion® and silica was prepared by Antonucci et al [102]. Higher operational temperature typically around 145ºC for liquid

fed direct methanol fuel cells demonstrated the utility of this composite membrane [103]. A peak power density of 240 mV / cm^2 for oxygen fed cell was achieved. Other hybridization concepts have been pursued [104-109]. The inclusion of inorganic oxide nanoparticles inside the structure of recast Nafion® lowers the membrane resistivity of due to the hygroscopic nature of the silicon oxide that improves water uptake and retention, [103] enabling operation at high temperatures. The study of Miyake et al [110] on Nafion®117/Silica showed that hybrid membrane could retain water up to 120ºC but not at higher temperatures such as 150ºC or 170ºC. The proton conductivity in Nafion® / Silica hybrid membranes was found to be equal to or lower than that of unmodified Nafion® at all temperatures and at all water vapour activities.

Savinell et al [9] incorporated phosphoric acid into Nafion® and achieved a conductivity of 0.05 Scm^{-1} at 150°C. The low volatile H_3PO_4 acts as a Brönsted base, solvating the proton from the strong sulfonic acid group, CF_3SO_3H, forming $H_4PO_4^+$ and $CF_3SO_3^-$. The conductivity of phosphoric acid swollen Nafion® was found to be lower than that of pure phosphoric acid. Although improved kinetics for oxygen reduction at the cathode has been reported, failure of the anode occurred after a short period of operation that was attributed to the possible anion ($H_2PO_4^-$) migration and the consequent electrode flooding.

2.4.3. Hydrocarbon Membranes

Hydrocarbon membranes are less expensive, and they have nowadays good thermal, chemical and mechanical properties. Poly Styrene Sulfonic acid (PSSA) was one of the first ionomers put to commercial use. The first polystyrene membranes were developed in 1955 by General Electric and were used in the first PEFCs operational fuel cells in the Gemini space program. The system had a limited lifetime < 200 h due to the ionomer degradation by radical attack. In order to improve its lifetime, further work involved cross-linking that yielded lifetimes of about several thousand with power densities of 0.05 kW m^{-2} to 0.1 kW m^{-2}. Another system involved cross-linked polystyrene-divinylbenzene sulfonic acid membrane in an inert matrix. The lifetime of the membrane had a range 1000 – 10000 h with power density of 0.75 kW m^{-2} to 0.8 kW m^{-2} [105]. The major drawback with these membranes is the poor protonic conductivity which limited power

density to below 100 mWm^{-2} [92]. Various research groups work on synthesizing different sulfonated polymers containing diaryl sulfone units. Wang *et al* [112] prepared biphenol based complete aromatic poly (arylene ether sulfone)s (BPSH) containing up to at least two pendant sulfonate groups per repeat unit. AFM revealed a membrane morphology consisting of hydrophilic phase domains that increased in size from 10 to 25 nm with increasing degree of sulfonation. These ionomers were stable up to 220ºC in air. Proton conductivity (σ) as high as 0.17 Scm^{-1} at 30°C in water could be reached with the highly sulfonated form of these membranes, as shown in Figure. 2.10.

Where n + m / *k* = 1.01 in mole

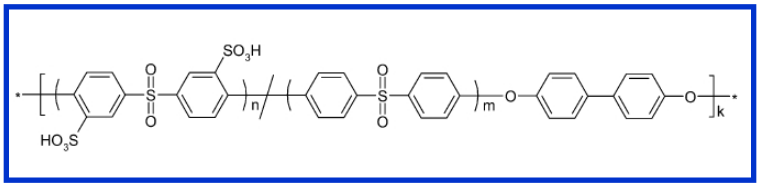

Figure 2.10: The chemical structure of sulfonated poly arylene ether sulfone membranes considered for as an alternative PEM. Adapted with permission from F. Wang, M. Hickner, Y. Seung Kim, T. A. Zawodzinski, J. E. McGrath *J. Membr. Sci.* 2002, 197, 231. Copyright Elsevier 2002.

Poppe *et al* [113] synthesized flexible PEM consisting of carboxylated and sulfonated poly (arylene-co-arylene sulfones). Sulfonated membranes gave conductivity in the range of σ = 0.11 – 0.23 Scm^{-1}. The carboxylated analogs showed reduced swelling, lower water uptake and hence reduced protonic conductivity, Fig. 2.11.

Lafitte *et al* [114] modified polysulfones by attaching pendant chains of sulfonated phenyl groups via ketone links by lithiation of sulfophenylated using BuLi (Butyl lithium) followed by anionic reaction with 2-sulfobenzoic acid cyclic anhydride. Higher proton conductivity of 3.2 x 10^{-2} Scm^{-1} at 60°C is noted in these membranes with ~1 sulfophenyl units per polysulfone unit and at water weight % of 30, Figure. 2.12.

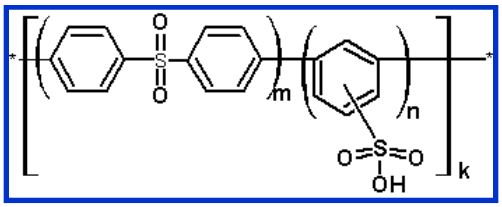

Figure 2.11: Sulfonated poly (arylene-co-arylene) sulfones. Adapted from D. Poppe, H. Frey, K. D. Kreuer, A. Heinzel, and R. Mülhaupt, *Macromolecules,* 2002, 35, 7936 with permission. Copyright 2002. American Chemical Society.

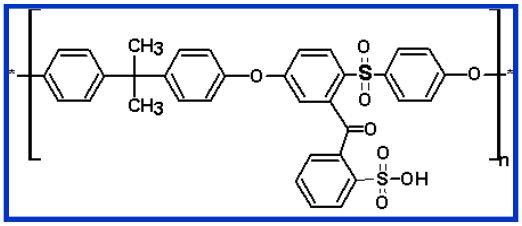

Figure 2.12: Sulfophenylated poly sulfone. Adapted with permission from Benoît Lafitte, Lina E. Karlsson, Patric Jannasch, *Macromol. Rapid Commun.,* 2002, 23, 896. Copyright John Wiley and Sons 2002.

In order to reduce the cost of the PEM, Meng *et al* [115] synthesized PEMs with phosphonic acid instead of sulfonic acid as hydrophilic moieties in poly-(arylene ether)s. These ethers have glass transition temperature in the range $254^{\circ}C < T_g < 310^{\circ}$ C along with high molecular weight. The proton conductivity of these membranes were found to range from 10^{-5} S cm^{-1} to 10^{-6} S cm^{-1}. New ionomer system were prepared by blending sulfonated arylene main-chain polymers like sulfonated PEEK (SPEEK), sulfonated polysulfones (SPSU) with polymers like poly(4-vinyl pyridine) [116], polybenzimidazole (PBI) and sulfonated napthalenic polymidie that show very good chemical and thermal stability as well as high proton conductivity [117], depicted in Figure. 2.13.

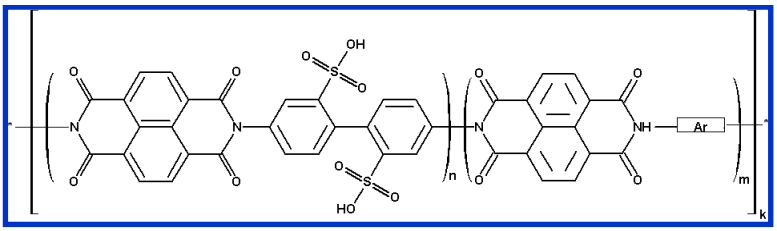

Figure 2.13: Sulfonated naphthalenic polyimide (Ar, various aromatic groups). Adapted from C. Genies, R. Mercier, B. Sillion, N. Cornet, G. Gebel, and M. Pineri, *Polymer* 2001,42, 359 with permission. Copyright Elsevier 2001.

Recently, Wang et al [118] synthesized imidazole micro capsules (IMCs) that are tunable with the number of imidazole groups, shell thickness, and incorporated into sulfonated poly(etheretherketone) (SPEEK). Enhanced proton conduction at low relative humidity and water retention properties were found for the composite membranes of IMCs in SPEEK. At 20 % RH, they found for the composite membrane, increase in proton conductivity of 1 to 2 orders of magnitude compared to the control membrane, SPEEK. The enhanced proton conductivity was found to afford the composite membrane with elevated peak power density from 69.5 to 104.5 Wcm^{-2}. They proposed that proton conductivity and water retention properties originate from both the lumen and shell of IMCs. The lumen acts as water reservoir and shell of imidazole manipulate the water release. They form anhydrous proton transfer pathways and low energy barrier pathways for proton hopping, imparting an enhanced proton transfer via either a vehicle mechanism or Grotthuss mechanism. Figure 2.14 shows a schematic representation of conduction mechanism in both control and composite membrane.

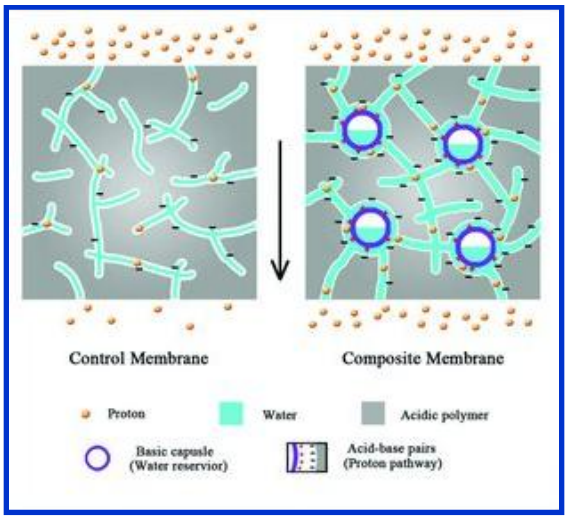

Figure 2.14: Schematic representation of proton conduction in control membrane (SPEEK) and Composite membrane (SPEEK-IMC composite). Adapted from J. Wang , X. Yue , Z. Zhang , Z. Yang , Y. Li , H. Zhang , X. Yang , H. Wu , and Z. Jiang *Adv. Funct. Mater*. 2012, 22, 4539 with permission. Copyright 2012 WILEY-VCH Verlag GmbH & Co. KGaA, Weinheim.

2.4.4. Block Copolymers

Self-assembled block copolymers lead to well-defined nanostructures wherein the morphology and domain size are tunable on the nanoscopic length scale [119]. In ion-containing block copolymers, the ionic part promotes ion conduction while the nonionic part of the block imparts mechanical support to the membrane. A number of recent studies on these types of membranes have demonstrated good proton conductivity values over a wide range of temperature and humidity [119-123]. Well-ordered morphologies in ionic block copolymers have only been demonstrated in sulfonated block copolymers with sulfonation levels at or below 50 mol % and MW < 100 Kg mol^{-1}[96]. Somewhat ordered block copolymer phases in samples with MW of 20-100 Kg mol^{-1} and degrees of sulfonation of up to 100 mol % was shown by Rubatat *et al* [123] and Saito *et al* [124], Figure. 2.15. High molecular weight systems with high degrees of sulfonation were found to be not as ordered as evidenced from scattering and microscopy studies.

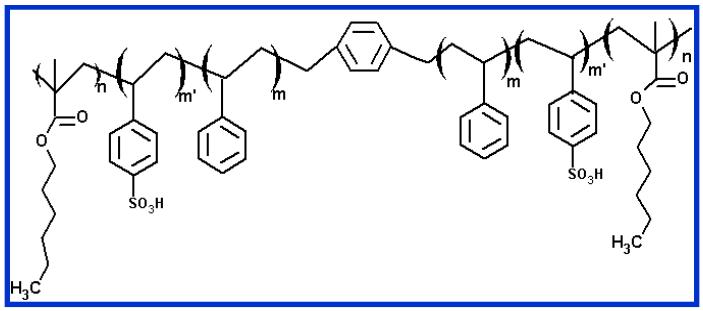

Figure 2.15: High molecular weight, block copolymer with aliphatic backbone. Adapted with permission from T. Saito, H. D. Moore, and M. A. Hickner *Macromolecules,* 2010, 43, 599. Copyright 2010. American Chemical Society.

Various morphological phases were observed as a function of volume fraction of the sulfonated phase in block polymers [118, 119]. Sulfonated poly (styrene-b-methylbutene) [Figure 2.19], showed disordered, lamellar, hexagonal packed cylinders, hexagonally perforated lamellar, and gyroid phases within a narrow volume range (0.45 - 0.5) of sulfonated poly (styrene) as a function of mol % of sulfonation in the styrene phase and molecular weight [119].

Similar to most sulfonated polymers, sulfonated block copolymers exhibit an increase in proton conductivity with IEC and λ. Due to their unique ionic domain structure, block copolymers generally have different relationships between IEC, λ and σ. Figure. 2.16 shows proton conductivity as a function of λ for Nafion®, block and random copolymers at 80°C [126]. In this figure the block copolymer has lower conductivity than Nafion® at low hydration, but at λ > 4-5, the conductivity of the block copolymer exceeds that of Nafion®. The higher acidity of Nafion® promotes higher conductivity at low hydration. At high hydration, the well-defined ionic domain structure of the block copolymer PEM provides higher conductivity than Nafion®. Changes in morphology through hydration or sulfonation lead to large alterations of transport properties. Morphological transitions from periodic lamellar morphology oriented anisotropically at IEC = 0.5-1 meq g^{-1} to an isotropic structure at IEC = 1.1 to 2 meq g^{-1} at RT were studied. These morphological transitions resulted in discontinuous abrupt increase in conductivity with increasing IEC. Such transitions were revealed in studies of Elabd *et al* [120] on sulfonated poly (styrene-b-isobutylene-b-styrene), Figure. 2.17. Both Figures. 2.16 and 2.17 reveal that, sulfonated block copolymers exhibit enhanced proton

conductivity compared to other sulfonated polymer architectures such as random copolymers at similar IEC and λ.

The connection between morphology and transport properties in block copolymers was shown by Holdcroft *et al* [128,129], Figure 2.18. In their work on sulfonated poly([vinylidene difluoride-co-hexafluoropropylene]-b-sytrene) higher conductivities were observed compared to both random and graft copolymers of sulfonated poly(styrene) at the same IEC. Higher conductivities were reported in the fluorinated block copolymer compared to other nonfluorinated sulfonated block copolymers such as sulfonated poly (styrene-b-(ethylene-r-butylene)-b-styrene)). TEM pictures of these materials revealed distruption in ordered morphology with increasing degree of sulfonation. These membranes with IEC = 0.6 – 1.2 meq / g showed a phase-separated morphology containing ion channels of 8 – 15 nm width.

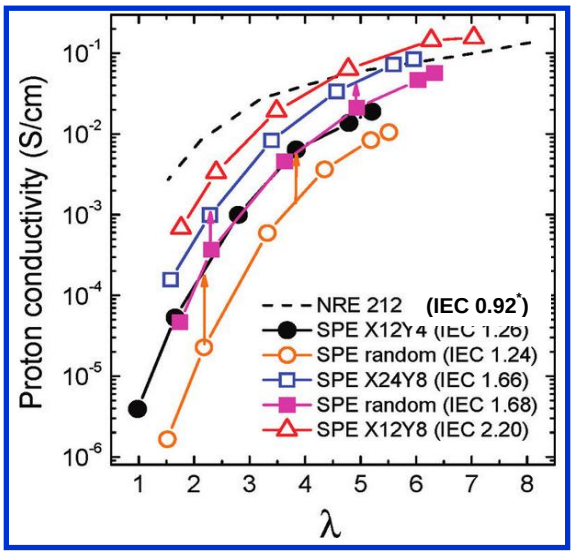

Figure 2.16: Proton conductivity as a function of λ for Nafion® NRE 212, SPE block, and SPE random copolymers at 80°C. Adapted with permission from B. Bae, K. Miyatake, and M. Watanabe *ACS Appl.Mater.Int.,* 2009, 1, 1279. Copy right 2009. (*H. Dai, H. Zhang, Q. Luo,Y. Zhang, and Cheng Bi *J. Power Sources* 2008, 185, 19.)

Sulfonated block copolymers were shown to have greater absolute proton conductivities and hence, phase separated morphologies [119-121, 126, 128 and 129]. It

was shown that orientation, size of block micro domains, and crystallinity in the nonconductive micro domain affect proton transport [119, 122 and 132].

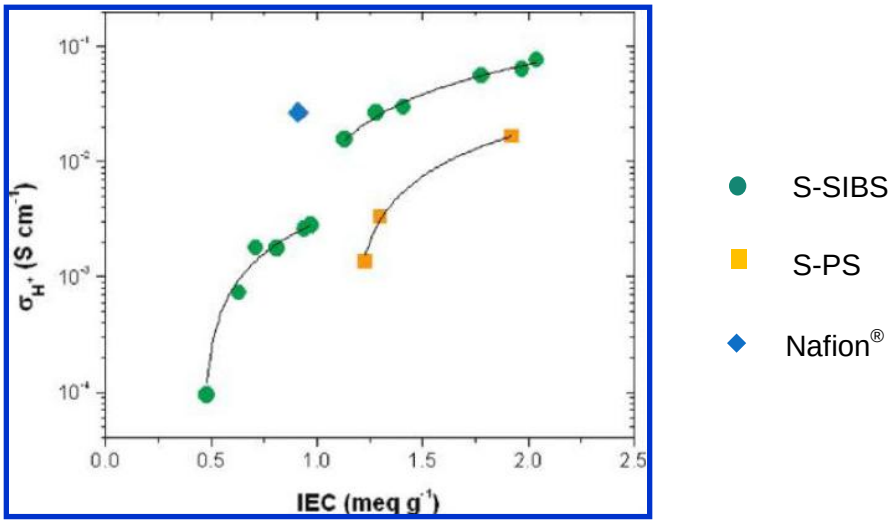

Figure 2.17: Conductivity of Nafion® as blue diamonds. Green dots represents Poly (styrene-b-isobutylene-b-styrene) and sulfonated poly (styrene) as orange square at room temperature. Adapted with permission from Y. A. Elabd, E. Napadensky, C. W. Walker, and K. I. Winey *Macromolecules, 2006,* 39, 399. Copyright 2006. American Chemical Society.

Two different block copolymers were studied by Frisken *et al* [123]. Both block polymers contain a fluorocarbon block and a sulfonated polystyrene block. In this study, the length and degree of sulfonation of polystyrene segment have been controlled. Using SANS with contrast variation and TEM was used to investigate the nanostructures of these polymers. Longer length scale morphology found to be well-ordered for diblocks containing long and partially sulfonated polystyrene whereas more disordered structure formed from short and fully sulfonated polystyrene blocks. Films were found to possess structure at two different length scales: phase separation at length scales of the order of 40nm due to insoluble nature of both blocks and a substructure within the sulfonated polystyrene domains due to segregation of the hydrated ionic groups.

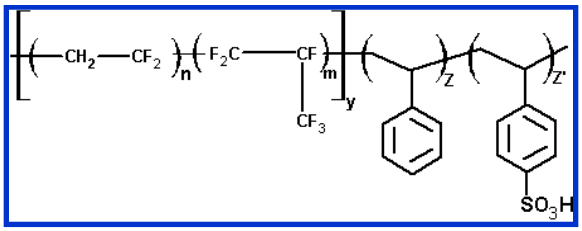

Figure 2.18: Fluorinated block copolymer. Adapted with permission from Z. Shi, and S. Holdcroft, *Macromolecules,* 2005*,* 38, 4193. Copyright 2005. American Chemical Society.

They considered two different series for analysis. For series 1 the polystyrene block consists of different degrees of sulfonation with the same length and series 2 are fully sulfonated but have different lengths of polystyrene chain. Large scale structure, typically of few hundred angstroms of these series was found to be very different from the analysis of SANS and TEM. The short scale structure, typically of few tens of angstroms, is found to be similar in both series. The small scale structure corresponds to the structure of hydrated polystyrene domains. Based on proton conductivity data it was concluded that, the largest effect on the conductivity might probably originate from the proton diffusion that occurs within the polystyrene domains. It was also observed that less ordered membranes from series 2 have better proton conductivities, which might be due to a more favourable structure in sulfonated polystyrene domains.

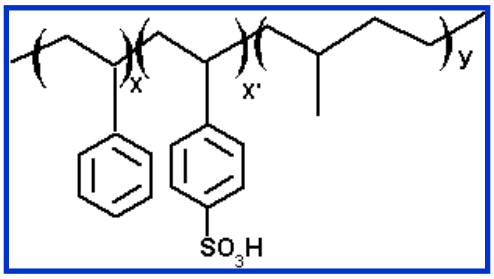

Figure 2.19: Block copolymer with aliphatic backbone. Adapted with permission from M. J. Park, and N. P. Balsara, *Macromolecules,* 2008*,* 41, 3678. Copyright 2008. American Chemical Society.

The importance of organized ionic domains for proton conductivity was shown by the work of Frisken *et al* [130]. Synthesis of self-assembled surface charged nanoparticles of latex to create continuous proton conduction pathways was proposed in the literature. Nanoparticles composed of a core of cross-linked poly (methyl

methacrylate-r-butyl acrylate) with hydrophilic PSSA surface were formed. These membranes were cast from aqueous dispersions of these nanoparticles, which self-assemble. Comparing conductivity with IEC, the membrane composed of nanoparticles had an acid content threshold of IEC < 1.2 meq/g. Compared to the solution cast analogue, at the acid content of 0.7 meq/g, the conductivity is found to be very low, 0.005 S cm^{-1} indicating homogeneous and more efficient distribution of charge.

2.4.5. Modeling Studies of PFSA Membranes

First principles based molecular modelling studies of SSC PFSA were carried out by Paddison et al [134-136]. It was found that the sidechain separation has an effect on the nature of the hydrogen bonding between the sulfonic acid groups and the number of water molecules needed to transfer a proton to the first hydration shell [134]. Hybrid method such as ONIOM / DFT was utilized by Paddison et al [136] to study the energetics of hydration of three sidechains of SSC PFSA. The ONIOM method was developed in the group of Prof. Keiji Morokuma (Emory University in Atlanta, Georgia USA), now at Fukui Institute for Fundamental Chemistry, Kyoto University. In this method, in order to decrease the computational cost in treating large system, the large system is partitioned into three levels of varying complexity. The part of system wherein important events occur such as bond-making or breaking is treated using high level of theory. Regions far away from the reactive site of the system are treated with a lower level of the theory. For high-level calculations, Paddison et al used a hybrid DFT method for CF_3SO_3H groups and H_2O molecules considered. Medium level simulations using HF/3-21G** were applied to treating entire backbone and the $–OCF_2$ portion of each sidechain. 6 to 9 water molecules were added explicitly to oligomers. All the sulfonic acid groups were connected through hydrogen bonding mediated by water.

Chapter 3. Proton Transport Mechanisms

3.1. Proton Transport Mechanisms

In order to gain insights into various processes in chemistry and biology, detailed understanding of the behaviour of ions in water is essential. Significant theoretical and as well experimental efforts were made to investigate the water ions. The resulting qualitative picture [137-142] is still found to be incomplete and controversial. Owing to the anomalous high mobility of protons in water and in ice, transport of protons in water is considered as an example of the Grotthus chain mechanism in which the charge migration is characterized by successive jumps of a proton from one oxygen centre to the next. Although, the basic feature of proton conduction was recognized at an early stage [137], the role of hydrogen bonding in aq. systems became clear and this picture was refined by assuming that proton transfer occurs preferentially along the hydrogen bonds [138,139].Spectroscopic experiments in solution were [137] able to show that the charge defects introduced by excess or missing protons in water occur naturally in the form of simple, relatively long-lived hydronium ion (H_3O^+) and hydroxyl ion (OH^-). Combining these two key notions of hydrogen bonding and water ions, one can write the charge transfer process along a hydrogen bond in the form

$$H_2O \cdot H^+ \cdots OH_2 \rightleftharpoons H_2O \cdots H^+ \cdot OH_2 \,(\text{For } H^+), \qquad \textbf{3.1}$$

$$HOH \cdots OH^- \rightleftharpoons HO^- \cdots HOH \;(\text{For } OH^-). \qquad \textbf{3.2}$$

In the liquid state, more complex solvation structures occur which have an impact on proton transport. The strong interaction of $1H_2O$ with a H_3O^+ ion leads to the formation of a Zundel-ion, in which the excess protons is delocalized between two neighboring water molecules [148]. The position of the excess proton can be visualized in Figure 3.1:

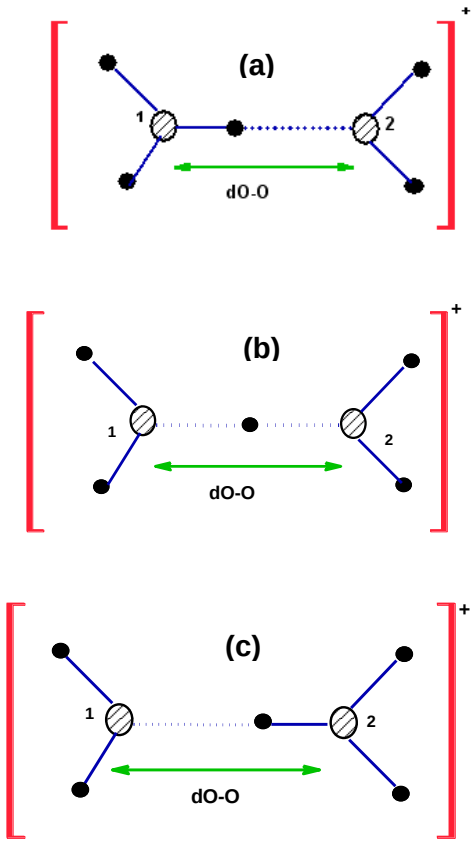

$$\delta = d_{O_1H} - d_{O_2H}$$

Figure 3.1: Schematic representation of 1D potential which the central proton experiences when it is displaced along O-O axis, at fixed O-O distance, d_{O-O} shown for (a) δ < 0.5 Å(large) and (b) δ =0 (small) and for (c) δ > 0.5 Å(intermediate) distances. Adapted with permission from D. Marx, *ChemPhysChem* 2006, 7, 1848. Copyright 2006 WILEY-VCH Verlag GmbH & Co. KGaA, Weinheim.:

As depicted in Figure 3.1, in the energetically most favourable arrangement the proton sits symmetrically between O1 and O2. This type of H-bond is represented generally as an “ultra-strong”, “symmetrical” bond. When both oxygens are moved farther and dislocate the proton along the elongated O-O bond, it will form H_3O^+ ion with one of the neighboring H_2O as depicted in Figure 3.1a. and this situation corresponds to the well-known 1D double minimum proton potential that is generally used to represent the proton transfer along H bonds. The difference between distances of the central proton with O1 and O2 is represented as δ. For symmetric bonding system, δ is zero. δ

is one of the parameter that defines the proton potential in 1D, V(δ). This function can be tuned to make barrier less proton transfer as in the case of symmetric bond. The major contribution to proton translocation is the proton tunnelling in liquids that is explained in the paper [149]. Different situations arise in the case of PEMs where excess protons or hydronium ions can be found in ultra-small spaces.

In the case of PEFC, operation at temperatures above 100ºC is desirable as it significantly improves the kinetics of electrode reactions and hence, could decisively reduce the Pt requirement [4,150-155]. Voltage losses due to reactant and water transport could also be reduced at higher temperature. The advantages of operating PEFCs at temperature above 100ºC provide a strong incentive for studying proton transport mechanisms in PEMs under conditions relevant for this temperature range. Due to the evaporation of weakly bound bulk-like water, only a small amount of residual water at acid-functionalized pore walls of polymer aggregates is retained in the membrane at T > 100°C. Understanding proton transport mechanism in both low and as well high water content could provide better understanding of the nature of various structures that could be formed at these conditions.

At high water contents, λ > 15 the activation energy of proton conductivity found from Arrhenius plots lies in the range of ~0.10 eV, similar to the activation energy of proton transport in free bulk water [150-155]. At water contents below λ~ 3, the activation energy of proton transport in PEM increases by about a factor of 3 to > 0.35 eV [37, 146, 147], Figure 3.2. This drastic increase indicates a change in the proton transport mechanism.

We provide in Figure 3.3a and in Figure 3.3b simplified pictures of a pore situation, and here we do not aim to represent any specific pore morphology. Pores can have different shapes including spherical, cylindrical or lamellar-like pores. Our main purpose here is to illustrate the effect of transition of water content from surface to bulk-like on proton transport mechanisms [187, 183]. The situation of a membrane pore at low water content is shown in Figure. 3.3a. At this low water content situation, only strongly bound surface water remains and protons move close to the hydrated interface.

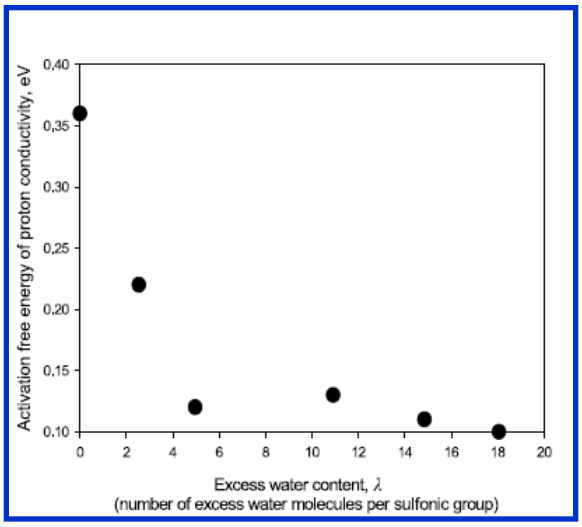

Figure 3.2: Activation energy of proton transport as a function of water content. Adapted with permission from M. Cappadonia, J. W. Ering and U. Stimming *J. Electroanal. Chem.*, 1994, 376,189. Copyright Elsevier 1994

Under well humidified conditions, illustrated in Figure 3.3b, high proton conductivity values for Nafion® are the results of the high concentration of mobile protons and the well-connected network of water-filled pores [37, 75, 150, 156, 183, and 198]. The protonic conductivity reaches values of ~ 0.1 Scm^{-1} at 30°C and at high water contents, $\lambda > 15$ [37]. In fully hydrated PEMs, water assumes "bulk-like" properties. DFT studies [18, 32] as well as theoretical studies [129, 178] predict that at $\lambda > 6$ the majority of protons move at sufficient distance away from surface groups with only small residual interaction between excess protons and hydronium ions.

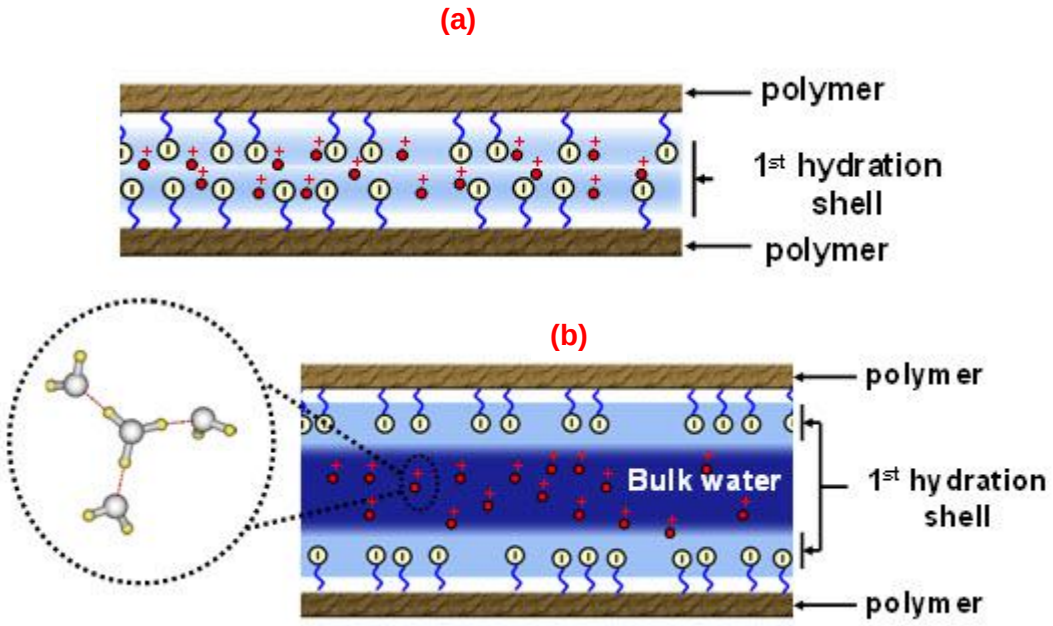

Figure 3.3: Sketch of membrane pore at (a) low and (b) high water content.

3.2. Proton Transport Mechanism in Bulk Water

The mechanism of proton transport was analysed in detail by Agmon [157, 158] and studied using ab initio molecular dynamics calculations performed by Tuckermann *et al* [159, 160] and Marx *et al* [154,155]. The widely accepted mechanism is known as Grotthuss diffusion or structural diffusion [156]. It involves the so called Zundel ion, $H_5O_2^+$ [162], where in a proton is shared between two water molecules, the Eigen ion, $H_9O_4^+$ [163], in which a single hydronium ion is solvated by three water molecules. *Ab initio* simulations of excess proton in bulk water have shown that, both the complexes are needed to describe the proton transfer mechanism [159,165]. Analysing the trajectories meticulously, it was found that the interconversion between these two complexes is modulated by fluctuations in the surrounding hydrogen bonded network. These fluctuations induce the breaking of a hydrogen bond in the second solvation shell. This reduces the coordination number of water molecule from the preferred value of 4 to 3 as shown in Figure 3.4a and in Figure 3.4b [154]. This step was identified as rate limiting. The time scale of hydrogen bond breaking and reorientation of water molecules

is in the order of picoseconds. This time scale governs the proton transfer mechanism via structural diffusion. After this coordination change of the proton-receiving water molecule, the proton can transfer readily as shown in Figure 3.4b and in 3.4c.

Calculations from first principles impose severe restrictions in terms of cost and system size. The length of simulations is often insufficient to obtain well converged values of thermodynamic and dynamical quantities of interest. A semi empirical method, the Empirical Valence Bond (EVB) model, was developed to overcome these difficulties. In the EVB model, the state of a chemical reaction process is described as a linear combination of a small number of independent, empirically-motivated valence bond (VB) ‘‘states’’.

Forms and functions of VB states are chosen to reproduce key aspects of actual PES usually determined from ab initio calculations or experimental results. The EVB approach was proposed by Warshel [166]. Two different groups, Voth et al [167-171] and Borgis et al [172-175] utilized Warshel’s EVB model and extended the concept to study activation free energies of proton transfer events in liquid water. Interconversion between Eigen- Zundel plays an vital role in proton transfer events. As an example, first Eigen ion converts to Zundel ion which then converts to Eigen ion and the sequence continues.This is generally represented as EZE mechanism. Voth and his coworkers found evidence of EZE mechanism, Figure 3.5, in which proton transfer with Eigen cation more stable by about 8 kcal / mol (33 kJ / mol) [171]. Supporting evidence for such mechanism of proton transfer comes from path integral molecular dynamics study [154].

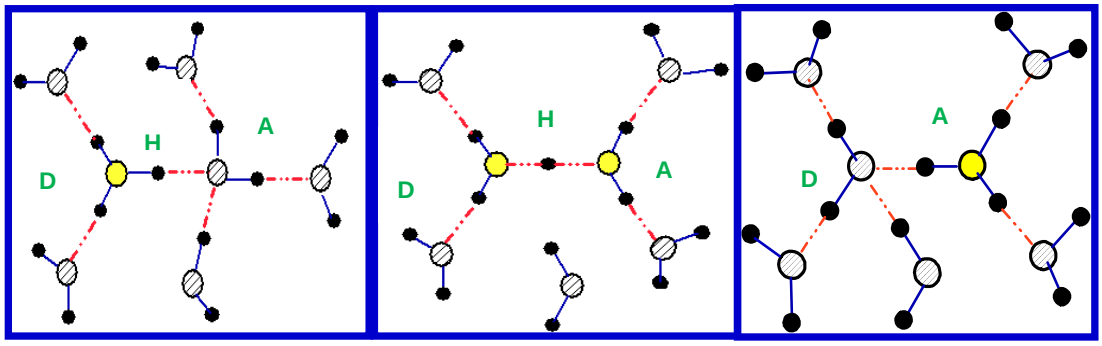

Figure 3.4: **Representation of charge defect migration (a)-(b) rate limiting step with three coordinated water molecules and picosecond breaking and making of H bonds. (c) represents transfer of proton (H^+) from D-A where, D represents donor and A represents acceptor. Picture redrawn with permission from M. E. Tuckerman, K. Laasonen, and M. Parrinello, *Nature* 2002, 417, 925. Nature publishing group. Copyright 2002.**

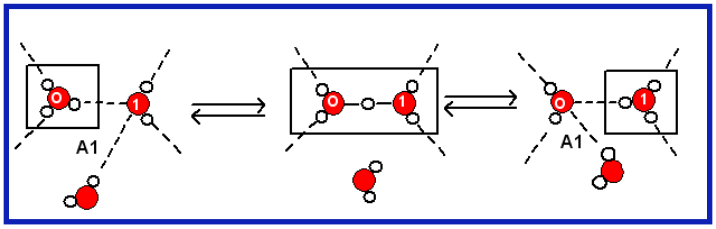

Figure 3.5: **Eigen-Zundel-Eigen (EZE) Mechanism. Red filled circles represent oxygen atoms while unfilled white circle represent hydrogen atoms. Hydrogen bonds are represented by dashed lines. Adapted with permission from O. Markovitch, H. Chen, S. Izvekov, F. Paesani, G. A. Voth, and N. Agmon. *J. Phys. Chem. B* 2008, 112, 9456. Copyright 2008, American Chemical Society.**

Proton Transport in PEMs at Low Hydration

Studies of proton transport in heterogeneous systems like PEM was carried out by several groups using various approaches. From experiments measurable proton conductivity was found remained even in almost dry Nafion® [176]. This implies that pathways for proton conductivity persist under these conditions. This was supported by

recent molecular modelling studies of hydrated Nafion® using hybrid Monte Carlo/reference interaction site model (MC/RISM) simulation technique [18]. From their simulation the authors concluded that the aggregation of the sulfonic acid groups proceeds even with a small amount of water in the membrane. Water was found to form specific cage-like structures similar to clathrates. These clathrates favour the formation of continuous channels at low hydration.

At low hydration, the flexibility of ionomer sidechains is critical in order to facilitate proton transport. The role of backbone conformation on hydration and proton transfer in SSC PFSA under minimal hydration was analysed using first principles molecular modelling [177]. Optimized global minimum energy structures were obtained for cluster geometries of SSC PFSA with 2 sidechains attached on the backbone and sulfonic acid interacting with the added water molecules. Four to seven water molecules were added explicitly and for each added system, the optimized structures were analysed.The folded conformation of the backbone was found to be energetically favourable over the extended conformation where all the carbon atoms are in trans configuration. Conformational changes in the backbone increase the chance of proton dissociation when the acid groups are brought close to each other.

In order to understand proton dissociation and stabilization of the dissociated proton, a series of electronic structure calculations were performed on trifilic acid (as model for Nafion®) and para-toluene sulfonic acid (that mimicks SPEEK) [178]. Minimum energy conformations were obtained from DFT studies at the B3LYP / 6-31G** level for systems with increasing number of H_2O molecules. It was observed that the dissociation of the acid proton occurred only upon addition of the fourth water molecule. The formation of H_3O^+ in water is favoured by the stabilization of the excess positive charge in the hydrogen bonding network and by the delocalization of the excess negative charge on the sulfonate anion. For the perfluorinated system, the distance between the sulfonate oxygen from which the proton left and oxygen on the hydronium ion assumes a value intermediate of that observed in Eigen ($H_9O_4^+$: 2.60 Å) and Zundel ions ($H_5O_2^+$: 2.50 Å) in bulk water [148] for the aromatic system (~ 2.4 Å) a smaller value was found. When the sixth water molecule was added to the cluster geometry, separation of H_3O^+ from the sulfonate group resulted in the formation of an $H_9O_4^+$ with average hydrogen

bond length, $d_{O—O}$ ~ 2.6 Å . With six H_2O molecules added, the electrostatic interaction with the sulfonate anion is shielded by an intermediate water layer and the closest O···O distance between H_3O^+ and sulfonate anion increased from 2.6 Å to 4.2 Å for CF_3SO_3H and from 2.4 Å to 3.6 Å for $CH_3C_6H_5$. The first hydration shell separating hydronium ion and sulfonate anion consists of 5 H_2O in agreement with findings from FT-IR spectral studies by Zanderighi et al [179]. In a subsequent paper, Paddison et al observed the formation of $H_5O_2^+$ in optimization studies of sidechains of SSC (Aquivion®) membrane with 6 surrounding H_2O.

Ab initio molecular dynamics was performed on a trifluoromethane sulfonic acid monohydrate (TAM) crystal [195] by Eikerling *et al* [188]. The system considered provided a model for proton transfer in minimally hydrated sulfonic acid based PEMs. Simulations identified the formation of the $H_5O_2^+$ion and re-organization of neighboring sulfonate groups that share a proton between oxygen atoms on the anionic sites with activation energy of ~0.3 eV. The calculations suggest that an appropriate flexibility of anionic sidechains could be vital for high proton mobility in PEMs under minimal hydration conditions and at high anionic density.

R L. Hayes et *al* [198] used Car-Parrinello Molecular Dynamics (CPMD) [189] and the path integral formalism of CPMD (PI-CPMD) [192-194] to simulate mono [195], di [196], and tetra [197] hydrate trifluoromethane sulfonic acid systems. The studies revealed quantum effects that facilitate proton transfer to the 'presolvated' water or SO_3^- in the first solvation shell and increase the likelihood of formation of $H_5O_2^+$ in all the defects studied [198]. Long range PT was not observed in any of the simulations due to the constraints imposed by the crystal structures but transient transfer was observed. For both di hydrate and tetra hydrate system, quantum effects were found to lower the proton transfer barrier in the free energy profiles. Hence, the Zundel character of proton increases facilitating proton transfer to the neighboring water molecule.

Same authors [199] studied proton transfer in model system of pentahydrate trifluorosulfonic acid using PI-CPMD implemented in CPMD. AIMD simulations reveal that the proton defect is most likely to transfer to the closest water that has the expected presolvation and only contains water in its first solvation shell. No evidence was found

for the proton preferentially transferring to a water molecule bridging two of the sulfonate groups as in the case of tetrahydrate of trifilic acid.

Proton Transport in Pores

Qualitative comparison of effects of different environment on reaction potential surfaces was introduced by Warshel's Empirical Valence bond (EVB) [166]. Kornyshev *et al* [201, 202] analysed the relationship between pore structure and proton ransfer dynamics as a function of PEM hydration and sidechain density. They proposed a locally polarizable two-state empirical valence bond (EVB) model [201]. It was utilized to study the proton dynamics in a single pore of a PEM. The EVB approach provides an adequate compromise between physical accuracy and computational effectiveness, thus allowing studying non-classical proton transport on extended time scales. It is widely used to study proton transfer events. In their simulation [200], the authors focused on proton dynamics and neglected large-scale polymer dynamics assuming rigid backbone walls. The basic unit of the polarizable two-state EVB model used was the $H_5O_2^+$ ion. This complex can be represented as a superposition of two equivalent basis state complexes, $H_3O^+.H_2O$ and $H_2O.H_3O^+$. The proton transfer coordinate was defined as $q = r_1 - r_2$, where r_1 and r_2 are the distances of the central protons to the oxygen atom positions of the neighbouring water molecules as shown in Figure 3.6. The value $q = r_1 - r_2 = 0$ refers to a symmetric $H_5O_2^+$ ion and $|q| > 0.5$ Å corresponds to the decomposition of the $H_5O_2^+$ ion into H_3O^+ and H_2O.

Considering systems with high proton concentration was possible due to the local nature of the coupling between the two basis states and the introduction of an empirical charge switching function. Slab-like pores with unit cell size of 2-5 nm and fixed width of 25 Å were considered that contained several hundred or thousand water molecules and 40-80 protons. Ionomer backbones were described by an excluded volume with a strong repulsive interaction in the form of a Lennard-Jones interaction potential. Three systems with λ between 14 and 39 were simulated. Simulated systems differ in interfacial charge density due to the varying number of protons. Charge densities varied to mimic ionomers with different IECs. From the simulations, it was found that when λ increased, the proton diffusion coefficient increased. On the other hand, when the surface charge density

increased, the concentration of protons would increase leading to a steeper increase in proton concentration towards the interfaces due to mutual proton repulsion in the bulk region. These trends are consistent with predictions of the Poisson-Boltzmann theory. Larger local proton concentrations in the interfacial region increase the likelihood of ion pair formation between H_3O^+ and SO_3^- ions. Formation of such ion pairs at the sites of fixed SO_3^- ions reduces the overall proton mobility as observed by the decrease of diffusion coefficient with decreasing λ. The total conductivity of the membrane is approximately proportional to the product of proton concentration and diffusion coefficient. Proton hopping times were found to be independent of water content and similar to the corresponding times found in bulk water [200].

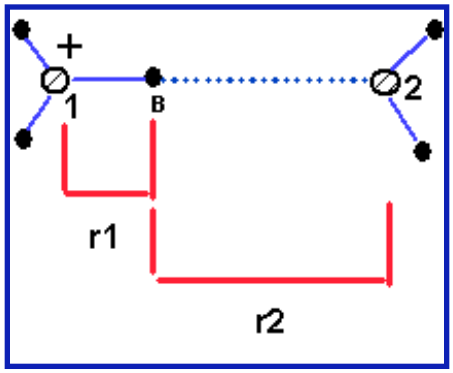

Figure 3.6: Schematic representation of Zundel ion, $H_5O_2^+$. Adapted with permission from E. Spohr, P. Commer, and A. A. Kornyshev, *J. Phys. Chem. B*, 2002, 106, 10560. Copyright 2002. American Chemical Society.

A phenomenological model of a single pore with planar geometry was considered by Eikerling et al [203]. The mobility of protons was assumed to occur via two mechanisms: surface mechanism and bulk mechanism. In the surface mechanism, the proton moves along the array of acidic head groups via structural diffusion at the interface. In the bulk mechanism, the protons are transported by structural diffusion. With assumed plane geometry, they showed that the work terms due to interactions of the protons with the fixed anionic surface groups contribute significantly to the activation energy of the surface mechanism. These work terms vanish in the central region of the pore, resulting in bulk-like proton mobility with low activation energy.

Proton transport and effects of interfacial charge distributions on proton mobility in a PEM using continuum theory and molecular dynamics simulations was done by Commer et al [202]. They calculated proton diffusion in a single pore assuming a slab-like geometry. Their aim was to understand the effect of hydration on the activation energy of proton transport and compare with experimental results. For molecular dynamics, the temperature, and slab width, L, have been varied systematically. Varying L and keeping the number of protons constant during simulations is equivalent to the polymer phase was modelled through combination of a Lennard-Jones (LJ) wall and a dynamic grid of SO_3^- groups, which have some lateral mobility. The SO_3^- can move within average distance of $\sqrt{\langle r^2 \rangle} \approx \sqrt{1\text{Å}^2}$. Cylindrical pores with radii 8 ≤ R ≤ 15 Å were considered to represent low (λ =4) to high (λ= 20) water contents. Extensive simulations were run in the temperature range 233 K < T < 413 K. The pore width L was varied between 8 and 21Å. Self-diffusion coefficients of the proton Dσ were calculated for the slab model from the mean square displacement in both x and y directions. The EVB model used for molecular dynamics (MD) simulation of proton transport in pores was similar to the one proposed before [201]. MD results suggested that there is no distinction between bulk and surface processes and even at low λ the activation energy (AE) and thus the transport process are found to be bulk-like.

In order to understand this surprising result from MD, the authors did refined analytical calculations based on a modified Poisson-Boltzmann approach, in which they accounted for finite proton size, smearing of charges on sulfonic acid groups (SO_3^-) and thermal motions of (SO_3^-) and sidechains. This reduces the Coulomb barriers for proton transport near the surface. Steric repulsion from the pore surface introduced through an empirical Lennard-Jones potential (LJ) to produce an excluded volume for proton complexes next to the surface. These modifications lead to a good agreement between modified Poisson-Boltzmann and MD approach. Activation energies of proton transport were found to be insensitive to pore size.

Coupled Proton and Water Transport

A phenomenological random network model was introduced by Eikerling *et al* [203]. They assumed a hydrated morphology of PEM based on the structural model of Gierke et al [39-41]. They demonstrated the importance of connectivity of the pores and the coordination of the water in the pores to the overall conductivity of the membrane. It was concluded based on the proposed random network model that PEMs with higher elasticity of the polymer phase would swell more homogeneously resulting in good connectivity of the pores and hence better conductivity.

Types of Water in PEMs: Experimental Evidences

In PEM systems, the different states of water are distinguished as surface water and bulk water. The distinction between surface and bulk water was exploited in the work of Eikerling *et al* [203, 204, 205].This distinction is based on the strength of hydrogen bond interaction between water molecules and acidic surface groups at the interface. Surface water interacts strongly through electrostatic interaction with the surface groups. On the other hand, bulk-like water is found to have similarity in dynamics to free liquid-like water. This type of distinction is capable of explaining the Arrhenius plots from Cappadonia *et al* [37, 91] which is shown in Fig 3.2. At water contents $\lambda > 10$, the activation energy of proton transport in PEM is found to be around 0.1 eV. At water contents below $\lambda \sim 3$, increases by about a factor of 3 to > 0.35 eV. Cappadonia *et al* observed the same freezing point suppression in Arrhenius plots of conductivity data [37, 91]. This phenomenon was explained as an effect of the nanoscale confinement that leads to increase in activity of water in small pores.

The local environment of water in ionic pores can be studied using differential scanning calorimetry (DSC) [85, 86], which probes thermal transitions. From such studies, water molecules have been found to have varying levels of interaction with the ionomer. Accordingly, water within Nafion membrane was classified as either freezable bound water, nonfreezable water or free water [88-90]. Nonfreezable water is composed of molecules that are strongly associated with either the polymer backbone or ionic

groups. These water molecules show no thermal transitions. Freezable water can be found in secondary and higher hydration shells around sulfonic acid groups.

Pulsed field gradient (PFG)- NMR was utilized in the group of Zawodinski *et al* and Kreuer *et al* [74, 76] in order to study the self-diffusivity of water in the membrane as a function of water content, λ.

Quasi elastic neutron scattering experiments (QENS) was utilized by Perrin *et al* [77, 79] for hydrated Nafion® analysed using Gaussian model for localized translational diffusion. They found evidence for two populations of water molecules, viz. water with slow dynamics at small λ ($\tau_{slow} = 500$ ps, $\sigma_{slow} \sim 1$Å) corresponding to water molecules that strongly interact with the sulfonic acid groups and water with dynamics. For the latter type, the long-range diffusion coefficients $D_{lr}=(5.1\pm0.5)*10^{-6}cm^2s^{-1}$, is almost bulk-like if corrected for the impact of confining pore dynamics.

Interfacial Proton Transport

Interfacial proton transport has been studied intensively in experiments at biomembranes and Langmuir monolayers. It was concluded from experiments that long-range proton transport along the surface of bio membranes and at monolayers is strongly dependent on the mutual distance between protogenic surface groups (SGs) at the interface [214-219]. A dramatic increase in interfacial proton conductivity was observed upon approach of a critical SG distance of ~7 Å.

At Langmuir monolayers, the surface potential was found to increase sharply when a critical density of the surface groups was reached [214-219]. This has been observed for various compounds such as fatty acids and fatty alcohols [219], phospholipids [214], conducting polymers [220], also for protein: Bovine serum albumin [227].

A theoretical work explained the occurrence of critical surface group separation, A_{SG} based on geometrical model and using 1D model for PT at the interface [222]. Fichet et al [223] utilized curves of surface pressure vs. area and surface potential vs.

area to study the organization of dithiolium-TCNQ salts (TCNQF4-, I-, TCNQ-) as a function of pH and temperature. Plots of surface potential and surface pressure vs. molecular area revealed a small increase in surface potential and a linear decrease of the ellipsometric angle as the area per SG, ASG, decreased from 110 to 87 $Å^2$ for 1,2-dithiolium-TCNQ. For dithiolium-TCNQ salt, both the onset of surface potential and change in ellipsometric angle occurs at same critical area, 110 $Å^2$. Upon further compression, a drastic change in surface potential was observed when ASG decreased from 72 $Å^2$ to 61 $Å^2$. Dithiolium-TCNQ salt found to exhibit both monolayer organization and multilayer formation due to special anion-cation arrangement (Figure 3.7).

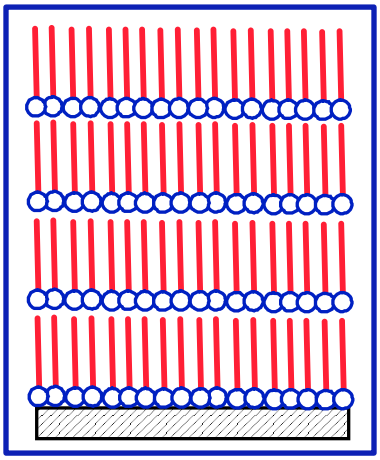

Figure 3.7: A multilayer formation of Dithiolium-TCNQ salt.

For 1,2-dithiolium- $TCNQF_4^-$, a surface potential jump ($\Delta V \equiv 390 \pm 10$ mV) was noted at A_{SG} = 81 $Å^2$ and ΔV was found to increase linearly during compression and attained a maximum value of 440 ± 10 mV at 64 $Å^2$. Plots of surface pressure (π), surface potential (ΔV) ellipsometric angle ($\delta\Delta$) as functions of A_{SG} for 1, 2-dithiolium-I confirmed the formation of a gaseous state of the monolayer for A_{SG}= 77 $Å^2$. A surface potential jump of ($\Delta V \equiv 390 \pm 10$ mV) occurred at A_{SG}= 77 $Å^2$, ΔV increased linearly up to 560 mV at A_{SG}= 44 $Å^2$ (Figure 3.8).

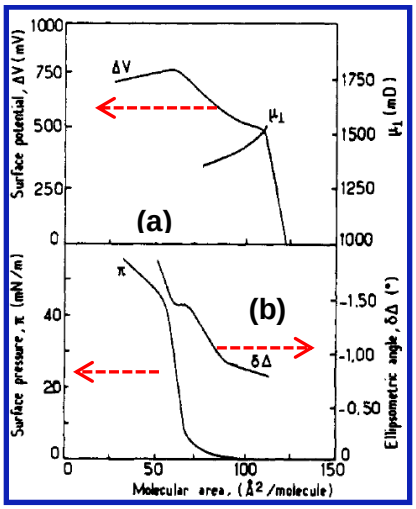

Figure 3.8: Plot of (a) Surface potential (ΔV)-molecular area (A)-normal dipole moment (b) Surface pressure (π)-A-Ellipsometric angle (δΔ) for 1,2-ditholium TCNQ. Reproduced with permission from O. Fichet, D. Ducharme, V. Gionis, P. Delhaès, and R. M. Leblanc, Langmuir, 1993, 9, 491. American Chemical Society. Copyright 1993.

Unwin et al studied the in plane lateral proton diffusion rates along stearic acid monolayers [225]. Scanning electrochemical microscopy (SECM) was utilized to determine the lateral proton diffusion rate at Langmuir monolayers. SECM [226,227] was operated under induced desorption mode (SECMID) [227]. The SECMID method uses a disk-shaped ultra-microelectrode (UME) that is positioned in the aqueous sub phase in a Langmuir trough at a small distance d, below the air/stearic acid/water interface. This distance is typically of the order of the electrode radius or smaller. The association/dissociation reaction at the interface, involving the surface-bound amphiphile is given by

$$C_{17}H_{35}COOH_{(surface)} \rightleftarrows C_{17}H_{35}COO^{-}{}_{(surface)} + H^{+}{}_{(aq)}. \qquad \textbf{3.3}$$

When a potential is applied to the UME, the equilibrium controlled by the concentration of acid in the aqueous phase is perturbed such that H^+ is reduced to H_2 at a diffusion-controlled rate at the electrode, whence depleting the concentration of protons in the gap between the electrode and the air-water interface. This promotes the deprotonation of surface-restricted stearic acid in a spot of similar dimensions to the UME, generating a radial surface proton concentration gradient that provides the driving

force for lateral proton diffusion. Under well-defined mass-transport conditions of SECM, the three steps, protonation/deprotonation, solution diffusion, and surface diffusion could be resolved for the full range of surface pressures. The transient measurements enable both the lateral diffusion coefficient and the protonation/deprotonation rates to be determined.

The surface diffusion rate depends on the degree of compression of the monolayer. The maximum surface diffusion coefficient of 1.2 (± 0.1) 10^{-5} cm^2s^{-1} was found at a pressure of 9-10 mNm^{-1} corresponding to A_{SG} = 26 $Å^2$. Further compression of the monolayer caused the surface diffusion rate to decrease again. This observation is consistent with the prediction of an optimum intermolecular separation for the formation of an H-bonded network at the monolayer surface [213, 229].

Lateral proton diffusion along membrane surfaces represents an efficient system for proton movement. However, the proton diffusion along membrane surfaces has been a subject of continuous debate. Heberle et al [207] used surface-bound pH indicators to measure light-induced pH changes on the extracellular and cytoplasmic surface of the purple membrane. The pH changes detected on the cytoplasmic side were slower than on the proton release side, but clearly faster than those measured in the aqueous bulk phase. These data was interpreted as due to fast proton migration along the purple membrane surface to the opposite side with retarded surface-to-bulk transfer. It was expected that if the protons do move along the membrane surface, the lateral diffusion should be mediated by the surface-bound acidic and basic residues such as lipid head groups. The dwell time of protons on lipid head groups was shown to increase with their pKa. This implies that lateral proton movement depends on the pKa of the lipid head groups. The diffusion coefficient measured was found to be D = 9.7 X 10^{-7} cm^2 / s.

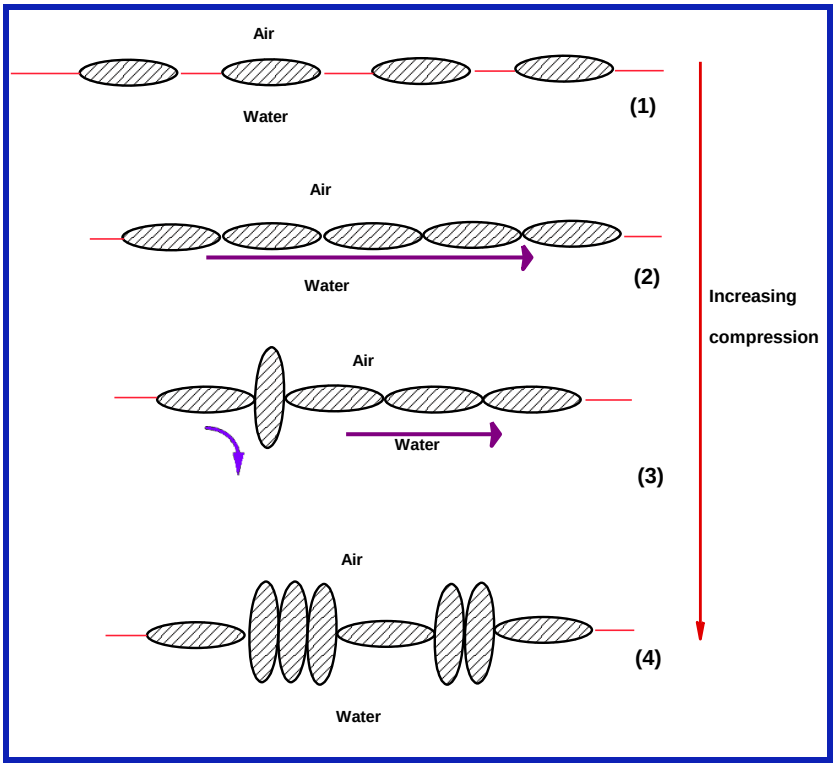

Figure 3.9: Various events that occur during film compression of BSA at air / water interface. (1) Represents the situation where in the protein lie flat at the interface, no conduction. (2) as the compression increases, formation of molecular assembly of continuous layer of interfacial water is created which facilitates long range lateral conduction (long arrow). (3) local break in conduction due to some molecules assuming upright position prevents lateral transfer locally. (4) Upon further compression i.e. at high packing density, more and more protein molecules assume upright orientation and associated increase in defect prevents long range proton conduction. Adapted from B. Gabriel, and J. Teissie, *Proceedings of the natural academy of sciences* USA. 1996, 93, 14521.With permission. Copyright 1996.

Lateral conduction mechanism is also found in proteins such as Bovine serum albumin at the air/water interface [230]. Investigation of proton conduction in protein, Bovine serum Albumin (BSA) has done using two complementary methods. Thefirst method is direct method, in which fluorescein dependent FITC-BSA was used (FITC = Fluoroscein isothiocyanate). The second method monitors the surface electrical conductance. In both the fluorescein method, and in surface electrical conductance method, fast lateral conductivity around critical area of 400- 300 nm^2 below 300 nm^2

conductance disappeared. This explains that film organization controls the conduction. For BSA protein the decrease of conduction upon increase in pressure was suggested to be due to reorganization of protein molecular assembly below 300 nm^2/ mol. The reorganization results in mismatch of neighbour to neighbour transport that decreases both the electrical and proton conductivity at high packing density as shown in Figure 3.9.

The measurement of the UV reflection spectrum has allowed Ahuja et al [231] to probe interactions between dimyristoylphosphatidic acid (DMPA) and tetracation cyclobis(paraquat-*p*-phenylene) (BBP4+) molecules at the air/water interface. In this method, only those molecules that resonantly contribute to the enhanced surface reflection are detected. In general, the reflectance displayed a sharp increase at 100 $Å^2$, similar to ΔV-A isotherms for these compounds. Major features of the isotherms namely, expansion at low surface pressure and contraction at high surface pressure together with dependence of the expansion and contraction isotherms on molar ratio of BBP_4^+: DMPA explained using lipid / adsorbate interaction model. Relative merits of adsorption vs. cospread monolayer methods were analyzed. The diffusion coefficient for BBP_4^+ was calculated to be 3.75 X 10^{-6} cm^2/s, giving a Nernst layer thickness of 0.033 cm.

Investigating the proton migration along the surface of bacteriorhodopsin micelles and its delayed transfer from surface to bulk was studied by Scherrer *et al* [236]. The deprotonation rate detected with fluorescein attached to the extra cellular surface was found to be 22 ± 4 µs faster than that measured with pyranine in the aqueous bulk phase: 125 ± 10 µs. In the cytoplasmic loop region, the protonation rate was 61 ± 10 µs, even though it is slower by a factor of 3 than at the deprotonation side, but still found to be faster than that measured with pyranine in the bulk phase. This result suggests that the released protons are retained on the micellar surface and move rapidly along the surface to the cytoplasmic side than from the surface to the bulk medium.

Occurrence of high proton mobility upon compression of the monolayer below a critical area is explained using a simple geometric model, hydrogen bond data and a unidimensional model for proton transfer (PT) in hydrogen bonds [213]. The formation of strong hydrogen bonds with the anion lattice takes place at A_{SG}. This creates a highly

structured network that allows for rapid proton transfer along the hydrogen bond network. Lateral conductance measurements and surface potential values were explained using Kiefer's model. In this work the authors explained the experimental observations based on hydrogen bond length where PT can occur. The energetics and dynamics of unidimensional proton coordinate under the presence of effective potential is considered.

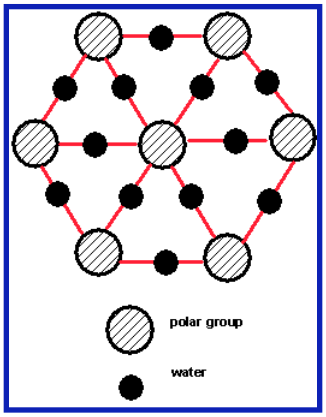

Figure 3.10: Molecular arrangement of hydrophilic groups in interface model proposed by Leite et al. Adapted with permission from V. B. P. Leite, A. Cavalli and O. N. Oliveira Jr., *Phys. Rev. E,* 1998, 57, 6835. Copyright 1998. American Physical Society.

A simple model was developed for obtaining comparable results with experiments. In this model, the polar part of the amphiphilic molecules in the films arranged in a bidimensional triangular lattice as shown in Figure.3.10. Water molecules were thought to be present between polar groups through which a net of H bonds are formed. A simple geometric model for the configuration of these molecules was assumed, as illustrated in Figure.3.11. The critical area for fatty acids corresponds to a distance of 7.1 Å between polar heads (A_{SG} = 38 Å^2). This configuration corresponds to a distance of R =2.8 Å. Below R a net with strong H bonds is formed. The H-bond strength increases exponentially with decreasing R. This suggests that the dramatic increase in the conductance below the critical area is due to a "hop-and-turn" mechanism of PT. In this model, the two oxygen atoms involved in the proton transfer are treated equivalently. This is an approximation, since one oxygen belongs to a water molecule, and the other to a hydrophilic head group.

There appears no single consistent definition of a Soliton. It is generally defined as self-reinforcing solitary wave. Mathematically, it is described as a solution of a non-linear evolution equation which at every moment of time is localized in a bounded domain of space, such that the size of the domain remains bounded in time while the movement of the centre of the domain can be interpreted as the movement of a particle.

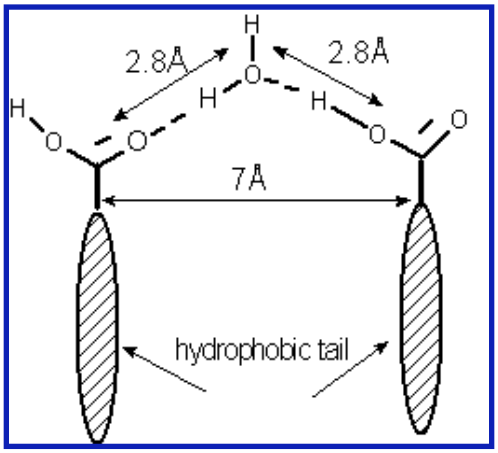

Figure 3.11: Geometric arrangement necessary for the PT to occur in stearic acid monolayers. Adapted with permission from V. B. P. Leite, A. Cavalli and O. N. Oliveira Jr., *Phys. Rev. E,* 1998, 57, 6835. Copyright 1998. American Physical Society

A soliton model [232-235] for proton conduction in quasi-unidimensional hydrogen bonded networks was presented by Bazeia et al [232]. In order to investigate proton conductivity in Langmuir films, the model presented in [235] was extended to the case of a three-component chain. In this model, the film is considered as an isolated system, and the water substrate alone provides hydration that participates in the H-bond network. No specific crystalline structure was assumed for the hydrated water. In this model, hydrogen bonds connect the hydrophilic head groups to the water, enabling a soliton mechanism that drives proton motion. The schematic representation of this model is given in Figure. 3.12.

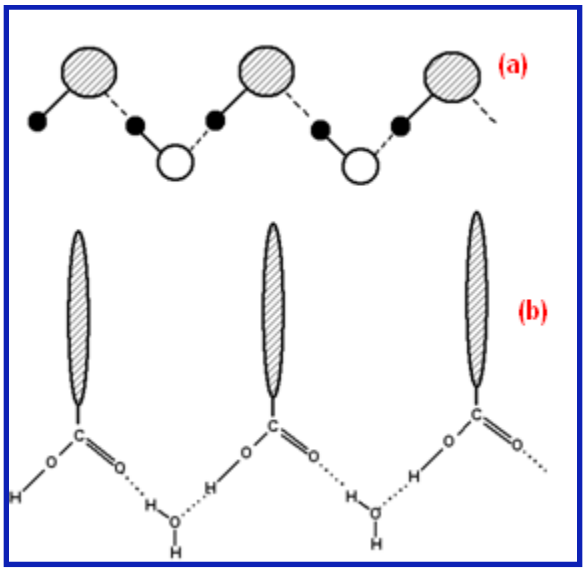

Figure 3.12: Schematic representation of three-component network model. In (a) protons, -OH groups, and head groups of the film are represented by small, medium and large circles respectively. In (b) the same film along with hydrophobic tails is represented. Adapted from D. Bazeia, V. B. P. Leite, B. H. B. Lima, and F. Moraes with permission, Copyright 2001. Elsevier.

Although many models have been proposed, there is still a lack in understanding the lateral transport mechanisms at the molecular level at monolayers and in bio membranes. Studies on biomembranes and monolayers generally focus on acidic surface groups terminated by carboxylic acid due to their importance in the biological context. However, in the context of PEMs, sulfonic acid groups are the most interesting groups. They offer different properties in terms of symmetries of dense hydrogen bonded arrays, resulting in different hydrogen bond strength and different proton transport mechanisms. Recently, experimental study on interfacial proton transport with a view to designing advanced PEM for PEFC was reported by Matsui et al [237]. The authors performed surface pressure and surface conductance measurements at nanosheet assemblies of monolayers with sulfonic acid head groups, fabricated by the Langmuir-Blodgett technique. They found the conductivity of ordered multilayer to be about 1×10^{-5} Scm^{-1}at 100 % RH and 20°C that increased to 1×10^{-2} Scm^{-1} at 70°C.

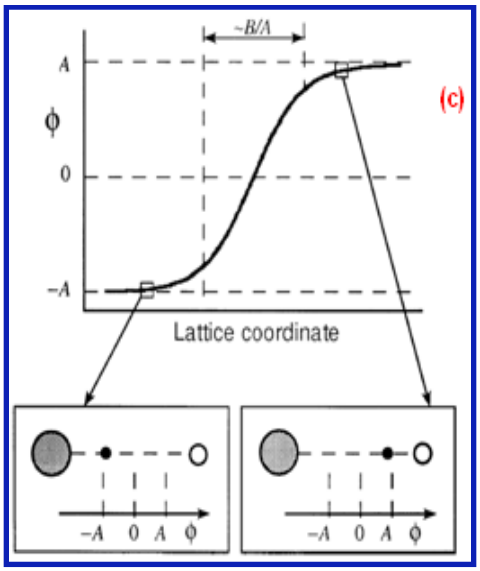

Figure 3.13: Schematic representation of three-component network model. (c) Presented soliton solution corresponding to the width, l ~ B / A with translational motion of proton φ. Adapted from D. Bazeia, V. B. P. Leite, B. H. B. Lima, and F. Moraes with permission, Copyright 2001. Elsevier.

Chapter 4. Objectives and Model System

4.1. Objectives and Model System

The high proton conductivity (~ 0.1 S cm^{-1} at 30°C) found in currently utilized polymer electrolyte membranes at high hydration levels is due to a combination of high concentration of mobile protons, high mobility of protons in bulk-like water and the excellent connectivity of the water-containing network of pores [37, 75, 150, 159, 187, and 202]. At low hydration levels and at elevated temperatures (> 80ºC), pathways containing bulk-like water cease to span the whole sample and hence conductivity decreases. Under such conditions, the PEM morphology and the transport mechanisms of protons and water change drastically as observed in experiments [62,235,236] and rationalized in theory [187, 203, 237,238].

Various efforts at the materials science front have explored the design and fabrication of anhydrous proton conductors that are completely independent of the presence of water for their performance [243,244,245,247] or membranes that could provide sufficient proton conductivity under minimal hydration [245,246]. These materials help in expanding the operational range flexibility of fuel cells with proton-conducting electrolytes, enabling sustained operation at T > 100ºC [248].

Under minimal hydration conditions, interfacial regions between polymer aggregates and water play a vital role for proton transport mechanisms and performance of PEMs. There is, thus, a need for theoretical understanding of conditions for which aqueous based PEM should attain sufficient proton transport with minimal amount of water that is tightly bound to the stable polymer host. The focus of the present work is on understanding the structural correlations and molecular mechanisms of proton transport at these polymer-water interfaces under minimal hydration (λ=1). We strive to rationalize dependences of lateral proton migration on packing density of proton-binding surface

groups (SGs) tethered to the interface and various parameters such as length, chemical structure and vibrational-orientational flexibility of the polymeric sidechains. A further incentive for these efforts stems from a number of experimental studies, which suggest that proton mobility along cellular membranes and lipid monolayers could be rather high at a critical packing density of protogenic SGs, approaching approximately 1/2 of the value of the proton mobility in bulk water [208,213,250].

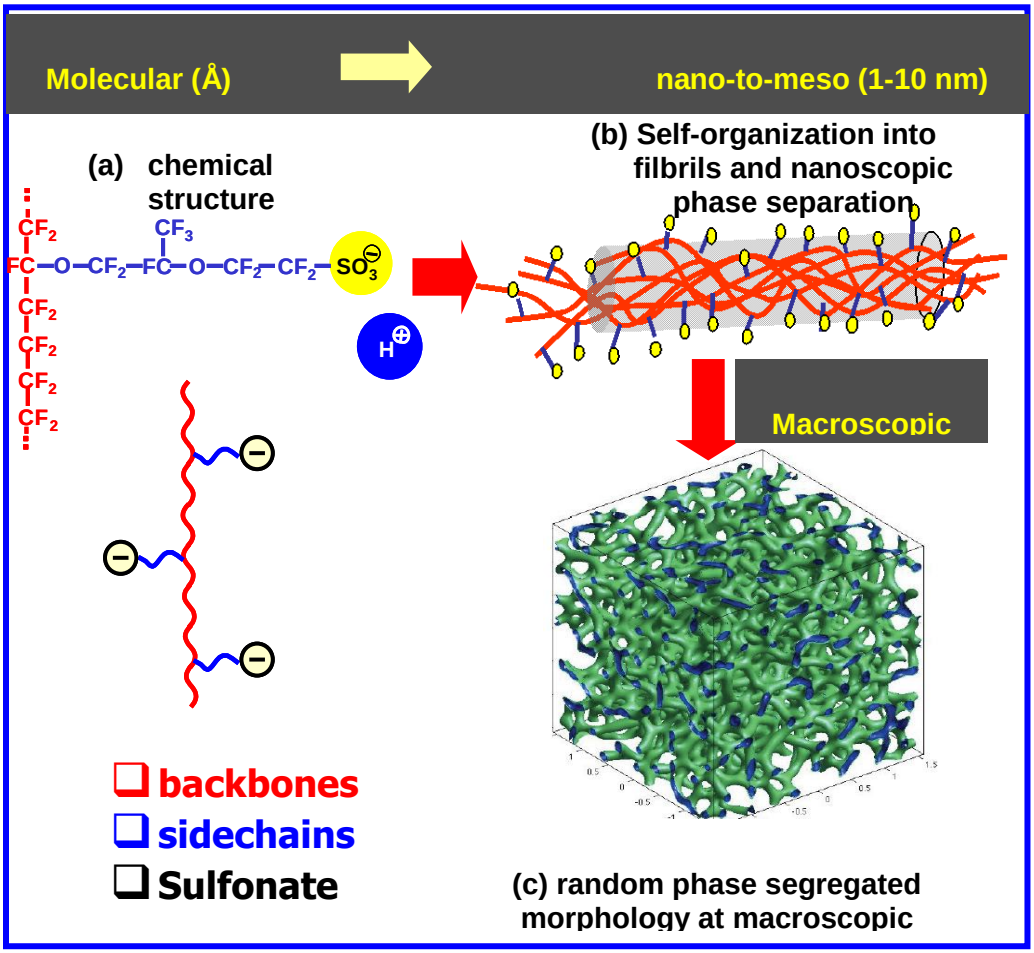

Figure 4.1: Structural evolution in Nafion-type PEMs [235, 262].

We show here in Figure 4.1(a) the molecular architecture of currently utilized membrane, Nafion® which is a copolymer of tetrafluoroethylene backbone with randomly attached pendant side chain terminated by hydrophilic sulfonic acid groups.Upon uptake of water, the hydrophilic part of the polymer interacts with water and hydrophobic part forms aggregates. This creates phase segregation into hydrophobic,hydrophilic and

water filled domains where in sulfonic acid groups at domain interfaces dissociate and release protons to the aqueous sub phase, as illustrated in Figure 4.1(b). As shown in this Figure 4.1, the polymer sidechains remain fixed at the surface of these aggregates thereby, forming charged interfacial layer. Random phase segregated morphology and water filled spaces creates structures at macroscopic scale as given in Figure 4.1(c).

Studying structural correlations and surface-mediated mechanisms of proton transfer in these environments requires methods such as *ab initio* quantum mechanical calculations based on density functional theory (DFT) [253-255]. The structural complexity and rarity of proton transfer events adds complications for quantum mechanical calculations based on DFT. The structural complexity defines the need for simplified model systems to use with advanced computational techniques that allow efficient sampling of rare events [256, 257, 258, 259, 260].

In order to study sidechain correlations and examine direct proton exchange between water and surface groups, molecular level simulations have been utilized by various authors [261,262]. Minimal hydration conditions were also evaluated using tetrafluoromethane sulfonic acid crystals with λ=1 [188].

4.2. Objectives

We aimed for an insightful yet sufficiently simple model system that could incorporate various structural parameters such as the length of sidechains, the number of water molecules added, and the distance between the acidic surface groups. In this work molecular level calculation for a regular hexagonal array of acidic groups in 2D is considered under minimal hydration [263,264].

In our first work, we considered the shortest groups possible, R_i (where R_1=CF_3SO_3H and R_2=CH_3SO_3H) [263], the main parameter varied is the distance between surface groups, d_{CC} and we studied stable structural conformations of the minimally hydrated interfacial array as a function of d_{CC}. Using this model, we have explored the role of chemical architecture and packing density of sidechains on acid dissociation, interfacial correlations, and conformational transitions at the interface. In

our next contribution, we considered sidechains with increasing length. Starting from the shortest group, CF_3SO_3H, we have increased the length of sidechains by adding more CF_2 groups to the more stable interface, CF_3SO_3H, for which R_i-SO_3H with R_3=CF_3CF_2-, R_4=$CF_3CF_2CF_2$- [263].

Finally, the surface groups that mimic sidechain of Dow®/Aquivion® have been considered; R_5=$CF_3OCF_2CF_2$. The separation of fixed end points of SGs on the basal plane was varied in the range of 5 Å < d_{CC} < 20 Å that encompasses the relevant range of variation in prototypical PEMs [41, 56, 57,265].

The second part of calculations deals with the addition of a second layer of water molecules to the minimally hydrated interface. The 2D H_2O layer was considered in two different positions, described as H-up and H-down, corresponding to the preferred orientation of hydrogen bonds. The binding energy of 2D H_2O layer in both the positions to the minimally hydrated interface was evaluated using optimization studies. In these studies, the separation of end points of SGs on the basal plane was varied in the range of 6 Å < d_{CC} < 8 Å. Since the minimally hydrated “upright” interface is no longer stable above d_{CC} > 7 Å, we concentrate reporting the results with binding energy of extra water layer with the tilted interface.

Atomistic models for R_i (with i=2-5) considered in this work are shown in Figures. 4.2 to 4.5. Using optimized energies as indicator, we have analyzed H bond strength, water binding energies, and structural transitions at the interface.

4.3. Model system and Parameters

The model system considered in this work is depicted in Figure 4.6. It emerges from the self-organized morphology of the membrane at the nanoscopic scale indicated as (b) in Figure 4.1**.** The random array of hydrated and ionized side chains is tethered to the surface of aggregated hydrophobic polymer backbones. Relevant structural properties include the shape, thickness, persistence length of aggregates, as well as the chemical properties and packing density of side chains attached to their surface. Various assumptions were made to construct a computationally feasible model. To a first

approximation, the highly correlated interfacial dynamics of side chains, protons and water decouples from the dynamics of the polymeric aggregates. We imply that these supporting aggregates form a fixed frame of reference for the surface groups. Further simplification was made by removing the supporting substrate completely and considering it in first approximation as an inert basal plane. Assurance is made that the acid head groups and water molecules are located on one side of the basal plane only. This treatment is equivalent to describing the polymer aggregates by excluded volume interactions [266]. Even though this model look simplified, it retains essential characteristics for studying structural conformations, stability, and the concerted dynamics of polymer side chains, water and protons at the polymeric aggregates in PEMs.

3 x [$CH_3SO_3H^{\cdots}H_2O$]

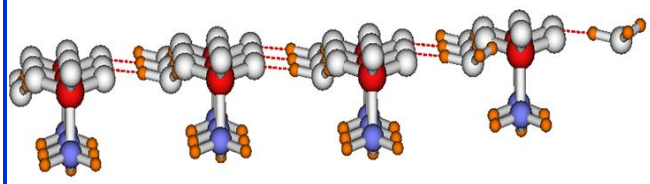

Figure 4.2: Simulated system 3 x [$CH_3SO_3H^{\cdots}H_2O$] in side view

3 x [$CF_3\,CF_2\,SO_3H^{\cdots}H_2O$]

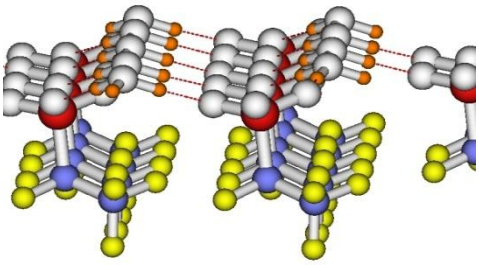

Figure 4.3: Simulated system 3 x [$CF_3CF_2SO_3H^{\cdots}H_2O$] in side view

3 x [$CF_3\,CF_2\,CF_2SO_3H^{\cdots}H_2O$]

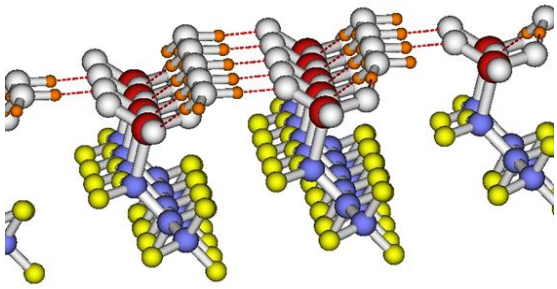

Figure 4.4: Simulated system 3 x [$CF_3\ CF_2\ CF_2SO_3H^{\cdots}H_2O$]

3 x [$CF_3\,OCF_2\,CF_2SO_3H^{\cdots}H_2O$]

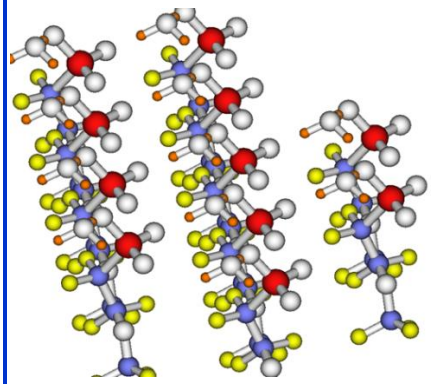

Figure 4.5: Simulated system 3 x [$CF_3OCF_2\ CF_2SO_3H^{\cdots}H_2O$] in side view

This implies that the effect of polymer dynamics on processes inside pores is primarily due to the distribution of sidechains, their protrusion lengths into aqueous

domains, their orientation relative to the basal plane, their flexibility and the corresponding transient charge distributions.

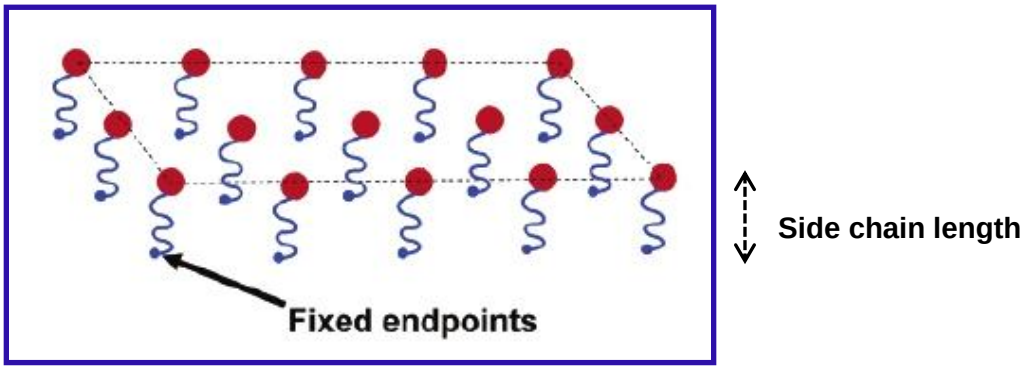

Figure 4.6: Sketch of 2D array of surface groups with terminating carbon atoms fixed at regular positions of hexagonal array on the basal plane. Adapted with permission from S. P. Narasimachary, A. Roudgar, and M. Eikerling. *Electrochimic. Acta.* 2008, 53, 6920. Elsevier. Copyright 2008.

The first set of calculations addressed the impact of substituting the fluorocarbon group in triflic acid by a hydrocarbon group. Results are presented in § 6.2. The computational study and analysis of these results took about 3 months, after the basic model system had been defined. The computations were performed on the Linux clusters PEMFC at SFU and Westgrid computer clusters. The total number of calculations for this part was 42.

In the study of the impact of the length of sidechains, three different systems with increasing size were considered. Results are presented in § 6.3. The larger number of atoms per unit cell led to increased computational times per calculation. Overall, this study was completed in about 9 months. It was performed mainly on Westgrid computer clusters. For R_i=3 the number of calculations performed was 28; for R_i=4 number of calculations performed was 31; for R_i=5 the number of calculations performed was 35.

The study on the effect of adding an extra water layer, reported in § 6.4, took about ~12 months. For these calculations, I have utilized 16 cores on SGI Linux clusters on WESTGRID. The number of calculations performed was 11 for each configuration.

Chapter 5. Computational Methods

5.1. Computational Methods

In this chapter, various computational methods used in our calculation will be described as briefly as possible. In principle, all physical and chemical properties of a system can be derived from its Hamiltonian. The proper description of quantum mechanical systems requires solving the Schrödinger equation. The exact solution of the Schrödinger equation is impossible for a macroscopic system with N ~ 10^{23} electrons. Through several simplifying assumptions and approximations the complexity of macroscopic systems could be reduced. For ordered systems with repeating units, a periodic super cell approximation can be used, by reducing the size of the system that must be simulated explicitly.

5.2. The Schrödinger equation

For a system of N interacting electrons at positions $\vec{r}_i$ with M nuclei at positions, $\vec{R}_I$, the exact ground state energy is obtained from the solution of Schrödinger equation

$$\hat{H}\Psi\left(\{\vec{r}_i\},\{\vec{R}_I\}\right)=E\Psi\left(\{\vec{r}_i\},\{\vec{R}_I\}\right), \qquad \textbf{5.1}$$

where the Hamiltonian operator $\hat{H}$ is given by

$$\hat{H}=-\frac{1}{2m_e}\sum_{i=1}^{N}\nabla_i^2-\frac{1}{2\mathrm{m_I}}\sum_{I=1}^{M}\nabla_I^2-\sum_{i=1}^{N}\sum_{I=1}^{M}\frac{Z_I}{|\vec{r}_i-\vec{R}_I|}+\frac{1}{2}\sum_{i=1}^{N}\sum_{i\neq j}^{N}\frac{1}{|\vec{r}_i-\vec{r}_j|}\ +$$

$$\frac{1}{2}\sum_{I=1}^{M}\sum_{I\neq J}^{M}\frac{Z_I Z_J}{|\vec{R}_I-\vec{R}_J|}, \qquad \textbf{5.2}$$

where m_e represents the mass of electrons and m_I the mass of nuclei. In the above Eq. 5.2, the first two terms represent kinetic energy operators of electrons and nuclei respectively. Third, fourth and the fifth term represent the potential energy operators for electron-nuclei interactions, electron-electron interactions and for the nuclear-nuclear interaction, respectively. Since the operator of nuclear-electron interaction energy is a function of position coordinates of nuclei and electrons, separation of this term becomes impossible. Based on the mass difference between nuclei and electrons also, nuclei being heavier compared to electrons, their velocities are much lower than those of the electrons. Approximation based on the mass ratio of the electrons and nuclei is given in terms of Born-Oppenheimer approximation.

5.2.1. Born-Oppenheimer Approximation

The Born-Oppenheimer approximation (BO) [267] decouples dynamic of nuclei and of electrons; it takes advantage of the large ratio of the masses of atomic nuclei to the mass of an electron. This implies that time scales of electron dynamics are larger by the inverse factor. In this approximation, the nucleus acts as a static charge acting as an electrostatic potential on electrons.

Therefore, the electronic structure problem for the condensed phase or a molecular system can be solved in an iterative way. For a fixed configuration of atomic nuclei, the quantum mechanical electronic structure problem is solved. Using the electronic charge density distribution obtained, the classical force field for the given configuration of nuclei can be calculated and the subsystem of nuclei is propagated by a single time step according to classical Newtonian equations of motion. In this approximation, the wavefunction of a molecule is written as a product of the wavefunction of nuclei and a many body wavefunction of electrons.

The Hamiltonian operator for electrons can be written as

$$\hat{H}_{el}\Phi\left(\{\vec{r}_i\}\right) = E_{el}\Phi\left(\{\vec{r}_i\}\right), \qquad \textbf{5.3}$$

where $\hat{H}_{el}$ the Hamiltonian operator is given as

$$\hat{H}_{el} = -\frac{1}{2m_e}\sum_{i=1}^{N}\nabla_i^2 - \sum_{i=1}^{N}\sum_{I=1}^{M}\frac{Z_I}{|\vec{r}_i - \vec{R}_I|} + \frac{1}{2}\sum_{i=1}^{N}\sum_{i\neq j}^{N}\frac{1}{|\vec{r}_i - \vec{r}_j|} \quad . \qquad \textbf{5.4}$$

The nuclear coordinates $\{\vec{R}_I\}$ in Eq. 5.1 do not act as variables but as parameters that define the electronic Hamiltonian. The eigenvalue, $E_{el}(\{R\})$ obtained as the solution of the electronic Schrödinger equation in Eq. 5.2 acts as the potential for the motion of nuclei. $E_{el}(\{R\})$ is called the Born-Oppenheimer energy surface. The equation of motion of nuclei is solved using Newton's classical equation of motion,

$$M_I \frac{\partial^2}{\partial t^2} R_I = -\frac{\partial}{\partial R_I} E_{el}(\{R\}). \qquad \textbf{5.5}$$

5.2.2. Hohenberg-Kohn Theorems

Density functional theory (DFT) reduces the many-body problem of N interacting electrons having 3N spatial coordinates to a problem that involves only 3 spatial coordinates through the use of functionals of the electron density; in other words, the formalism of DFT converts a system of N interacting electrons to a system of N non-interacting electrons under the influence of an effective potential, V_{eff}, such that these two systems are equal at the ground state.

Walter Kohn was awarded the Nobel Prize in Chemistry (1998) for his groundbreaking development of DFT. Nowadays, DFT is widely applied to problems in materials chemistry, biochemistry [268], electrochemistry [269], and condensed matter physics [270]. Also, DFT is the most widely employed electronic structure method in computational chemistry, solid state physics and materials science [271]. In chemistry, DFT can predict molecular properties such as molecular structures, vibrational frequencies, ionization energies, electric and magnetic properties, and reaction paths, to name a few.

DFT is a ground state theory. It is based on the Hohenberg-Kohn theorems [272]. The first theorem may be stated as: the electron density $\rho_0(r)$ uniquely determines the

external potential $\hat{V}_{ext}$ (to within an additive constant). It follows from the above statement that the electron density uniquely determines the Hamiltonian operator for a given system of nuclei and electrons that can be written as

$$\hat{H}_{el}=\hat{T}+\hat{V}_{ee}+\hat{V}_{ext} \qquad \textbf{5.6}$$

where, $\hat{T}$ and $\hat{V}_{ee}$ are the kinetic energy and electron-electron interaction energy operators.

The second theorem establishes the variational principle: For any positive trial density, ρ_t such that, $\int \rho_t(r)dr = N$ then

$$E[\rho_t] \geq E_0 \qquad \textbf{5.7}$$

The proof of the second theorem is straight forward. From the first theorem we know that the trial density determines a unique trial Hamiltonian (H_t) and thus the wavefunction (Ψ_t) that follows from the variational principle

$$E[\rho_t] = \langle \Psi_t | H | \Psi_t \rangle \geq E_0 . \qquad \textbf{5.8}$$

This theorem restricts the density functional theory to studies on ground state properties.

These two theorems lead to the fundamental relation of density functional theory,

$$\delta\left[E[\rho] - \mu\left(\int \rho(r)dr - N\right)\right] = 0, . \qquad \textbf{5.9}$$

that is, the ground state energy and density correspond to the minimum of some functional $E[\rho]$ subject to the constraint that the density contains the correct number of electrons. The Lagrange multiplier of this constraint is the electronic chemical potential, μ .This implies that there is a universal functional $E[\rho]$ which does not depend on the

external potential which represents the particular system of interest and which if we knew its form, could be inserted into the above Eq. 5.9 and minimized to obtain the exact ground state density and energy.

5.2.3. The Energy Functional

From the form of the Schrödinger equation, we see that the energy functional contains three terms, the kinetic energy, the interaction with the external potential and the electron-electron interaction. We can write the energy functional as

$$E[\rho] = T[\rho] + V_{ext}[\rho] + V_{ee}[\rho], \qquad \textbf{5.10}$$

where, the external potential interaction $V_{ext}[\rho]$ is trivial:

$$V_{ext}[\rho] = \int \hat{V}_{ext}\,\rho(r)dr, \qquad \textbf{5.11}$$

but the kinetic and electron-electron functionals are unknown.

Kohn-Sham proposed an approach to approximating the kinetic and electron-electron functionals. They introduced a fictitious system of N non-interacting electrons to be described by a single determinant wavefunction in N orbitals ϕ_i. In this system the kinetic energy and electron density are known exactly from the orbitals

$$T_S[\rho] = -\frac{1}{2}\sum_{i}^{N}\langle \phi_i | \nabla^2 | \phi_i \rangle . \qquad \textbf{5.12}$$

Equation 5.12 represents the kinetic energy of a system of non-interacting electrons that can produce the true ground state density

$$\rho(r) = \sum_{i}^{N} |\phi_i|^2 . \qquad \textbf{5.13}$$

Since a significant component of the electron-electron interaction will be the classical Coulomb interaction or Hartree energy

$$V_H[\rho] = \frac{1}{2}\int \frac{\rho(r_1)\rho(r_2)}{|r_1 - r_2|} dr_1 dr_2 . \qquad \textbf{5.14}$$

Hence, the energy functional can be rewritten as

$$E[\rho] = T_s[\rho] + V_{ext}[\rho] + V_H[\rho] + E_{xc}[\rho] . \qquad \textbf{5.15}$$

The utility of density functional theory rests on the approximation used for the exchange-correlation functional $E_{xc}[\rho]$.

5.2.4. Exchange-Correlation Functional

The non-local exchange-correlation functional $E_{xc}[\rho]$ is not known exactly. The reliability and accuracy of DFT implementations depends crucially on the exchange-correlation functional.

The exchange correlation functional $E_{xc}[\rho]$ in general form is written as

$$E_{xc}[\rho] = \int d^3r \; \rho(r) \; \varepsilon_{xc}[\rho](r), \qquad \textbf{5.16}$$

where $\varepsilon_{xc}[\rho](r)$ is the exchange-correlation energy per electron at the point r which depends on the entire electron density distribution $\rho(r)$. Since the exchange-correlation functional $E_{xc}[\rho]$ is usually not known, the exchange correlation energy $\varepsilon_{xc}[\rho](r)$ cannot be derived either. The exchange correlation energy for systems with uniform electron density is known [273]. Different approximations have been introduced to obtain practically useful expressions for exchange-correlation energies.

5.2.5. Local Density Approximation

In the Local Density Approximation (LDA), the exchange-correlation energy for the homogeneous electron gas is used for non-homogeneous systems [274, 275]. The expression of exchange-correlation energy functional is given as

$$E_{XC}^{LDA}[\rho]=\int d^3r\ \rho(r)\varepsilon_{XC}^{LDA}(\rho(r)). \qquad \textbf{5.17}$$

In a wide range of bulk and surface problems, LDA has been successful [275]. This was thought due to cancellation of opposing errors in the exchange and correlation expression in the LDA. However for chemical reactions in the gas phase and at surfaces, the LDA shows overbinding, which means that binding and cohesive energy turn out to be too large compared to experiment. Due to the overbinding, the lattice constants and bond lengths are smaller compared to the experimental values [276].

5.2.6. Generalized Gradient Approximation

LDA uses the exchange correlation energy for the uniform electron gas at every point in the system regardless of spatial variations in the real charge density. For non-homogeneous charge densities the exchange correlation energy can deviate significantly from that of obtained in LDA approximation. LDA has been shown to be clearly inadequate for certain system and properties. For instance, DFT calculations of O2 using LDA gave a binding energy of 7.3 eV which significantly exceeds the experimental value of 5.23 eV [276].

In advanced DFT approaches, the exchange correlation energy is expressed in terms of local charge density, its gradient and higher order spatial derivatives of the total charge density. A variety of gradient corrections has been proposed in the literature. The generalized gradient approximation (GGA) [276-280] uses the gradient of the charge density defining the exchange-correlation functional by

$$E_{XC}^{GGA}[\rho]=\int d^3r\ \rho(r)\ \varepsilon_{XC}^{GGA}(\rho(r),|\nabla\rho(r)|). \qquad \textbf{5.18}$$

General scaling properties and the asymptotic behavior of effective potentials are taken into account in the construction of the GGA. DFT calculations using GGA achieve good accuracy (error $\leq$ 0.01 eV) for many chemical reactions. Hence, in this work we used the GGA, in particular the approach developed by Perdew and Wang 91, (PW91) [279]. A comparison of different exchange correlational functional results for the binding energy of O_2, obtained using DFT, with the experimental value is given in Table 5.1 [276, 280]. Other GGA functional approaches are those of Perdew, Burke and Ernzerhof (PBE) [280] and revised PBE functional [276].

Table 5.1. **O_2 binding energies obtained from DFT calculations using LDA and various GGA exchange-correlation functionals. Reproduced with permission from B. Hammer, L. B. Hansen and J. K. Nørskov, *Phys. Rev. B,* 1999, 59, 7413.Copyright 1999. The American Physical Society.**

Functional	LDA	PW91	PBE	RPBE	Exp.
O_2 binding energy (eV)	7.30	6.06	5.99	5.59	5.23

5.3. Plane Waves, Pseudopotentials and k points

Plane waves are considered the most obvious basis set to use for calculations of periodic systems. These are equivalent to a Fourier series expansion which is the natural approach to periodic systems. Here, each orbital wavefunctions is expressed as a linear combination of plane waves, which differ in their reciprocal lattice vectors,

$$\varphi_i^K(r)=\sum_G a_{i,K+G}\exp^{(i(K+G).r)} \quad . \qquad \textbf{5.19}$$

One of the potential problems of using plane waves is the calculation of a sum over an infinite number of reciprocal lattice vectors R. Secondly, for a macroscopic lattice there are effectively an infinite number of k points within the first Brillouin zone. Since only valence electrons of an atom are largely responsible for the chemical bonding and most of physical properties, it is reasonable to consider explicitly the valence electrons in the calculation and incorporate core electrons into the nuclear core. One of the problems in

representing valence electrons by a plane wave basis set is that near to the atomic nuclei the wavefunctions of the valence electrons show rapid oscillations. This is due to the requirement of orthogonality of wavefunctions of valence electrons to those of the core electrons. These oscillations give rise to large kinetic energy and a very large number of plane waves would be required to properly model this behavior. However, in the core region the kinetic energy is largely cancelled by the high electrostatic potential energy of interaction with the nucleus. The most common way to deal with these problems is to replace the “true” potential in these core regions with a much weaker pseudopotential [275].

A schematic representation of the pseudopotential approach is shown in Fig. 5.2 [275]. The Kohn-Sham (KS) equations can be solved explicitly for valence electrons only if the core electrons do not participate in the processes under study. A pseudopotential is constructed in such a way that it matches the true potential outside a given radius, designated as the core radius r_c (shown in Fig. 5.2). This method reduces the number of wavefunctions to be calculated. The pseudo wavefunctions corresponding to this modified potential do not exhibit the rapid oscillations of the true wavefunctions in the core region, but with fewer nodes inside the core region, they match the true wavefunction beyond the distance r_c. This reduces the number of plane waves needed for their representation which in turn reduces the scale of the computational problem. The integral of the squared amplitudes of the real and pseudo-wavefunctions over the core region must be identical. This condition is known as norm-conservation [282, 283]. Since the atomic properties of the element should be preserved, including the phase shifts across the core, and since the phase shift depend on the angular momentum and its eigenstates, the pseudopotential should be non-local with projectors for different angular momentum components. The usual form of the pseudopotential is given below [275].

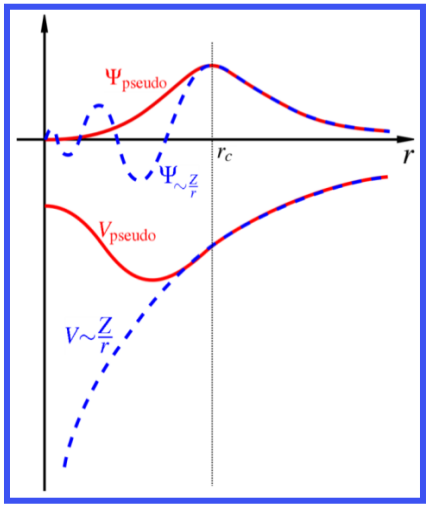

Figure 5.1: Schematic representation of all electron (dashed blue lines) and pseudo potentials (solid red lines) and their corresponding wavefunctions. Adapted with permission from M. C. Payne, M. P. Teter, D. C. Allan, T. A. Arias, and J. D. Joannopoulos. *Rev. Mod. Phys.,* 1992, 64, 1045.

The radius at which all electron and pseudopotential values match is r_c [275].

$$V_{NL} = \sum_{lm} |Y_{lm}\rangle V_l \langle Y_{lm}|, \qquad \textbf{5.20}$$

where $|Y_{lm}\rangle$ the spherical harmonics and V_l are the pseudopotentials for the angular momentum l. Acting on the electronic wavefunction with this operator decomposes the wavefunction into spherical harmonics each of which is then multiplied by the relevant pseudoptential, V_l.

The pseudopotential is constructed such that the scattering properties of pseudo-wavefunctions are identical to the scattering properties of the ion and core electrons. In general, this will be different for each angular momentum component of the valence wavefunction; therefore, the pseudopotential will be dependent on the angular momentum. Pseudopotentials with angular momentum dependence are called non-local pseudopotentials. The most general form of non-local pseudopotential is

$$V_{ion} = \sum_{lm} |Y_{lm}\rangle V_l \langle Y_{lm}|, \qquad \textbf{5.21}$$

where Y_{lm} are spherical harmonics and V_l is the l^{th} angular momentum component of the pseudopotential acting on the wavefunction or in semi-local form,

$$\hat{V}_{SL} = \sum |Y_{lm}\rangle V_{nl}(r) \langle Y_{lm}|, \qquad \textbf{5.22}$$

where $\hat{V}_{SL}$ is the semi-local operator and $V_{nl}(r)$ is the l-dependent model nonlocal pseudopotentials.

The semi-local form has a disadvantage in that it is computationally very expensive, since the number of matrix elements that need to be calculated scales as the square of the number of basis states. If there are N_{pw} in the expansion of the wavefunction at each k-point then the evaluation of V_{ion} will require

$$N_{pw} N_k (N_{pw}+1) / 2 \qquad \textbf{5.23}$$

projectors of the above form (eq. 5.12) to be calculated for each angular momentum component l.

The most common solution is to use the Kleinman-Bylander separable form [284] that reduces the computational cost by reducing the number of projections which need to be performed that scales linearly with the number of basis sets that is given as:

$$\hat{V}_{KB} = \hat{V}_{loc} + \sum_{lm} \frac{|\delta\hat{V}_l \phi_{lm}\rangle \langle \phi_{lm} \delta\hat{V}_l|}{\langle \phi_{lm} | \delta\hat{V} | \phi_{lm} \rangle}, \qquad \textbf{5.24}$$

where $|\phi_{lm}\rangle$ is an eigenstate of the atomic pseudo-Hamiltonian.

For a periodic system, integrals in real space over the infinitely extended system are replaced by integrals over the (finite) first Brillouin zone in reciprocal space, by virtue of Bloch's theorem. According to Bloch's theorem, the wavefunction of an electron, $\psi_{j,k}$

within a periodic potential can be written as a product of lattice-periodic part $u_j(r)$ and a wave-like part $e^{ik.r}$,

$$\psi_{j,k}(r) = u_j(r)e^{ik.r}, \qquad \textbf{5.25}$$

where j indicates the band index and k is a continuous wave vector that is confined to the first Brillouin zone of the reciprocal lattice. Therefore, quantities like charge density can be evaluated using integrals over k-points in the first Brillouin zone. The actual quantum state of the electron is determined by ψ, not by either u or by k. Since k and u are not unique. For instance, if ψ can be written as above in the Eq.5.25, then it can also be written using (k+K), where K is any reciprocal lattice vector. Therefore, wave vectors that differ by a reciprocal lattice vector are equivalent, in the sense that they characterize the same Bloch state.

The first Brillouin zone is restricted to set of k-vectors with the property that no two of them are equivalent, and yet every possible k is equivalent to one and only one vector in the first Brillouin zone. If we restrict k to the first Brillouin zone, then every Bloch state has a unique k.

If there is sufficient space between layers and no electron dispersion in the direction perpendicular to the given plane, the Brillouin zone reduces to a single k-point, the Γ-point. In our calculation, we consider enough vacuum space, ~12 Å between the layers in the direction that is perpendicular to our 2D plane, and also, there is no electron dispersion in this direction (which in our calculation to be Z-axis). For our calculation we used the Γ-point (0, 0, 0) summation of Brillouin zone. Also, since the volume of the unit cell is inversely proportional to the volume of the Brillouin zone, BZ. For a very large unit cell, it is sufficient to represent a single point in the cell which is the Γ-point.

5.4. Simulation Methods

5.4.1. Vienna *Ab Initio* Simulation Package (VASP)

Vienna *ab initio* simulation package (VASP) [252] is a package for performing quantum mechanical simulations at the DFT level [253-255]. This package uses pseudopotentials such as ultrasoft, norm-conserving and projector-augmented plane wave methods along with plane wave basis set. The interaction between ion and electrons are described by the projector augmented wave (PAW) method that allows for significant reduction in the number of plane waves per atom. The projector augmented waves is a technique used in ab initio electronic structure calculations. It is a generalization of the pseudopotential and linear augmented plane-wave methods and allows for DFT calculations to be performed with greater computational efficiency.

Forces and full stress tensor are calculated that aid in relaxation of atoms into their instantaneous ground state.

Geometry optimization of 2D hexagonal array of acidic surface groups of PEMs $[CF_3SO_3^- \cdots H_3O^+, CH_3SO_3^- \cdots H_3O^+]$ (as described in §4.1 and §6.1) was performed using VASP. The exchange correlation effects are incorporated within the generalized gradient approximation (GGA) using the Perdew-Wang (PW-91) functional. The ionic cores are represented by projector augmented waves (PAW). The Kohn-Sham one–electron wavefunctions are expanded in a plane wave basis set with kinetic energy cut-off 400 eV. A Γ- point sampling of the Brillouin zone is used.

As a model system, we considered a hexagonal unit cell with minimal hydration of surface groups viz. $1H_2O$ / SO_3H. In total, the unit cell consists of 3 X [H_2O + R-SO_3H] where R = CF_3, CF_3CF_2, $CF_3CF_2CF_2$, $CF_3OCF_2CF_2$, CH_3. A periodic super cell approach was employed where the unit cell has periodicity along X, Y, Z directions. For interactions between the layers negligible along the Z direction a vacuum space of ~ 12 Å was added. This distance was found to be sufficient to render interactions between neighboring unit cells in this direction negligible. The unit cell consists of $3SO_3H$ and $3H_2O$molecules. The separation between fixed carbon atoms, d_{CC} varied with step width

of 0.35 Å in the range 5 < d_{CC}< 16 Å. The number of atoms per unit cell is 36 for $–CH_3$ (-CF_3), 45 for $–CF_2CF_3$, 54 for $–CF_2CF_2CF_3$ and 57 for the $–CF_2CF_2CF_2OCF_3$ group respectively. The unit cell composition considered in this calculation is shown in Figure. 5.2.

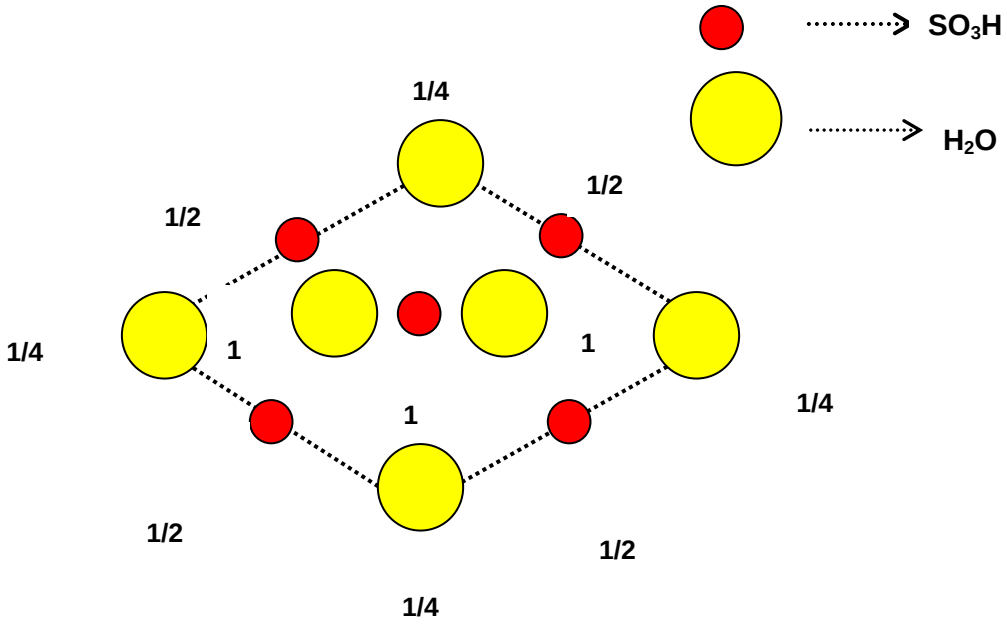

Figure 5.2: Schematic representation of unit cell composition considered in this thesis.

5.4.2. Car-Parrinello *Ab Initio* Molecular Dynamics

Car-Parrinello Molecular Dynamics (CPMD) [285] is an *ab initio* molecular dynamics program. It has parallelized plane wave and pseudopotential code that implements DFT [253-255]. In their seminal paper, Car and Parrinello explained the advantages of unified approach for both MD and DFT. Their idea is to reduce the difficulties in MD simulation of large and disordered system using only an assumption that classical mechanics suffices to describe ionic motion. In Born-Oppenheimer molecular dynamics (BOMD) the nuclear degrees of freedom are propagated using ionic forces that are calculated at each iteration by solving approximately electronic problem using matrix diagonalization scheme.

On the other hand, in the Car-Parrinello method, explicit introduction of a fictitious dynamics of electronic degrees of freedom leads to coupled equations of motion for ions and electrons. This creates a situation where in explicit electronic minimization at each time step is bypassed and after an initial standard electronic minimization, fictitious dynamics of the electrons keeps the system on the electronic ground state corresponding to every new ionic configuration visited and hence yielding ionic forces. The fictitious mass of electrons should be chosen to be small enough to avoid considerable energy transfer from ionic to electronic degrees of freedom and hence maintain adiabatic conditions. Due to the small fictitious mass of electrons, equations of motions are generally integrated using a small time step. The fictitious mass μ is generally kept around 400- 800 a.u. with default time step of 5 a.u. (equivalent to 0.12 fs).

For the part of the calculation where extra water molecules were added to the minimally hydrated interface, we further refined the calculation using geometry optimization studies using CPMD [3x ($CF_3SO_3^{-}\cdots H_3O^{+}$]. For this system, initially geometry optimization was performed using VASP and further optimization was carried out using CPMD with exchange correlation effects incorporated within the functional of Becke, Lee, Yang and Parr, i.e. BLYP[278]. This functional is suited to describe hydrogen bonded systems [278]. This refinment to CPMD was needed due to the larger number of water molecules considered and the higher accuracy of CPMD in describing energetics of hydrogen bonded systems and proton transfer dynamics. In this calculation, Kleinman-Bylander pseudopotentials were used for atomic core regions. The Kohn-Sham one-electron valence states were expanded in a basis of plane waves with cutoff energy of E_{cut} = 80 Ryd = 1088.45 eV, Γ point sampling of the Brillouin zone was used.

In next set of calculation, which aims to explore the orientational fluctuations of the SGs and to study the surface mediated proton transport, we utilize CPMD package [285] and BLYP exchange and correlational functional [278] and Troullier-Martins norm conserving pseudopotential with cut-off of 80 Ryd [287]. The remaining procedure being the same, such as periodic super cell approach, and in the Z-direction, in order to reduce the artificial dipole-dipole interactions, a vacuum space of 12 Å was inserted.

Chapter 6. Results and Discussion

6.1. Structural Optimization of Minimally Hydrated Arrays of Acid-Functionalized Surface Groups

Main observations covered in this chapter include, the effect of changing the chemical side chain group. The main points discussed (in **§6.3**) include the transition point, formation of two different conformations of the surface groups, number of H bonds, and the angle with respect to the basal plane.

In **§6.4**, the effect of length of the side chain on structural changes, transition points will be covered. In **§6.5**, the elementary act of proton transfer in our model system will be discussed, and in **§6.6**, the structure of interfacial array upon addition of monolayer of water is discussed. Also discussed are recent published molecular dynamics results from our group. Finally, the importance of collective H_3O^+ transfer under minimal hydration condition is discussed using solition theory that is proposed by our group.

6.2. Formation Energy and Structural transitions

The previously introduced model system of a minimally hydrated array of acid-functionalized surface groups was considered for obtaining minimum energy structures.

Carbon end atoms of the residual groups are fixed on a basal plane at the positions of a regular hexagonal lattice. For these systems, we have evaluated basic structural transitions as a function of the nearest neighbour separation distance of surface groups (SG). Thereafter, we have studied the impact of a basic chemical modification, comparing R_1= CF_3 with R_2= CH_3. Then we have evaluated and compared

groups of increasing length, i.e. R_i = CF_3CF_2, $CF_3CF_2CF_2$, $CF_3OCF_2CF_2$. In the following discussion we will present and compare results for all of these groups.

The main parameter evaluated for structural studies is the formation energy per unit cell E_f^{uc} , which we have defined as

$$E_f^{uc}=E_{total}(d_{CC})-E_{total}^{\infty}. \qquad \textbf{6.1}$$

$E_{total}(d_{CC})$ and E_{total}^{∞} are the total energy of the system at separation d_{CC} and at infinite separation of surface groups, respectively, as indicated in Figure. 6.1.

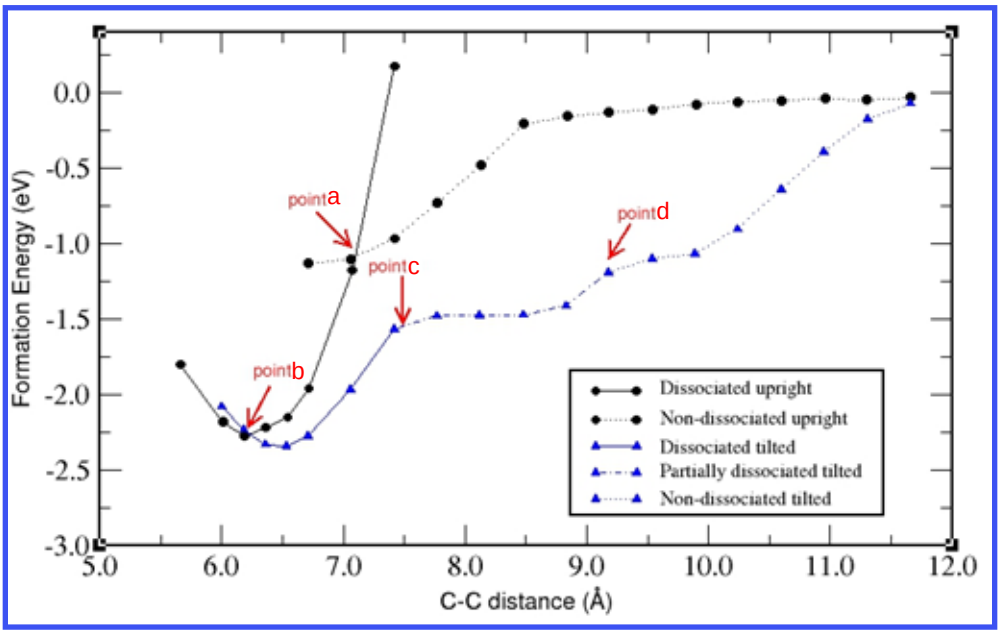

Figure 6.1: Formation energy per unit cell E_f^{uc} , of the interfacial layer of CH_3SO_3H groups as a function of the separation of surface groups, d_{CC} showing "upright" and "tilted" structures respectively. The points refer to structural conformations that are discussed in the text. Reproduced with permission from, A. Roudgar, S.P.Narasimachary and M. Eikerling, J.Phys. Chem. B 2006, 110 20469.

The formation energy represents the energy gained upon bringing three surface groups and three water molecules in the unit cell together from infinite separation. It

incorporates correlation energies between surface groups due to electrostatic interactions and hydrogen bonding in the hydrated interfacial layer.

6.3. Impact of Chemical Structure of SG

In the following we will present and discuss detailed results obtained for the system with interfacial group CH_3SO_3H-H_2O (R_2). The system with the shortest fluorocarbon tail, CF_3SO_3H-H_2O (R_1), will serve as a reference for comparison, but results for this system will not be shown explicitly.

For R_1, the most stable configuration was found at d_{CC}= 6.7Å with E_f^{uc} = -2.78 eV . For R_2, the most stable configuration is found at d_{CC} = 6.2 Å with $E_f^{uc}\left(d_{CC}\right) = -2.27$ eV , as can be seen in Figure 6.1. For R_2, the absolute value of the formation energy, $|E_f^{uc}(d_{cc})|$, at the position of the minimum is thus lower by a value of 0.51 eV than that for R_1 ; the CF_3 group present in the tail possesses a stronger electron-withdrawing capacity than CH_3.The most stable conformation in both cases corresponds to the fully dissociated state. In this state, all SG are oriented in an upright configuration at an angle of $\theta \approx 90^{\circ}$ relative to the basal plane. Due to the strong interaction between H_3O^+ and SO_3^- groups a highly ordered hydrogen-bonded network in 2D is formed. The hexagonal symmetry in this surface conformation gives a saturated number of interfacial hydrogen bonds, corresponding to 9 hydrogen bonds per unit cell.

Figure.6.2 shows the upright conformation for the R_2 system at d_{cc} = 6.2 Å. The average hydrogen bond length is $d_{O\text{-}O}$ = 2.5 Å. The average OH bond length in H_3O^+ ions is 1.04 Å which is slightly larger than OH bond lengths in water ($d_{O\text{-}H}$=0.98 Å) and in CF_3-SO_3H-H_2O groups ($d_{O\text{-}H}$ = 1.02 Å).

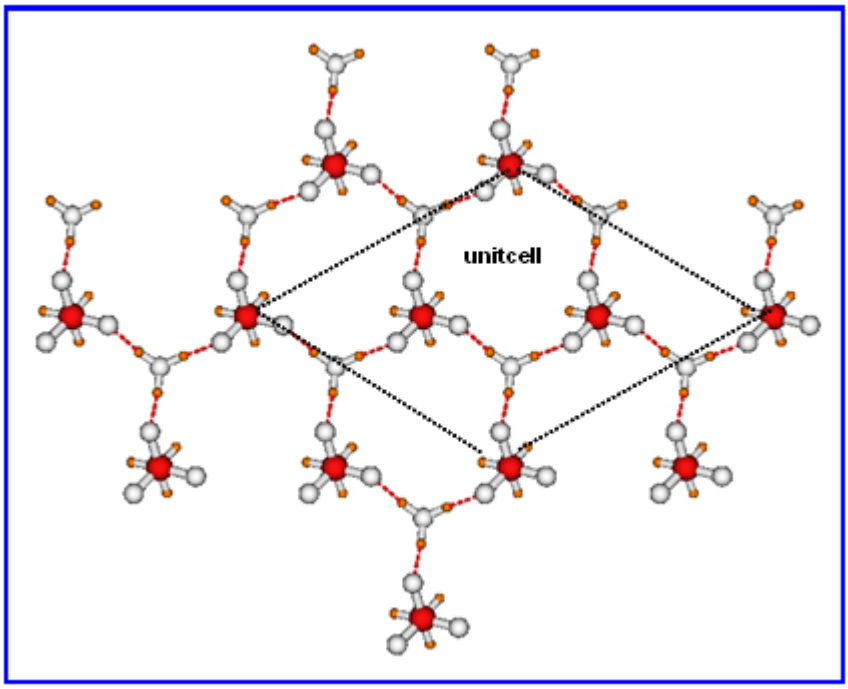

Figure 6.2: Top view of upright fully dissociated system $CH_3SO_3^-\cdots H_3O^+$ at d_{CC} = 6.2 Å.

For the R_2 system, we found that the average vertical separation between H_3O^+ ions (position of O atom) and the layer of SO_3^- groups (position of S atom) is ≈0.1 Å, which is ~0.9 Å smaller than the value found for the $CF_3SO_3H\cdots H_2O$ system. At the same d_{CC}, H_3O^+ ions are, thus, more deeply embedded into the interfacial layer for the $CH_3SO_3H\cdots H_2O$ system, indicating that interactions between H_3O^+ ions and the hydrophobic parts of the sidechains are significantly less repulsive for the SGs with hydrocarbon tails. Upon increasing d_{CC}, the fully dissociated "upright" structure becomes less stable. The average hydrogen bond length increases from $d_{O\text{-}O}$ = 2.5 Å to $d_{O\text{-}O}$ = 2.7 Å at d_{CC} = 7.1 Å corresponding to decreasing strength of hydrogen bonds and therefore lower absolute values of the formation energy which is E_f^{uc}=-1.17 eV at d_{CC}=7.1 Å. In comparison, for the R_1 system ($CF_3SO_3H\cdots H_2O$) the formation energy is E_f^{uc}=-1.67 eV at d_{CC}=7.1 Å. Figure 6.1 reveals the transition from upright fully dissociated to fully non-dissociated states in the upright conformation, indicated as point

a. The number of hydrogen bonds decreases from 9 to 3 upon this transition that occurs at d_{CC} = 7.4 Å for 3 x [CH_3SO_3H-H_2O] (as shown in Figure 6.3) and at d_{CC} = 7.1 Å for 3 x [CF_3SO_3H-H_2O].

For the array of 3 x [CH_3SO_3H-H_2O], the "upright" conformation becomes unstable at d_{CC} = 6.2 Å indicated as point b in Figure 6.1. For d_{CC} > 6.2 Å, a transition to a more stable fully dissociated "tilted" structure occurs. In the "titled" conformation, the three surface groups in each unit cell are inclined toward each other. The surface groups are rotated around their C-S axis and a hydronium ion, H_3O^+, is shifted laterally. As shown in Figure 6.4, upon increasing d_{CC} the tilting angle in the "tilted" state decreases monotonically from $\theta = 70^\circ$ for d_{CC} = 6 Å to $\theta = 10^\circ$ for d_{CC} > 9.5 Å compared to R_1 where θ decreases from 75° to 14° when d_{CC} increased from 6 Å to > 10 Å. At d_{CC} = 7.4 Å the number of hydrogen bonds per unit cell decreases from 9 to 7 as shown in Figure 6.3. The tilting of SG increases the number of interfacial hydrogen bonds at larger d_{CC}.

At the critical d_{CC} value marking the transition from "upright" to "tilted" state, inter-unit-cell hydrogen bonds are broken leading to the formation of disconnected clusters that consist of three surface groups and three H_3O^+ ions. Optimized geometries of fully dissociated "tilted" conformations with nine (at d_{CC} = 7.1 Å) and seven hydrogen bonds (at d_{CC} = 7.8 Å) are shown in Figure 6.5 and in Figure 6.6 respectively. The strong intracluster correlations due to shorter hydrogen bonds stabilize the "tilted" structure over the "upright" structure for d_{CC} > 7 Å.

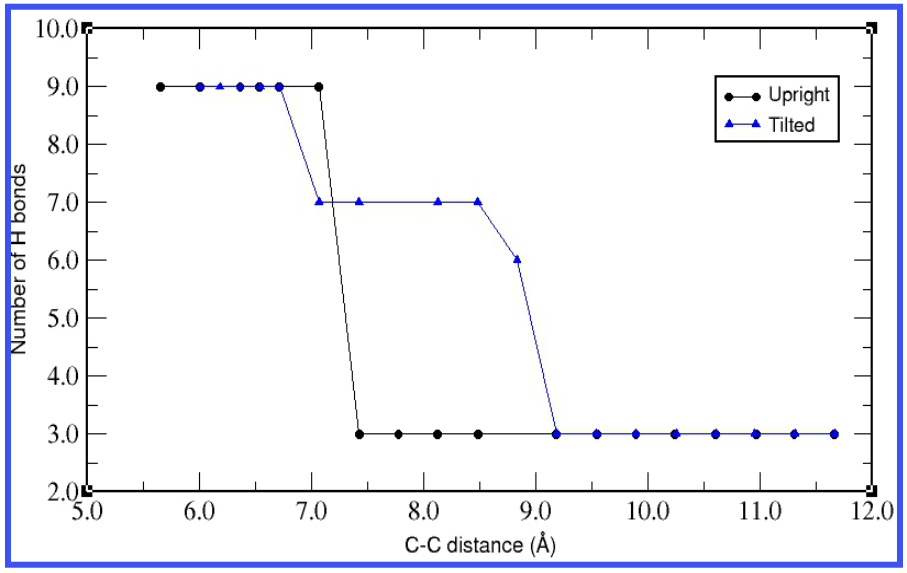

Figure 6.3: Number of hydrogen bonds in the R_2 system as a function of d_{CC} for "upright" and "tilted" structures.

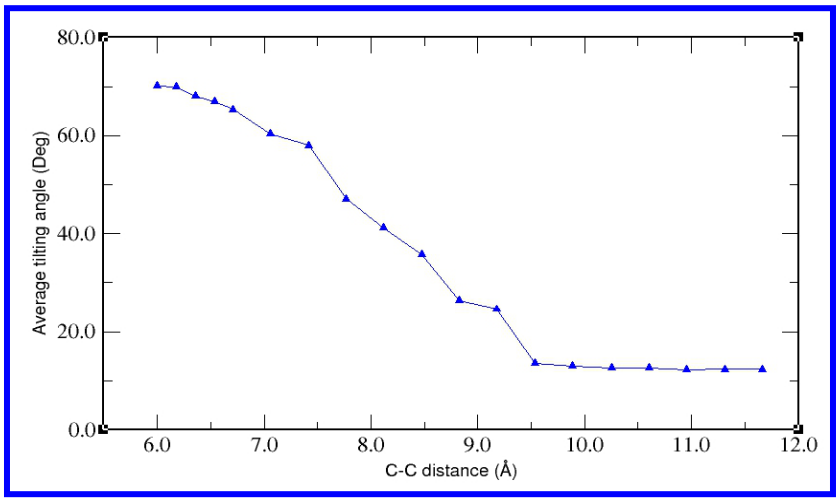

Figure 6.4: Average tilting angle in the R_2 system as a function of d_{CC} for tilted structures.

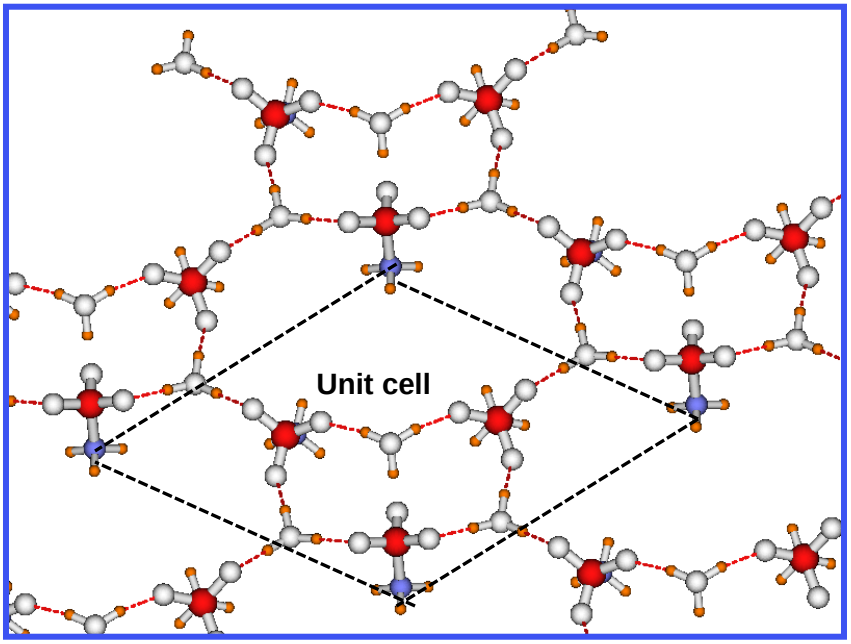

Figure 6.5: Optimized geometry of R_2 system in fully dissociated "tilted" structure at d_{CC} = 7.1 Å.

The transition from the fully dissociated "tilted" structure to the partially dissociated "tilted" structure with $2H_2O$ and $1H_3O^+$ as well as 7 hydrogen bonds remaining per unit cell occurs at d_{CC}= 7.8 Å for the R_2 system indicated as point c in Figure 6.1 also shown in Figure 6.6. For the R_1 system, this transition occurred only at d_{CC}=8.7 Å, owing to stronger interactions between sulfonic acid groups and hydronium ions.

The transition from a partially dissociated "tilted" structure to a fully non-dissociated structure occurs at d_{CC}=9.2 Å for the R_2 system, indicated as point d in Figure. 6.1, and at d_{CC}=9.2 Å for the R_1 system. Figure 6.7 shows the optimized fully non-dissociated "tilted" structure at d_{CC}= 10.3 Å. Upon further increasing d_{CC}, each SG has only one hydrogen bond with the closest water molecule. The intracluster hydrogen bonds are broken and the formation energy approaches zero. It is known from earlier simulations studies by Paddison *et al* [182, 288] that one water molecule is insufficient for the dissociation of sulfonic acid groups. The number of hydrogen bonds per unit cell is a measure of correlations in the interfacial layer which determines the structure at the interface. Strong long-range correlations exist at d_{CC} < 7 Å. Here, the hydronium ion

could attain its optimum number of hydrogen bonds. Short-range correlations persist at intermediate separations 7 Å < d_{CC} <10.5 Å. At d_{CC} ≥ 10.5 Å the correlation energy approaches zero due to the separation into three independent surface groups. In [262], the strength of binding of a single additional water molecule, E_b to the minimally hydrated acidic interface was evaluated for the R_1 system (3x [CF_3SO_3H-H_2O]). Moreover, the

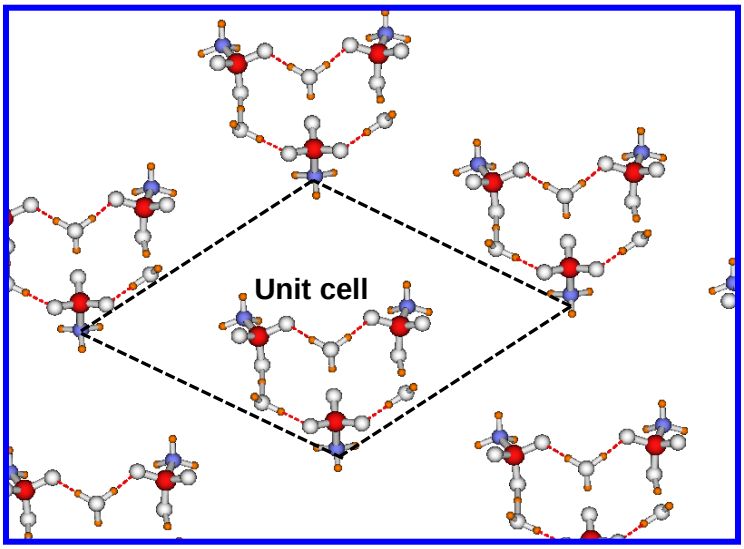

Figure 6.6: Top view of optimized tilted geometry of R_2 system at d_{CC}=7.8 Å with intracluster hydrogen bonds.

stability with respect to the removal of a water molecule, E_d, was explored. For the "upright" structure the additional water was weakly bound to two neighboring SO_3^- groups in the surface group separation range of 6.7 Å < d_{CC} < 9.9 Å. A Zundel cation, $H_5O_2^+$ formed by interaction of one H_3O^+ of the interfacial array with the additional water molecule was found in the tilted structure. In the strongly correlated regime for d_{CC} < 7.0 Å the absolute value of the binding energy of the additional water molecule was found as $|E_b|$ < 0.1 eV, indicating the hydrophobic nature of the minimally hydrated interfacial array due to the saturation of the number of strong hydrogen bonds. On the other hand the absolute value of $|E_b|$ > 0.8 eV for d_{CC} > 7.4 Å indicates the hydrophilic nature of the interface at sufficiently low SG density.

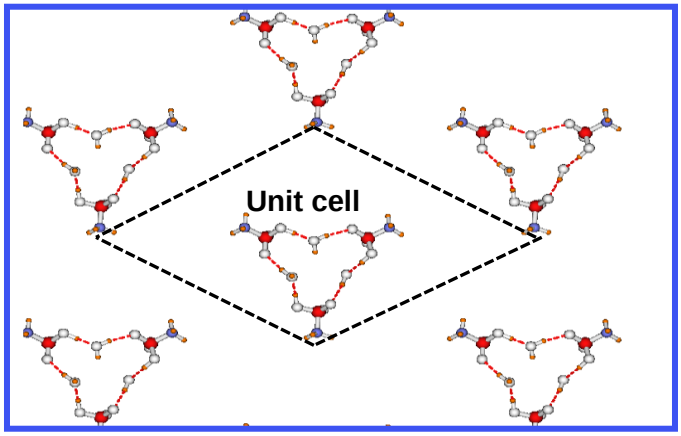

Figure 6.7: Optimized geometry of the R_2 system in the non-dissociated tilted state at d_{CC} = 10.3 Å.

6.4. Variation in the Length of Surface Groups

In Ref. [263], we focused on the effect of the chemical structure of sidechains on interfacial correlations and acid dissociation. Using the same simplified model system, optimization studies were carried out on systems including sidechain with increasing length. The comparison of the system 3 x [CH_3SO_3H-H_2O] with the system 3 x [CF_3SO_3H-H_2O], presented in the previous section, revealed that the replacement of the fluorocarbon group with a more hydrophilic hydrocarbon group has only a minor effect on the basic interfacial transitions.

In further studies [264], we have explored systems of the type 3 x [R_i-SO_3H], where R_3=$CF_3CF_2SO_3H$, R_4=$CF_3CF_2CF_2SO_3H$, and R_5 = $CF_3OCF_2CF_2SO_3H$. The last sidechain considered resembles the short sidechains in Dow® or Aquivion® ionomers (SSC membrane).

The separation of terminating C atoms SGs on the basal plane varied again in the range of 5.0 Å < d_{CC} < 20.0 Å [41, 56, 57]. In Figures 6.8, 6.9 and 6.10 and 6.11 we show the formation energy, E_f^{uc} per unit cell as a function of d_{CC} for arrays of R_1, R_3, R_4, and R_5. We have also compared the system R_1 for convenience and to get insight about complete dissociation and 2D correlation effect upon increasing length of the side chains or tail groups.

Plots of E_f^{uc} vs. d_{CC} look qualitatively similar to the shortest SGs, i.e. arrays with CH_3SO_3H/CF_3SO_3H. Thus, the basic interfacial conformations and correlations are independent of the chemical architecture of polymeric sidechains. Stated differently, the main structural effects at hydrated interfacial arrays are due to the structure of the acid head group and the packing density of SGs.

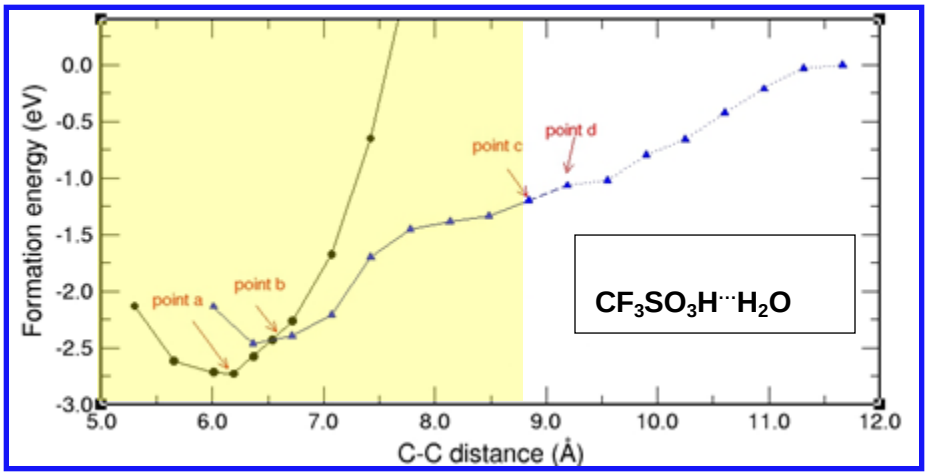

Figure 6.8: Formation energy per unit cell, E_f^{uc} as a function of C-C distance d_{CC} for arrays with R_1- SO_3H; (R_1=CF_3).

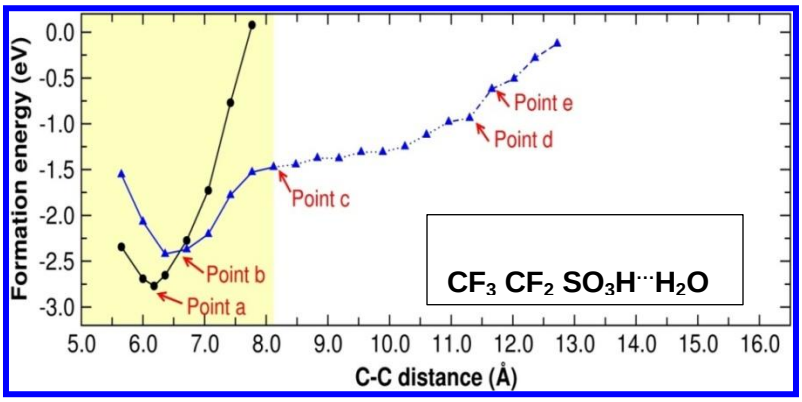

Figure 6.9: Formation energy per unit cell, E_f^{uc} as a function of C-C distance d_{CC} for arrays with R_3- SO_3H; (R_3= CF_3 CF_2).

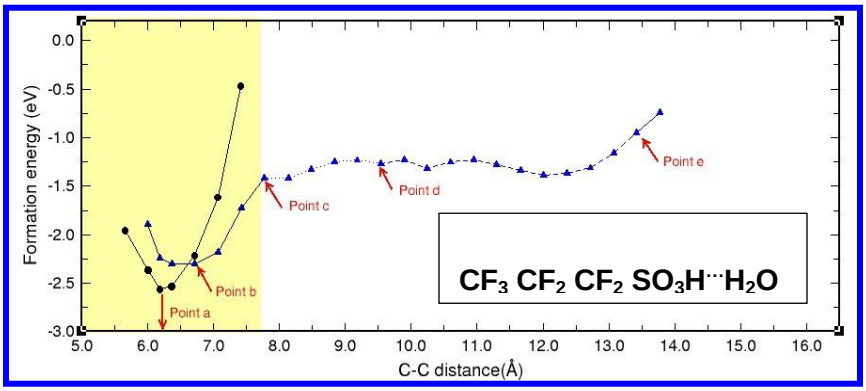

Figure 6.10: Formation energy per unit cell, E_f^{uc} as a function of C-C distance d_{CC} for arrays with R_4- SO_3H; (R_4= $CF_3CF_2CF_2$)

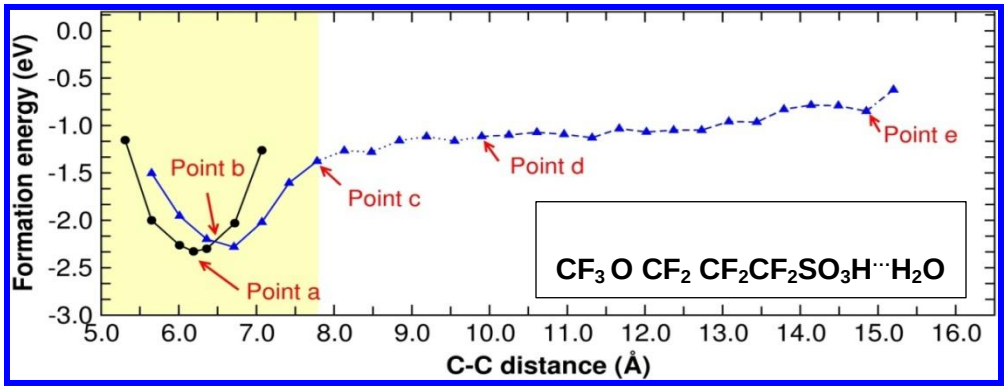

Figure 6.11: Formation energy per unit cell, E_f^{uc} as a function of C-C distance, d_{CC} for arrays with R_5- SO_3H; (R_5=$CF_3OCF_2CF_2CF_2$). The black curves (circles) correspond to the "upright" conformations and the blue curves (triangles) to the "tilted" conformations are provided in order to compare visually. The range of complete dissociation is highlighted. Reproduced with permission from A. Roudgar, S. P. Narasimachary and M. Eikerling, *J.Phys. Chem. B* 2006, 110, 20469 for Figure 6.8.; For the figures 6.9 through 6.11: Reproduced with permission from S. P. Narasimachary, A. Roudgar, and M. Eikerling, *Electrochim. Acta,* 2008, 53, 6920. Elsevier. Copyright 2008.

The most stable structure for all SGs is found at d_{CC}^{a}=6.2 Å . At this separation, the array is in the fully dissociated state $\left(\text{-}SO_3^-\right)$ with all acid protons residing on the hydronium ions (H_3O^+). In this "upright" conformation, the plane spanned by the three oxygen atoms in each SG is parallel to the basal plane. The resulting structure is a

highly ordered hydrogen-bonded network of $-SO_3^-$ and H_3O^+ moieties with long-range correlations, as can be seen in Figure. 6.11.

Trifluoromethane sulfonic acid CF_3SO_3H is a super acid. After deprotonation, the excess negative charge on the resulting conjugate base is stabilized by the electron-withdrawing effect of $-CF_3$. The stronger electron-withdrawing effect of $-CF_3$ compared to $-CH_3$ results in the more negative formation energy of the CF_3SO_3H array compared to the CH_3SO_3H, as discussed in § 6.2. $E_f^{uc}(\text{eV})\ \Delta q_0(e_0)\ d_{CC}^a(\text{Å})$

Table 6.1. Formation energies, $E_f^{uc}(\text{eV})$, and average excess charges per oxygen species of sulfonic acid head groups, Δq_0 (in the units of elementary charges, e_0) for various systems considered in this study. Reproduced with permission from S. P. Narasimachary, A. Roudgar, and M. Eikerling, *Electrochim. Acta,* 2008, 53, 6920. Elsevier. Copyright 2008.

R_I-SO_3H	E_f^{uc}(eV)	Δq_0(eV)	d_{CC}^a(Å)	d_{CC}^b(Å)	d_{CC}^c(Å)	d_{CC}^dÅ)	d_{CC}^e(Å)
R_1	-2.78	-0.2627	6.2	6.7	8.7	9.2	-
R_2	-2.25	-0.1812	6.2	6.7	7.4	9.2	-
R_3	-2.77	-0.2415	6.2	6.7	8.1	11.3	11.6
R_4	-2.56	-0.2040	6.2	6.7	7.7	9.8	13.8
R_5	-2.46	-0.1903	6.2	6.7	7.7	9.8	15.5

The trend in the formation energies, E_f^{uc}, in Table 6.1 upon increasing the length of sidechains can be explained based on the poor stabilization of excess negative charge on the sulfonic acid group upon deprotonation due to the influence of hydrophobic parts of the SGs. It can be seen that, in going from the shortest to the longest SGs, the formation energy increases from $E_f^{uc}\left[CF_3SO_3H\right]_{d_{CC}^a} = -2.78$ eV to $E_f^{uc}\left[CF_3OCF_2CF_2SO_3H\right]_{d_{CC}^a} = -2.46$ eV, indicating that the interfacial array is less stable for longer SGs.

In order to quantify this assumption, we have calculated the average localized charge per oxygen atom of $-SO_3^-$ groups by $q_O^{ave} = \int_{V_s} \rho(\vec{r})\, d^3r$, where $\rho(\vec{r})$ is the average charge density at point $(\vec{r})$. Integration is performed over the volume V_s that encloses a region with localized space charge around each oxygen atom. This region is defined by the existence of a strong electrostatic potential exerted by the charged oxygen, $|U_{el}(r)| > |U_{cut}|$. In our calculation, we have approximated the integral by $\sum_k \rho_k(\Delta V)$ where $\Delta V = 2.42X10^{-4}$ Å^3 and index k includes a number of points in V_s. The cut-off value of the electrostatic potential $|U_{cut}|$ has to be set initially. For a too large value of $|U_{cut}|$ we could cut off a portion of the localized charge. Choosing $|U_{cut}|$ too small would mean that we would account for non-localized charge. In order to determine the most appropriate value of U_{cut}, we have generated contour plots of isolines of the electrostatic potential in the plane spanned by the three oxygen atoms in the unit cell. $|U_{cut}|$ corresponds to the smallest absolute value of the electrostatic potential, at which the isolines around neighboring oxygen atoms do not overlap. Based on this procedure, we found $U_{cut} = -30$ eV. The values of q_O^{ave} calculated using this U_{cut} are listed in Table 6.1. We found that q_O^{ave} is reduced with increasing length of the surface groups. The reduction in localized charge destabilizes the ordered interfacial array of SGs. Upon increasing d_{CC}, the formation energy is reduced and the "upright" conformation structure is destabilized. The transition from fully dissociated "upright" conformation to a clustered conformation occurs at $d_{CC} = d_{CC}^b$. In this "tilted" conformation, the planes spanned by three oxygen atoms of the $-SO_3^-$ head groups are no longer parallel to the basal plane; their normal vectors are inclined towards each other. On-top views of optimized geometries in this conformation are shown at d_{CC}^b in Figure.6.12 for $CF_3CF_2SO_3H$, $CF_3CF_3CF_2SO_3H$ and $CF_3OCF_3CF_2SO_3H$, respectively. At high densities of surface groups in the "tilted" conformation, i.e. for $d_{CC}^b \leq d_{CC} < d_{CC}^c$, the SGs remain in the fully dissociated state.

The widths of different regions of stability and degree of dissociation for all SGs are given in Table 6.1. The wide range of full dissociation is a result of correlation effects in 2D. Deprotonation of acid-functionalized polymeric sidechains with only one water molecule added per acid head group has not been observed in calculations that considered only a single sidechain or a polymeric fragment with several neighbouring sidechains along a single backbone strand [31, 32].

In Figure 6.14, the number of hydrogen bonds per unit cell is shown as a function of d_{CC}. We have defined a hydrogen bond by having separations in the range of $2.5 < d_{O\text{-}O} < 2.9$ Å between the two hydrogen-bonded oxygen atoms [76,157,160,290]. In the fully dissociated "upright" conformation, the number of hydrogen bonds per unit cell is nine corresponding to the maximum possible value. Saturation of the number of hydrogen bonds in this conformation is enabled by the trigonal symmetry of the interfacial structure. Clustering in the "tilted" conformation allows maintaining the largest number of strong hydrogen bonds possible in the range $d_{CC}^{b} \le d_{CC} < d_{CC}^{c}$, viz. nine hydrogen bonds per unit cell. The average hydrogen-bond length at the transition point is d_{OO}^{b}=2.57 Å .

In the range $d_{CC}^{c} \le d_{CC} < d_{CC}^{d}$, two inter-unit cell hydrogen bonds are broken. The remaining seven hydrogen bonds per unit cell have an average length of $d_{OO}^{c\text{-}d}$=2.53 Å . In this range the formation energy is more positive by $\Delta E_f^{uc} \approx 1.0$ eV relative to the most stable conformation at d_{CC}^{a}. In the partially dissociated state for $d_{CC}^{c} \le d_{CC} < d_{CC}^{d}$, two SGs per unit cell are found in the dissociated state $\left(-SO_3^- \cdots H_3O^+\right)$, and one SG in the non-dissociated state $\left(-SO_3H \cdots H_2O\right)$. Corresponding optimized geometries at d_{CC}=8.1 Å are shown for arrays with SG of the type $CF_3CF_2SO_3H$, $CF_3CF_3CF_2SO_3H$, and $CF_3OCF_3CF_2SO_3H$ in Figure 6.13.

Detailed studies on the strength of binding an additional water molecule to the minimally hydrated interface revealed a rather interesting effect of interfacial correlations [263]. As stated in §6.2, as d_{CC} decreases, the strength of extra water binding changes

from $|E_b| > 0.8$ eV for $d_{CC} > 7.4$ Å to $|E_b| < 0.1$ eV for $d_{CC} < 7$ Å. This transition from hydrophilicity to hydrophobicity is related to the change in the number of hydrogen bonds from 7 to 9 in the narrow range of d_{CC}.

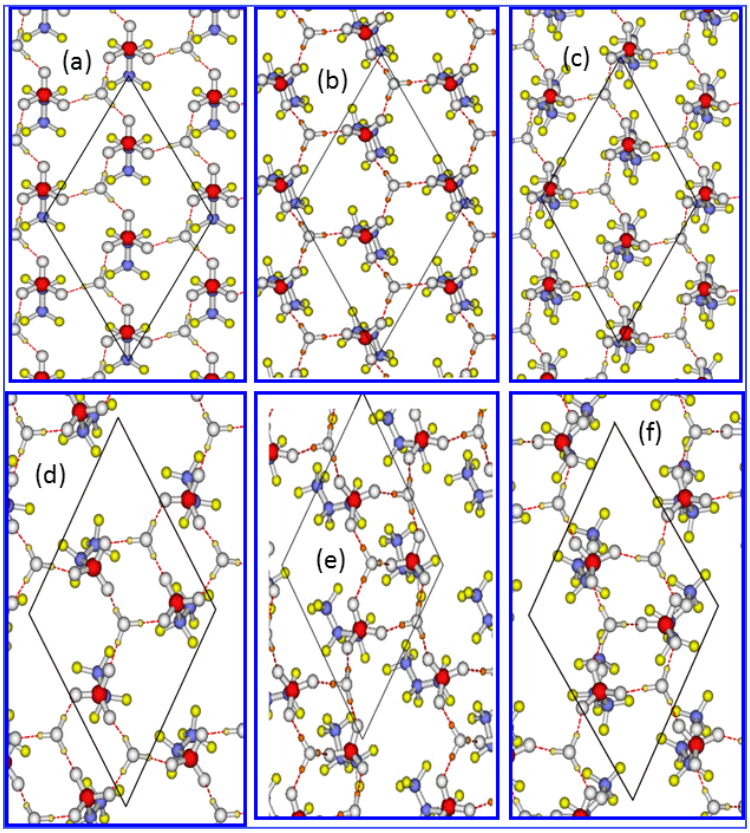

Figure 6.12: **On top views of arrays of SGs with (a) $CF_3CF_2SO_3H$, (b) $CF_3CF_2CF_2SO_3H$ and (c) $CF_3OCF_2CF_2SO_3H$ at d_{CC}^{b} for "upright" and (d), (e), (f) for tilted conformations respectively. Reproduced with permission from S. P. Narasimachary, A. Roudgar, and M. Eikerling, *Electrochim. Acta,* 2008, 53,6920. Elsevier. Copyright 2008.**

The hydrophobic nature of the interface at $d_{CC} < 7$ Å is due to the saturation of the number of hydrogen bonds in the highly ordered "upright" conformation. On the other hand, at $d_{CC} > 7.4$ Å undersaturation of the number of hydrogen bonds allows strong binding of additional water molecules. We expect to find similar hydrophilic-to-hydrophobic transition in systems with varying sidechain architecture. This transition might shift to slightly larger values of d_{CC} but still will fall within the range of 7 Å < d_{CC}< 8 Å, as suggested in Figure. 6.10 correlation with the transition in the number of hydrogen

bonds per unit cell. In the range $d_{CC}^{d} \le d_{CC} < d_{CC}^{e}$, one acid head group per unit cell is in the dissociated state $\left(-SO_3^- \cdots H_3O^+\right)$ and two are found in the non-dissociated state $\left(-SO_3^- \cdots H_3O^+\right)$. Optimized geometries for $CF_3CF_2SO_3H$, $CF_3CF_2CF_2SO_3H$, and $CF_3OCF_2CF_2SO_3H$ in this state are shown at d_{cc} =11.3 Å in Figure. 6.15. The average number of hydrogen bonds remains 7 per unit cell up to point (e) as given in Figure. 6.10. As the length of SGs increases, the range with partially dissociated head groups becomes wider. This implies that in the highly disordered and dynamic real membrane situation, it is probable to find a fraction of dissociated protons at all relevant separations of SGs under conditions of minimal hydration.

Upon further increasing d_{CC} beyond point (e), the clusters break up. Hence, the average number of hydrogen bonds per unit cell drops to 3 and the formation energy E_f^{uc} approaches zero corresponding to independent SGs with one water molecule each. In conclusion, a regular array of acid functionalized SGs was utilized for performing *ab initio* studies of structural correlations and processes in polymer electrolyte membranes at low hydration. This model system resembles the microscopic interfacial elements at polymeric hydrated fibrils in PEMs. We have evaluated the effects of “sidechain length” (chemical structure), packing density, and flexibility of acid-functionalized polymeric sidechains. The simplest surface groups correspond to trimethanesulfonic acid (trifilic acid) and the most complex surface groups considered mimic sidechains of Aquivion® membranes. For all systems, we have found similar trends in interfacial conformations, strength of interfacial correlations, acid dissociation, and hydrogen bonding. At high packing density, we found that the “upright” conformation to be the most stable state. In this conformation, acid head groups are completely dissociated corresponding to the formation of nine hydrogen bonds per unit cell.

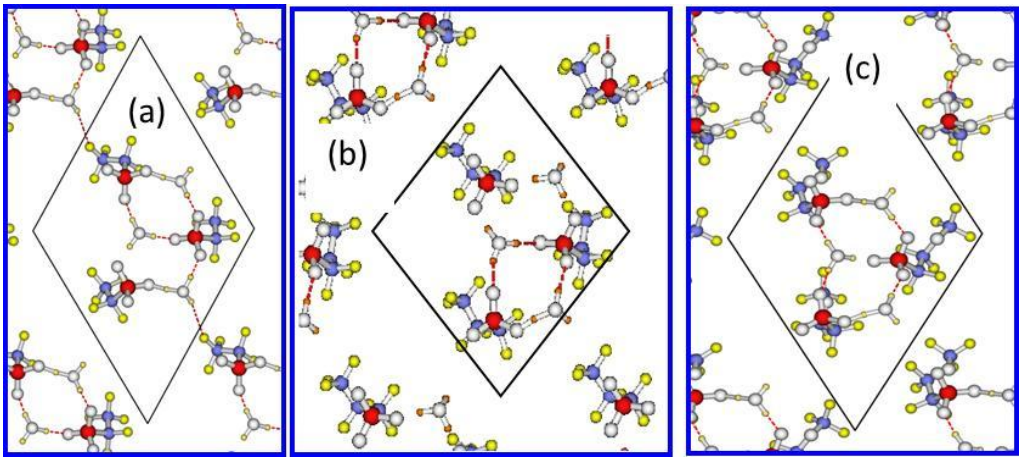

Figure 6.13: Depicting partially dissociated tilted configurations at d_{CC}=8.1 Å for (a) $CF_3CF_2SO_3H$, (b) $CF_3CF_2CF_2SO_3H$, and (c) $CF_3OCF_2CF_2SO_3H$. Reproduced with permission from S. P. Narasimachary, A. Roudgar, and M. Eikerling, *Electrochim. Acta,* 2008, 53, 6920. Copyright Elsevier 2008.

Decreasing the packing density of SGs triggered the transition from the “stiff” upright conformation to the “tilted” conformation with clustering of surface groups. As the sidechain length increases, the formation energies at the most stable conformation decreased. The sidechain length has a significant impact on the range of interfacial correlations. Upon increasing the “lengths” of sidechains, strong correlations, assisted by the persistence of strong hydrogen bonds and of dissociated acid protons, extend to separations between surface groups of up to 15 Å. In general, this study highlights the importance of 2D correlation effects at polymer-water interfaces in PEMs.

.

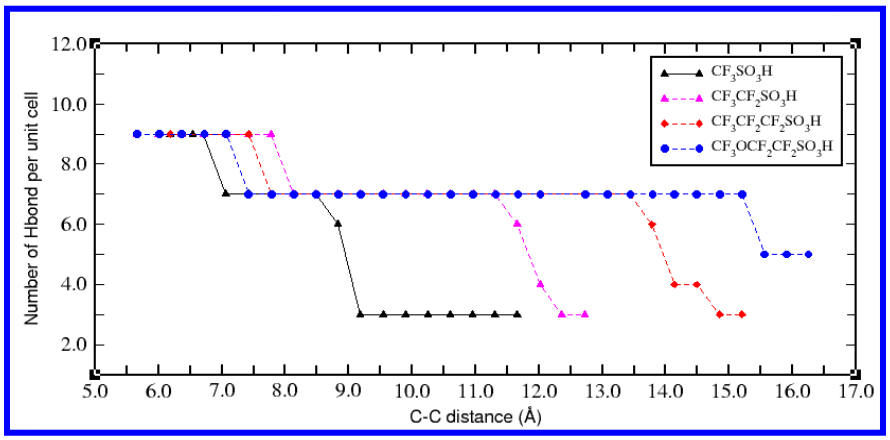

Figure 6.14: Number of hydrogen bonds per unit cell as a function of d_{CC} for R_i-SO_3H. Reproduced with permission from S. P. Narasimachary, A. Roudgar, and M. Eikerling, *Electrochim. Acta,* 2008, 53, 6920. Copyright Elsevier 2008.

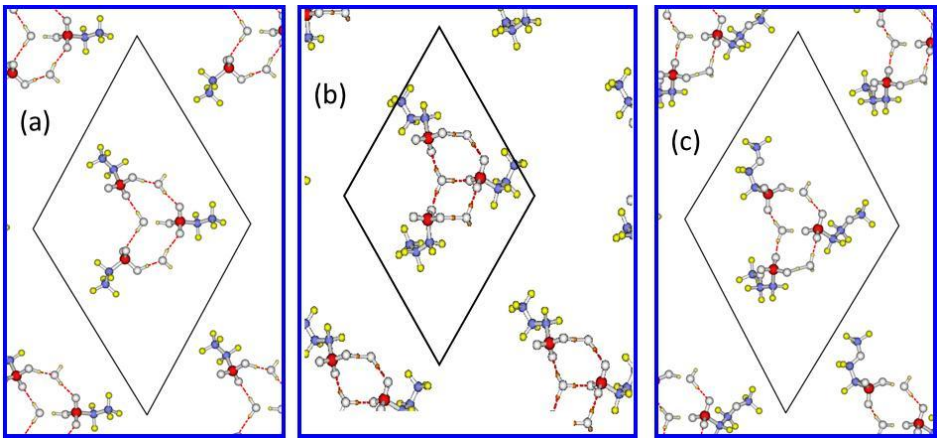

Figure 6.15: Optimized "tilted" structure of (a) $CF_3CF_2SO_3H$ (b) $CF_3CF_2CF_2SO_3H$ and (c) $CF_3OCF_2CF_2SO_3H$ at d_{CC}=11.3Å. Reproduced with permission. from S. P. Narasimachary, A. Roudgar, and M. Eikerling, *Electrochim. Acta,* 2008, 53, 6920. Copyright Elsevier 2008.

6.5. Ab initio Study of Surface-Mediated Proton Transport

In ref [263,264], we explored how the orientational fluctuations of surface groups facilitate the structural transitions between energetically degenerate conformations at the critical separation, d_{CC} = 6.7 Å. This transition involves proton transfer between unit cells.

In order to overcome the difficulties of simulating a large number of particles in *ab initio* method, we reduced the high dimensional coordinate space of all atom system to a low dimensional space of collective coordinates (CC). We identify three CCs from our calculation, viz. the lateral shift, r, of H_3O^+ ion transferring parallel to the basal plane, specified relative to the position of fixed carbon atom in the accepting surface group, (SG1), the azimuthal angle, θ, of tilting of SG (1) relative to the basal plane; and the polar angle of rotation, ϕ, of the head sulfonic acid group of SG (1). We utilized these three CCs in order to evaluate complex potential energy surface (PES), identify the saddle points and evaluate the transition path we determined the activation energy for this transition at d_{CC}= 6.7 Å and compared it with results from d_{CC} = 6.3 Å and d_{CC} = 7.1 Å. We explored the PES by generating grid points of size 10x10x10 in space spanned by r, θ and ϕ.

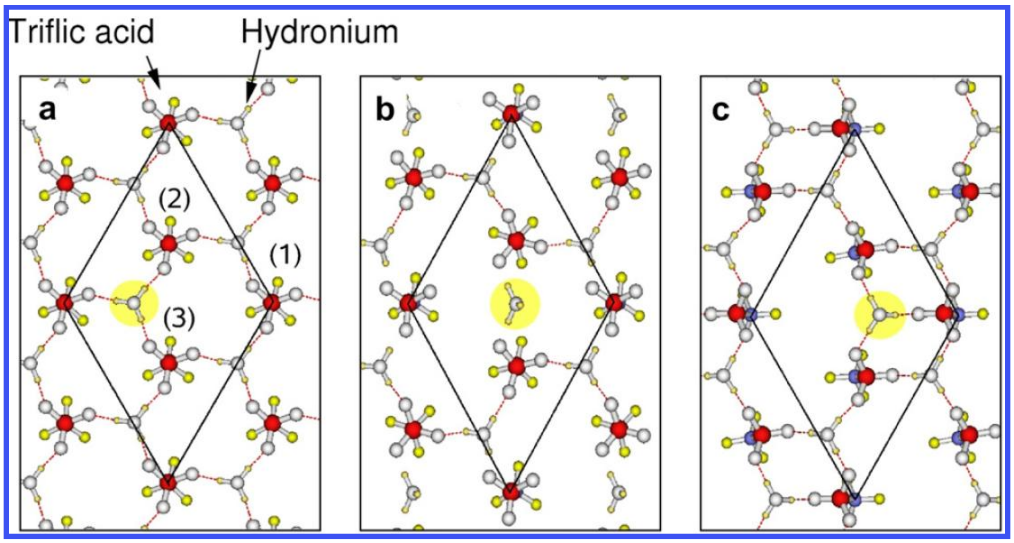

Figure 6.16: Interfacial conformations during structural transition from upright (a) to tilted conformation (c) is shown and the unit cell with three surface groups are labeled in a. Reproduced with permission from *Ab initio* study of surface-mediated proton transfer in polymer electrolyte membranes, A. Roudgar, S. P. Narasimachary and M. Eikerling, *J. Chem. Phys. Letts*. 2008, 457, 337. Copyright Elsevier 2008.

The position of the hydronium ion was changed from r = 7.77 to r = 4.43. SG (1) which is the acceptor side of the hydrogen bond exhibits rotation $\Delta\phi = 37.4^{\circ}$ and tilting $\Delta\theta = 23.5^{\circ}$ due to the tilting and rotation of SG (1). For the SG (2) and SG (3) groups, the variation was found to be much lower. We chose intervals between grid points (r, θ, ϕ) to be $\delta r = 0.4$ Å, $\delta\theta = 2.6^{\circ}$ and $\delta\phi = 4.2^{\circ}$. We performed geometry optimization at each grid points with complete relaxation of all degrees of freedom. We define configuration energy at the grid point as,

$$E_{conf} = E_{total} - E_{total}^{upright}, \qquad \textbf{6.3}$$

where $E_{total}^{upright}$ is the reference value of the total energy in the stable 'upright' conformation at d_{CC}. A plot of E_{conf} along the lowest energy reaction path for d_{CC} = 6.7 Å is shown along with the same path at d_{CC} = 6.3 Å and d_{CC} = 7.1 Å. Conformations a to c in Figure 6.16 is clearly shown in the plot of Figure 6.17, where we can see the hydrogen bond breaking between mobile hydronium ion with SG, rotation of H_3O^+ over its back and reformation of a new H bond with the next SG. We also calculated the barrier

energy along the minimum energy path from upright to tilted conformation and found a value of ΔE =0.64 eV, 0.55 eV, and 0.28 eV corresponding to d_{CC} = 6.3, 6.7, and 7.1 Å. For the transfer in the reverse direction which is from 'tilted' to 'upright', the barrier energy, ΔE = 0.38 eV, 0.58 eV and 0.68 eV respectively. The plot further implies that, above d_{CC} > 6.7 Å, the tilted structure is favoured over the upright structure,with an energy difference of 0.03 eV at d_{CC} = 6.7 Å and 0.4 eV at d_{CC} = 7.1 Å.

This study demonstrates that, rotation and tilting play a vital role in H-bond breaking / reforming at the SGs.

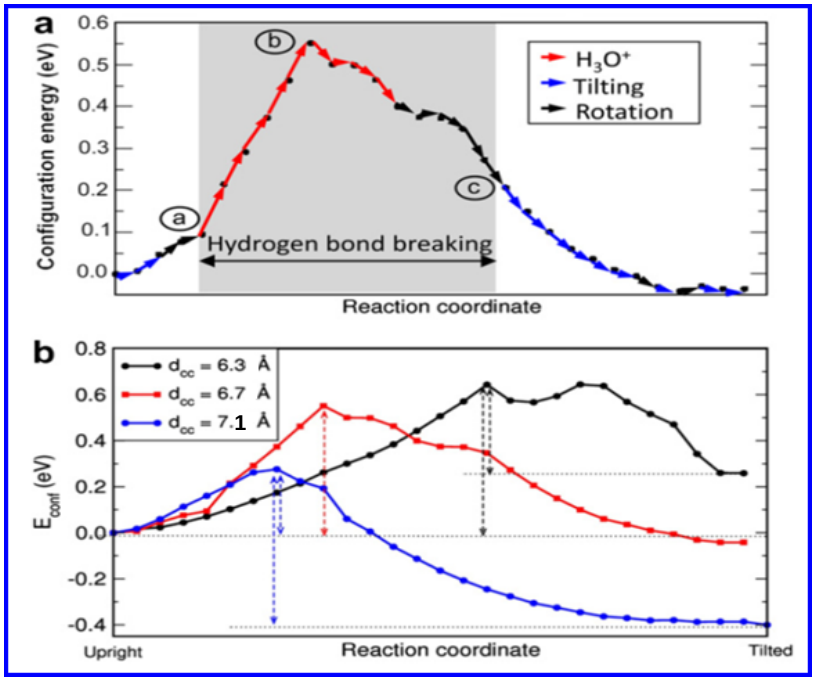

Figure 6.17: (a) Configuration energy along the minimum energy path for the transition between upright to tilted conformations at d_{CC} = 6.7 Å is shown with points a, b, c corresponds to the conformations in Figure 6.16. Contribution of the collective coordinates to the reaction path is also indicated. (b) Comparison of the minimum energy paths for transition at d_{CC} = 6.3, d_{CC} = 6.7, and d_{CC}= 7.1 Å is depicted. Reproduced with permission from A. Roudgar, S. P. Narasimachary and M. Eikerling, *J. Chem. Phys. Letts*. 2008, 457, 337. Copyright Elsevier 2008.

We predict that fluctuations in classical degrees of freedom could thus trigger proton transport at the interface with transition probability given as:

$$\kappa_{PT} \sim \nu_{eff} \exp\left(-\frac{G^a}{k_B T}\right). \qquad \textbf{6.4}$$

With an effective frequency ν_{eff} of classical nuclear modes, corresponding to fluctuations in ϕ and θ, and the activation Gibbs free energy of the transition, G^a, needed to reach the saddle point along the reaction hypersurface. The barrier energy, ΔE, determined above, provides an upper estimate of G^a. A full energy calculation, leaving all molecular degrees of freedom unconstrained, increasing the size of the unit cell, adding more water molecules, correcting for zero point energy, and accounting for dispersion interactions and image charge effects at the interface would result in a significantly lower value of G^a. The identified minimum energy path on the PES will be valuable for initializing dynamic simulations employing Transition Path Sampling [257], Umberalla Sampling [259], or Metadynamics method [295] for a more accurate determination of G^a .The fluctuation modes of the CC are determined by non-bonded interactions between SG(1) and remaining degrees of freedom of the interfacial array. We estimate the frequencies of these low-frequency modes by fitting Morse potentials [296]

$$E_M = D_e\left\{1-\exp\left[a(x-x_e)\right]\right\}, x \in \{\phi,\theta\}, \qquad \textbf{6.5}$$

to E_{conf} for small fluctuations of ϕ,θ where x_e represents stable positions of these variables in 'upright' or 'tilted' conformations. We determine the fit parameters D_e and a, we calculated the Morse frequencies $\nu_M = \nu_{har}(1-2\chi_e)$ with harmonic frequency $\nu_{har} = \frac{a}{\pi}\sqrt{\frac{D_e}{2I}}$,anharmonicity factor $\chi_e = \frac{h\nu_{har}}{4D_e}$, and moment of inertia [296]. We performed these calculations for two extreme cases of coupling between SG (1) and the remaining system, i.e. for weak and strong coupling limits. In the weak coupling limit, optimization of the electronic wavefunction was performed by varying ϕ and θ for stiff ionic configuration of SG (1) and frozen positions of all other ionic cores. SG (1) rotates and tilts relative to its anchoring point on the basal plane. Effective moment of inertia for tilting and rotating of SG (1) are given by

$$I_{\phi}^{wc} = \sum_{i=1}^{n_{\phi}} m_i \left(\vec{r}_i - \vec{r}_S\right)^2, \qquad \textbf{6.6}$$

$$I_{\theta}^{wc} = \sum_{i=1}^{n_{\theta}} m_i \left(\vec{r}_i - \vec{r}_C\right)^2, \qquad \textbf{6.7}$$

where $n_{\phi} = 3$ accounts for the O atoms in the SO_3^- head group, whereas $n_{\theta} = 4$ includes both the O and S atoms in SG (1). m_i is the mass of the i-th atom and $(\vec{r}_i - \vec{r}_S)$ and $(\vec{r}_i - \vec{r}_C)$ are the positions of the i-th atom relative to S and C atoms. We obtain in the weak coupling limit, $\nu_{\phi}^{WC} = 153$ cm^{-1} and $\nu_{\theta}^{WC} = 106$ cm^{-1} for 'upright' and $\nu_{\phi}^{WC} = 169$ cm^{-1} and $\nu_{\theta}^{WC} = 108$ cm^{-1} for 'tilted' conformations.

In the strong coupling limit, corresponding to the contour plots E_{conf}^{SC} is obtained by varying ϕ and θ in the vicinity of stable conformations, while all other degrees of freedom are allowed to relax. Effective moments of intertia are calculated by incorporating all atoms in the unit cell, except those which are fixed, i.e. I_{ϕ}^{SC} includes sum over all O, H, S atoms relative to the S atom in the SG(1) and I_{θ}^{SC} includes sum over all S, O, H atoms in the unit cell relative to the C atom in SG(1). Effective moments of inertia in the strong coupling limit are $I_{\phi}^{SC} \simeq 21 I_{\phi}^{WC}$ and $I_{\theta}^{SC} \simeq 80 I_{\theta}^{WC}$. The frequency of normal modes, determined from fitting Morse potentials to E_{conf}^{SC} are $\nu_{\phi}^{SC} = 11$ cm^{-1}, $\nu_{\theta}^{SC} = 12$ cm^{-1} for "upright" and $\nu_{\phi}^{SC} = 8$ cm^{-1}, $\nu_{\theta}^{SC} = 15$ cm^{-1} for "tilted" conformations.

We utilized CPMD simulation in the NVT ensemble in order to analyse fully the interfacial mode spectrum. For this we did CPMD calculations for about 63 ps in total on the "upright" conformation with d_{CC} = 6.7 Å at 300 K. The first 2 ps considered for thermalization. The time interval from which uncorrelated initial configurations are sampled is 30 ps. The maximum remaining correlation time for the calculation of autocorrelation functions is 30 ps. The corresponding frequency resolution is 1 cm^{-1}. Most frequencies identified in the full spectrum could be assigned to normal modes of

trifilic acid in the gas phase [298] except for peaks at 56 cm^{-1}, 102 cm^{-1}, 123 cm^{-1}, which represent interfacial correlations.

We obtained the specific frequencies of rotation and tilting of SG(1) by projecting out the temporal evolution of the collective coordinates $\phi(t)$ and $\theta(t)$ from the complete NVT trajectory and subsequently Fourier-transforming the autocorrelation functions

$$V_{\phi\phi}(t) = \sum_{i=1}^{3} \left\langle \dot{\phi}_i(0) \mid \dot{\phi}_i(t) \right\rangle_T / \left\langle \dot{\phi}_i^2 \right\rangle_T \qquad \textbf{6.8}$$

and

$$V_{\theta\theta}(t) = \left\langle \dot{\theta}_i(0) \mid \dot{\theta}_i(t) \right\rangle_T / \left\langle \dot{\theta}_i^2 \right\rangle_T \qquad \textbf{6.9}$$

For the ϕ-spectrum we added up the contributions from rotations of all three SO_i bonds, with i=1, 2, 3. We depict the frequency spectra (Figure 6.18 and in 6.19) corresponding to $\phi(t)$ and $\theta(t)$. In order to more clearly identify the dominant low-frequency vibration modes of the interfacial array, we used a smoothing procedure by applying standard weighted averaging over an interval of 8 cm^{-1} centered around each point in the depicted spectra. After this processing, we could clearly discern low-frequency bands with peaks in the range of 50 – 130 cm^{-1}. The inset in Figure 6.18 resolves the ϕ-spectrum into rotations of the three individual SO_i bonds. The most pronounced peaks, observed at 56 cm^{-1} and 102 cm^{-1}, correspond to concerted motions of all three SO_i bonds. The most pronounced peak in the θ-spectrum, Figure 6.19 is found at 133 cm^{-1} with smaller peaks at 56 cm^{-1}, 76 cm^{-1}, 104 cm^{-1}, and 173 cm^{-1}. We have identified two concerted tilting-rotation peaks at $\nu_1^{MD} \cong 56\ cm^{-1}$ and $\nu_2^{MD} \cong 104\ cm^{-1}$. Averaging over longer simulation time and / or larger system size could cause some maxima to merge into broader 'bands', which would be more characteristic for the considered system. This would, however, not invalidate our conclusion on concerted tilting-rotation modes in the range of 50 cm^{-1} – 100 cm^{-1}. Low-frequency modes of reactive coordinate ϕ and θ depend strongly on hydrogen-bonding and electrostatic interactions in the interfacial network. We evaluate the strength of coupling between

fluctuations of SG (1) and the relaxation of the remaining system by comparing characteristic frequencies $\nu_{\phi/\theta}^{WC/SC}$ obtained from Morse fits with $\nu_{1/2}^{MD}$. For a quantitative comparison, we define effective moments of inertia by

$$I_{1/2}^{eff} = I_{\phi/\theta}^{WC}\left(\nu_{\phi/\theta}^{WC} / \nu_{1/2}^{MD}\right)^2 \qquad \textbf{6.10}$$

or

$$I_{1/2}^{eff} = I_{\phi/\theta}^{SC}\left(\nu_{\phi/\theta}^{SC} / \nu_{1/2}^{MD}\right)^2 . \qquad \textbf{6.11}$$

We find $I_{1/2}^{eff} / I_{\phi/\theta}^{WC} \simeq 2-4$ or $I_{1/2}^{eff} / I_{\phi/\theta}^{SC} \ll 1$. These results suggest that the dynamics of the system is more closely approximated by assuming weak coupling of tilting-rotation modes of SG (1) with the relaxation of the remaining interfacial array.

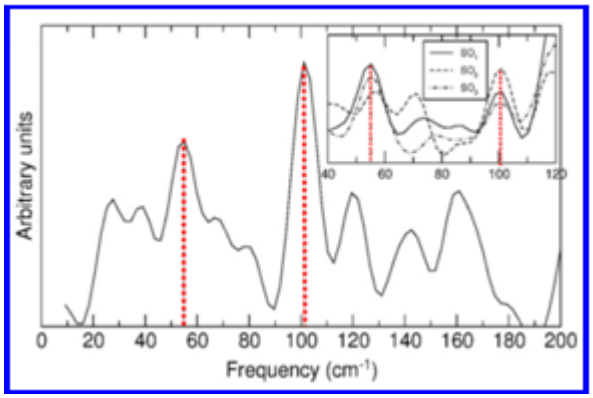

Figure 6.18: Low frequency bands of rotation of SG (1) The inset resolves the ϕ spectrum into individual rotations of three S-O bonds. Reproduced with permission from *Ab initio* study of surface-mediated proton transfer in polymer electrolyte membranes, A. Roudgar, S. P. Narasimachary and M. Eikerling, *J. Chem. Phys. Letts*. 2008, 457, 337. Copyright Elsevier 2008.

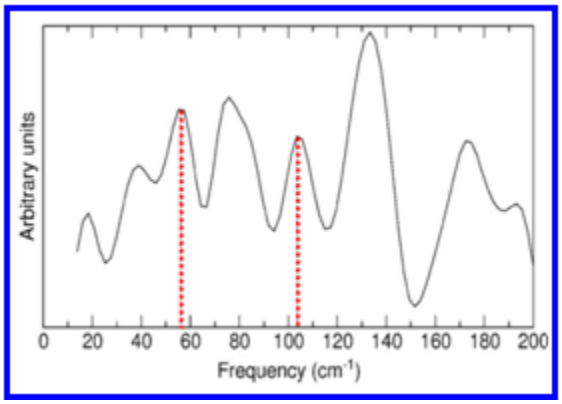

Figure 6.19: Low frequency bands of tilting of SG (1) at 6.72 Å. Reproduced with permission from *Ab initio* study of surface-mediated proton transfer in polymer electrolyte membranes, A. Roudgar, S. P. Narasimachary and M. Eikerling, *J. Chem. Phys. Letts*. 2008, 457, 337. Copyright Elsevier 2008.

Through detailed ab initio molecular dynamics simulation, we identified molecular mechanism of the elementary act of proton transport in minimally hydrated condition. The activation energy of proton transport found from this work, ~ 0.5 eV is found to be in reasonable range. We propose that, concerted tilting and rotation of surface group accepts / donates the transferring proton. Analysis of low frequency dynamics suggests that the orientational fluctuations of proton donating/accepting surface groups couple only weakly to the relaxation of the remaining interface.

6.6. Addition of Monolayer of Water to Minimally Hydrated Array

In this section, we consider increasing the level of hydration of the system. The question addressed in this study was: What will be the effect of adding a monolayer of water to the minimally hydrated interface? Details pertaining to the addition of a monolayer of water such as the change in interfacial conformation, binding energy of an additional water layer, and local water structure can be understood by optimization studies.

In order to form a monolayer of water molecules, the number of water molecules that should be added per unit cell should be estimated. This was roughly estimated using area of hexagonal unit cell and area of water molecule and using $d_{CC} \approx$ 7Å. The

area of the hexagonal unit cell is $A_{uc} = 3a^2\cos 60^\circ$, where a is the lattice constant. For a = 7 Å, the area of a unit cell =73.5 $Å^2$. A single water molecule occupies an area of 7 $Å^2$ [265-267]. The number of water molecules to create a monolayer above the unit cell is thus ~10. The $d_{CC} \approx$ 7Å is considered as a reference since it represents the transition from weak to strong binding of an additional water molecule [263].

The value of 10 water molecules in the extra water layer is only a lower bound. In order to obtain a more precise estimate of the number of water molecules required to form the extra water layer the following procedure was adopted. A slab of bulk water consisting of 64 water molecule was considered. A single water layer was cut from this slab and optimized. From the geometry optimization of that layer, unit cells of different sizes could be created by including varying numbers of water molecules. It was determined that 14 water molecules are needed to form the second hydration layer of the minimally hydrated unit cell at $d_{CC} \approx$ 7Å. After placing the extra water layer above the minimally hydrated array, VMD software [294] was used to rotate the extra water layer in order to attain a commensurate symmetry with the minimally hydrated array. Optimization was carried out for the two layer system of minimally hydrated array and extra water layer.

Two orientations of the additional water layer were distinguished. When the majority of free OH bonds in the extra water layer point away from the interface the configuration is referred to as “H up”. In the opposite case, it is referred to as “H down”. These orientations are shown in Figure. 6.20.

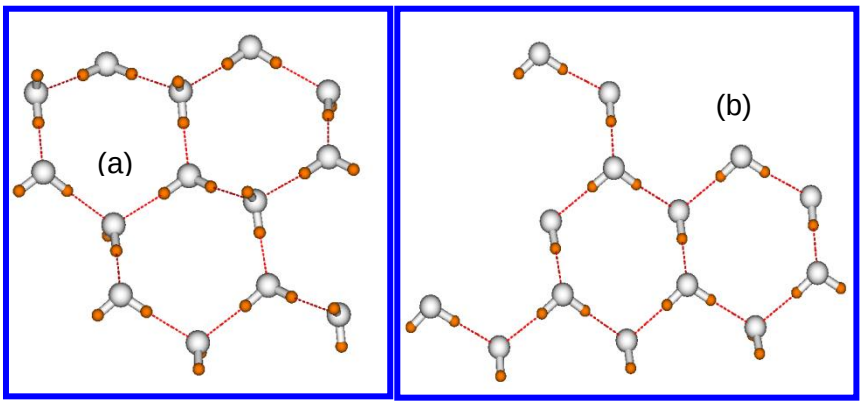

Figure 6.20: (a) "H up" and (b) "H down" orientations of additional water layer. In these representations, the minimally hydrated array of SGs would lie below the plane.

6.6.1. Geometry Optimization Results with Extra Water

Optimization was carried out with both upright and tilted conformations of the minimally hydrated array of 3 x [$CF_3SO_3H^{\cdot\cdot}H_2O$]. The separation distance of fixed end points of SG was varied in the range 6.3 Å < d_{CC} < 8.7 Å. Above d_{CC} > 7 Å, we know from plot of the formation energy vs. d_{CC} that the upright structure is not favoured. So, here the discussion will focus only on tilted structures with the addition of a monolayer of water to it.

We define the binding energy as:

$$BE = E_{TOT} - E_{WL} - E_{SG}. \qquad \textbf{6.12}$$

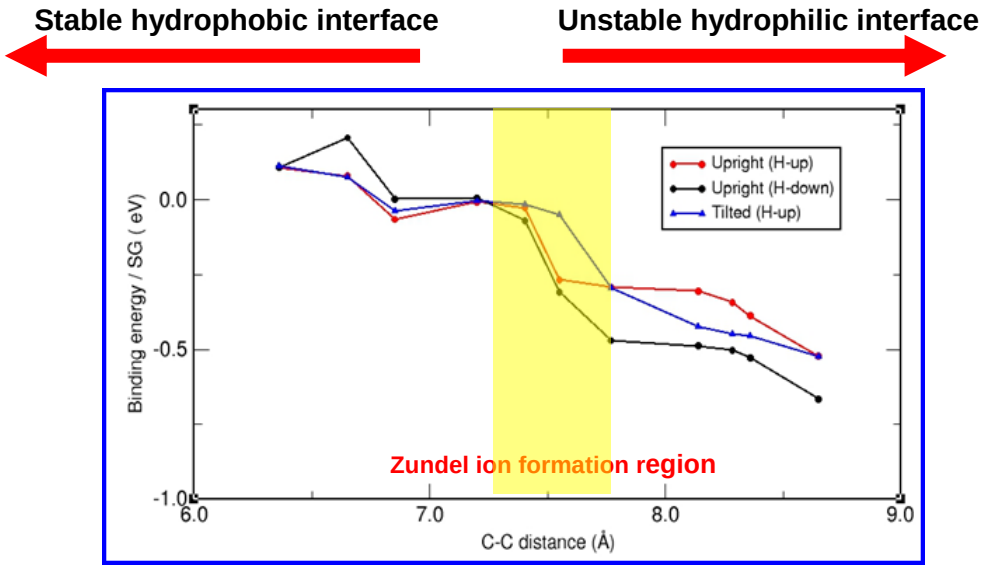

Figure 6.21: Binding energy of extra water layer per surface group as a function of d_{CC}

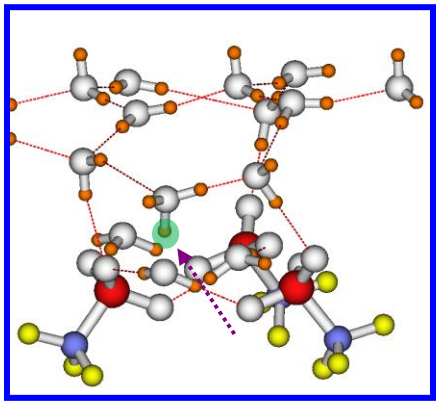

Figure 6.22: Tilted interface at d_{CC} = 7.9 Å with $d_{o\text{-}o}$ = 2.5 Å with proton transferred from the interface to the extra water layer and the interaction of the transferred proton with the interface is highlited.

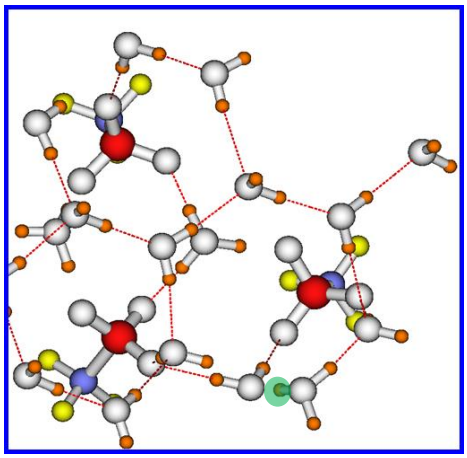

Figure 6.23: Extra water layer breaks up at d_{CC} = 8 Å implying instability at the extra water layer due to the transfer of proton from the interface.

The main results from the static calculations are:

1. When the separation between the surface groups is d_{CC}< 6.7 Å, highly ordered and fully ionized sulfonic acid groups and H_3O^+ form a 2D network of the interface in upright conformation.

2. Upon increasing the surface group separation $d_{CC,}$ a cluster-like "tilted" network forms at d_{CC} = 6.7 Å. This occurs with a sharp transition from weak binding of the additional water monolayer, with binding enrergy < 0.1 eV, to strong binding, with binding energy > 0.6 eV.

3. For the tilted interface, we find transfer of a proton from the interface to the monolayer of water at the d_{CC}=7.9 Å as shown in Figure. 6.22.

4. Instability at the extra water layer is noted when the tilted interface is at d_{CC} ~ 8 Å, as shown in Figure 6.23.

From the above static calculations we infer:

I. Degeneracy of conformations at the interface was found at a critical surface group separation, d_{CC} = 6.7 Å.

II. Below this SG separation, we find that the interface is hydrophobic and above this separation the interface behaves hydrophilically upon addition of water molecule(s).

III. A similar situation arises in the case of biological membranes and in Langmuir monolayers where it was observed that, upon densification of surface groups the system undergoes a transition from hydrophilic to hydrophobic [213-221]

IV. In Langmuir monolayers, it was found that the rate of lateral proton transport depends on the nature of ionic groups at the interface as well as the distance between these groups. Due to difference in composition of monolayers, different pKa of ionic groups as well as experimental factors such as convective distrurbances, the reported values of proton diffusion coefficients were found to be in a range, 10^{-5} to 10^{-6} cm^2s^{-1} [209-212,]. Despite the range in experimental values, we believe that hydrogen bonded ionic groups at the SG/water interface can enable a very efficient mechanism of surface proton transport.

V. Experiments performed at bio-membranes in general focus on surface groups terminated by carboxylic acids.

VI. In order to elucidate the mechanism of proton transport in PEM at minimal hydration condition, at the interface, the surface groups (SGs) terminated with sulfonic acid is of interest.

VII. Matsui *et al* [237] studied the lateral conductivity using surface pressure and surface conductance experiments on nanosheet assemblies of monolayers with sulfonic acid terminated head groups. The conductivity was found to have a value of 1×10^{-2}S cm^{-1} at 70°C for the ordered multilayer. Though, this study is interesting, no conclusive mechanism in proton transport at the interface was provided.

VIII. Our studies can be evaluated by comparison to the recently published experimental studies on mesoporous silica terminated with sulfonic acid groups [304]. The measured proton conductivity was found to be about 5.4 $*10^{-3}$ S cm^{-1}. For the highest acid density of 2.3 mmol g^{-1} (1.41 groups/nm^2) with smallest pore size of 2.2 mm considered in this work at 25°C at RH =20 % with λ= 2, the activation energy of proton transport was found to be 0.26 eV. The activation energy of interfacial hydronium translocations found in our work is in a comparable range.

6.7 *Ab initio* Metadynamics Simulation

Further calculations were carried out in our group [300] performed utilizing *ab initio* metadynamics simulations at the DFT level using CP2K. This method implements mixed Gaussian and plane wave method (GPW) [301, 302]. Using this methodology the activation energy barriers and reaction pathways of relevant interfacial proton transitions were determined. The main interest in this simulation study was to understand whether the highly ordered and exceptionally stable array of densely packed SG could efficiently promote long-range proton transfer. An intuitive graphical representation of possible interfacial H_3O^+ ion transitions on the 2D two-component lattice at d_{CC}≈ 6.7 Å is presented in Figure 6.24.

In the *ab initio* metadynamics study two extreme scenarios corresponding to local defect-type and highly collective H_3O^+ ion transitions were evaluated. In both cases the initial structure was the perfectly ordered condensed state at d_{CC} ≈ 6.7 Å. The lateral H_3O^+ ion shift was selected as a single metadynamics collective variable (CV). For studies of local defect-type transitions, unit cells with 12 surface groups were considered. For collective transitions unit cells with 3 surface groups considered. Activation energy and reaction Helmholtz energies for the local defect-type transition are ΔF_a=0.6 eV and ΔF_r =0.5 eV (refer Figure 6.25a). The final state of this transition was

found to be metastable. On the other hand, for the collective transition, activation and reaction Helmholtz energies are ΔF_a=0.3 eV and ΔF_r =0.0 eV (refer Figure 6.25b). The value of ΔF_a for the collective transition is found to be 2-3 times larger than the activation energy of proton transport in bulk water (0.1 eV) this is explained based on the hydrogen bond strength. It is expected that the collective nature of hydronium ion translocations at the interface could give high total rates of proton transfer despite the higher activation energy. The possibility of this collective motion has been evaluated based on soliton theory of collective proton transfer in our model system in the next paper by Golovnev and Eikerling. The present metadynamics simulation show that using only one CV the highly improbable proton transfer obtained through static calculation with activation energy ~ 0.5 eV changes to one where the activation barrier for the transfer is ~ 0.3 eV. The collective nature of proton transfer helps in achieving high proton conductance. This simulation implies that concerted hydronium ion translocation reduce the activation energy (~0.3 eV) and that the concertedness depends on the coupling strength of hydrogen bonds as shown in Figure 6.24.

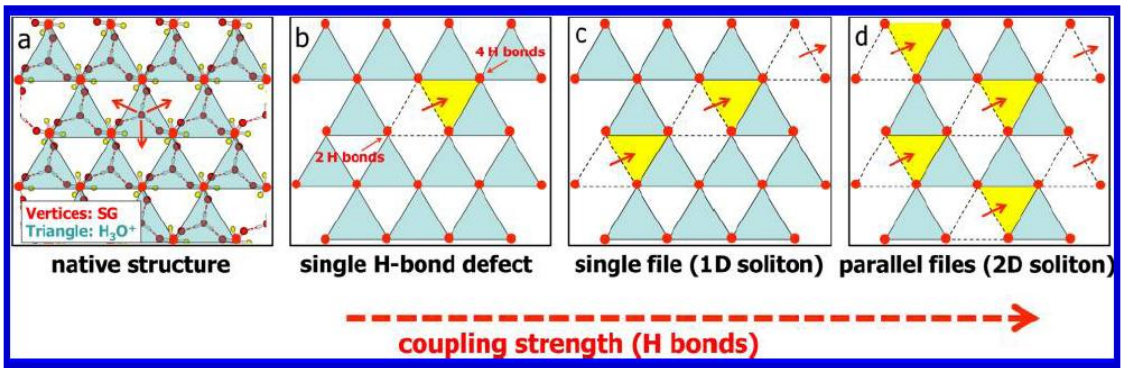

Figure 6.24: 2D component of $H_3O^+$and SO_3^- ions. (a) represents triangles with vertices as sulfonic acid groups and hydronium ions at the centre (b) creation of H-bond defect(c) single file proton transfer (1D soliton) (d) parallel file proton transfer (in plane 2D soliton). Reprinted with permission from S. Vartak, A. Roudgar, A. Golovnev, and M. Eikerling, *J. Phys. Chem. B* 2013, 117, 583. Copyright 2013. American Chemical Society.

(a)

(b)

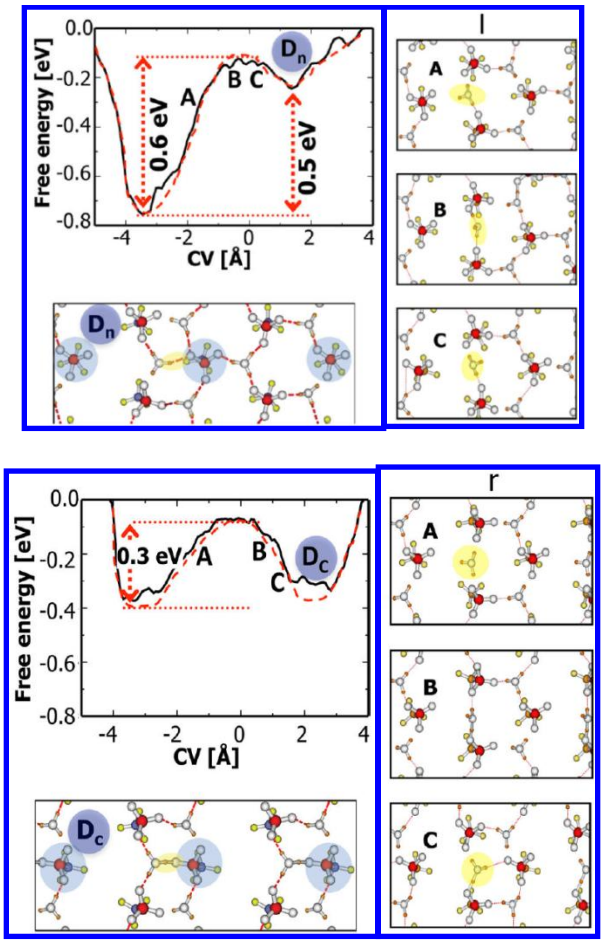

Figure 6.25: (a) Free energy surfaces for local defect type (left panel, l) and (b)collectiveH_3O^+ (right panel, r). Snapshots for the corresponding structures are shown in these panels and marked in free energy surfaces as well. Reprinted with permission from S. Vartak, A. Roudgar, A. Golovnev, and M. Eikerling, *J. Phys. Chem. B* 2013, 117, 583 Copyright 2013. American Chemical Society.

6.8. Soliton Theory

A theoretical study of collective proton transport in the 2D model system was presented in Ref [303]. In the high packing density of sulfonic acid surface groups, and under minimal hydration conditions, the stable interfacial conformations consists of two component lattice of hexagonally ordered sulfonate anions and interstitial hydronium cations. Considering that hydronium ion motion occurs as a travelling solitary wave analyzed microscopic parameters such as size of the soliton and concertedness of the

motion were analysed that depend strongly on the periodic potential created by surface groups, SGs. Kinetic properties of the solition such as energy and mobility were found to be independent of the potential profile. It is proposed in the paper that conductivity requires soliton statistics based on the properties of single soliton that is derived in this paper. The mechanism that might prevail at or under dry conditions is suggested. As the water content increases, different mechanism might prevail. It is also suggested that, soliton is very sensitive to the SG spacing and change in spacing might make one of the structures upright or tilted much less preferable that complicates the process. In conclusion, soliton mechanism is applicable when the membrane is at dry condition (~ $1H_2O$ / SO_3H) and at optimal surface group separation, at around 7 Å.

Chapter 7. Conclusions and Outlook

In this thesis, a simple model of a highly acid-functionalized interface was evaluated using *ab initio* molecular dynamics. The model system represents a hydrated array of protogenic surface groups as encountered at polymer-water interfaces in pores of polymer electrolyte membranes. The interfacial system is mapped onto a 2D array of surface groups, which is considered under minimal hydration and with hexagonal order of grafting points of the surface groups at a basal plane.

The main findings obtained is a structural interfacial transition to a condensed surface state with long-range order at high density of SGs. The structural transition is accompanied by a wetting transition from a hydrophilic surface state to a super hydrophic state upon densification of the minimally hydrated array.

Structural correlations at the interface have been explored and compared for systems with $CH_3SO_3^{-}\cdots H_3O^{+}$ and $CF_3SO_3^{-}\cdots H_3O^{+}$. The study on effect of different chemical groups we found qualitatively similar results. Thus we conclude that, basic interfacial correlations and conformations are independent of the chemical nature of the polymeric sidechains.

Moreover, an increase in the length of SG was evaluated, by addition of CF_3 in the tails of SGs. The longest sidechain mimics Aquivion® ($CF_3OCF_2CF_2^{-}$). The main conclusion from this calculation is that the formation energy at the most stable conformation decreases slightly, while the range of 2D correlations extends to markedly reduced densities of surface groups with increasing length of SGs.

In the next part of this study $14H_2O$ molecules were added to the minimally hydrated interface. The extra water layer was considered in two different positions, "H-up" and "H-down", referring to the orientation of H positions of the extra water layer

relative to the minimally hydrated array underneath. We report the result of “tilted” structure which is stable above d_{CC} > 6.7 Å. In this study we find that, binding energy is found to be > 0.6 eV above d_{CC} > 6.3 Å and weak binding below d_{CC} < 6.3 Å with binding energy < 0.1 eV. This calculation ascertain that, the minimally hydrated interface is hydrophobic d_{CC} < 6.3 Å and hydrophilic when d_{CC} > 6.3 Å.

The optimization results obtained so far suggest that dense packing of acidic groups at the polymer-water interface in a polymer electrolyte membrane is critical to obtain acceptable proton conductivity under minimal hydration. In a related study, detailed *ab initio* molecular dynamics calculations have identified the molecular mechanism of an elementary proton exchange at a dense array of acid- functionalized surface groups. In that publication [299], concerted tilting-rotation modes of acidic head groups (SO_3H) were found to facilitate the lateral proton exchange. From this elementary step, we can assume that, long range proton transport under minimal hydration condition might involve such tilting-rotation modes of acidic groups.

The challenge at the theory front is to understand the interplay between long range proton transport at acid-functionalized interfaces and proton exchange between the interfacial SG and bulk water. If need be, further optimization could be performed for d_{CC} > 9Å for which the number of water molecules that should be added is ~16 from rough estimation.

A recently developed theory for soliton in our group at monolayers with densely packed surface groups was put forward by Golovnev and Eikerling [303]. They discussed the microscopic parameters of hydronium ion motion, such as soliton size and shape and described the concertedness of proton motion that depends strongly on the periodic potential created by acidic surface groups. Kinetic properties of the soliton such as energy and mobility were found to be independent of the potential profile. The proposed soliton mechanism ascertained to be advantageous over the individual hopping motion of hydronium ion at minimal hydration condition. Soliton motion is very sensitive to the density of the surface groups. Solitons could exist only on the surface at packing density close to the optimal value.

From our calculations and understanding of the system, we propose that dense packing of surface groups will enable high proton conductivity at minimal hydration condition and at critical distance of ~ 7Å.

All of our static simulation formed the basis for proposing the proton transport at the minimally hydrated interface as soliton-like in next papers from Swati *et al* [300] and by Golovnev *et al* [303].

In the paper of Swati *et al* [300], *ab initio* calculations using metadynamics technique, at the critical group density viz d_{CC} ~6.7 Å, strong hydrogen bonds in the network of H_3O^+ and SO_3^- ions enforce soliton-like motion of hydronium ions. This proposed mechanism is in line with various experimental observations of highly efficient concerted proton transport at charged monolayers. The obtained activation energy, ~ 0.3 eV is found to be in agreement with experimental data for minimally hydrated PEMs.

Strong interactions between water molecules can form a continuous 2D sheet of water that enable the proton transport at minimal hydration condition by reducing the proton potential barrier between water molecules of neighboring sulfonic acid sites. This conductivity can also be realized as soliton motion of H_3O^+ as proposed in our soliton theory by Eikerling *et al* [303].

Such studies can be realized in experiments using surface potential experiments of monolayer groups terminated with sulfonic acids by Matsui *et al* [237].

References

1. Fuel Cell Handbook, Fifth edition, U. S. Department of Energy, **2000**.

2. Physical Modeling of Materials for PEFCs: Michael H. Eikerling, and Kourosh Malek *Proton Exchange Membrane Fuel Cells: Materials Properties and Performance. CRC Press,* **2009***;* http://www.sfu.ca/eikerlingresearch/overview

3. D. E. Curtin, R. D. Lousenberg, T. J. Henry, P. C. Tangeman, M. E. Tisack. *J. Power Sources*, **2004**, 131, 41.

4. M. Mathias, H. Gasteiger, R. Makharia, S. Kocha, T. Fuller, T. Xie, and J. Pisco. *Prepr. Pap.Am. Chem. Soc., Div. Fuel Chem.,* **2004**, 49, 471.

5. B. S. Pivovar. *Polymer,* **2006**, 47, 4194.

6. D. Wei, W. Haijiang, Y. Xiao-Zi, M. J. Jonathan, Y. Daijun, Q. Jinli, and M. Jianxin. *Int. J. Hydrogen energy* **2009**, 34, 9461.

7. M. Watanabe, Y. Satah, and C. Shimura.*J. Electrochem. Soc*., **1993**, 140, 3190.

8. K. H. Choi, D. J. Park, Y. W. Rho, Y. T. Kho, and T. H. Lee. *J. Power Sources* **1998**, 74, 146.

9. R. Savinell, E. Yeager, D. Tryk, U. Landau, J. Wainright, D. Weng, K. Lux, M. Litt, and C. Rogers. *J. Electrochem. Soc.,* **1994**, 141, L46.

10. O. Savadogo, and B. Xing. *J. New Mat. Electrochem. Systems* **2000**, 3, 345.

11. M. A. Hickner, H. Ghassemi, Y.-S. Kim, B. R. Einsla, and J. E. McGrath. *Chemical Reviews* **2004**, 104, 4587.

12. B. Smitha, S. Sridhar, and A. A. Khan. *Journal of Membrane Science* **2005**, 259 10.

13. K.-D. Kreuer, S. J. Paddison, E. Spohr, and M. Schuster. *Chemical Reviews* **2004**, 104, 4637.

14. S. M. Haile. *Acta Materialia* **2003**, 51, 5981.

15. M. Schuster, T. Rager, A. Noda, K. D. Kreuer, and J. Maier. *Fuel Cells.* **2005**, 16. 355.

16. X. Zhou, Z. Chen, F. Delgado, D. Brenner, and R. Srivastava. *J. Electrochem. Soc*., **2007**, 154, B82.

17. J. A. Elliot, S. Hanna, A. M. S. Elliot, and G. E. Cooley. *Phys.Chem. Chem.Phys.* **1999**, 1, 4855.

18. J. A. Elliott and S. J. Paddison. *Phys.Chem. Chem.Phys.* **2007**, 9, 2602.

19. A. Vishnyakov and A. V. Neimark. *J. Phys. Chem.* **2001**, 105, 9586.

20. S. S. Jang, V. Molinero, T. Cagin, and W. A. Goddard, III. *J. Phys. Chem.* **2004**, 108, 3149.

21. A. Vishnyakov and A. V. Neimark. *J. Phys. Chem.* **2000**, 104, 4471.

22. E. Spohr, P. Commer, and A. A. Kornyshev. *J. Phys. Chem.* **2002**, 106, 10560.

23. W. Goddard, III, B. Merinov, A. van Duin, T. Jacob, M. Blanco, V. Monirelo, S. S.Jang, and Y. H. Jang. *Molecular Simulation.* **2006**, 32, 251–268.

24. S. Cui, J. Liu, M. E. Selvan, D. J. Keffer, B. J. Edwards, and W. V. Steele. *J. Phys. Chem. B.* **2007**,111, 2208.

25. R. Devanathan, A. Venkatnathan, and M. Dupuis. *J. Phys. Chem. B*. **2007**, 111 13006.

26. R. Devanathan, A. Venkatanathan, and M. Dupuis. *J. Phys. Chem. B*. **2007**, 111, 8069.

27. A. Venkatanathan, R. Devanathan and M. Dupuis. *J. Phys. Chem. B*. **2007**, 111, 7234.

28. P. G. Khalatur, S. K. Talitskikh, and A. R. Khokhlov. *Macro.Mol.Theory and Simu.* **2002**, 11, 566.

29. D. Y. Galperin, and A. R. Khokhlov. *Macro.Mol.Theory and Simu*. **2006**, 15, 137.

30. K. Malek, M. Eikerling, Q. Wang, Z. Liu, S. Otsuka, K. Akizuki and M. Abe*. J. Chem.Phys.* **2008**, 129, 204702.

31. J. A. Elliot, and S. J. Paddison. *Phys. Chem.Chem. Phys*. **2006**, 8, 2193.

32. S. J. Paddison. *Annu.Rev.Mater.Res*. **2003**, 33, 289.

33. G. A. Eisman. *J. Power Sources.* **1990**, 29, 389.

34. M. W. Verbrugge, and R. F. Hill. *J. Electrochem. Soc.,* **1990**, 137, 3770.

35. K. Strasser. *J. Power Sources.* **1992**, 37, 209.

36. T. A. Zawodzinski Jr., C. Derouin. S. Radzinski, R. J. Sherman, V. T. Smith, T. E. Springer and S. Gottesfeld. *J. Electrochem. Soc*., **1993**, 140, 1041.

37. M. Cappadonia, J. W. Ering, S. M. Saberi Niaki, and U. Stimming. *Solid State Ionics.* **1995**, 77, 65.

38. A. Ghielmi, P. Vaccarono, C. Troglia, and V. Arcella. *J. Power Sources.* **2005**, 145, 108.

39. T. D. Gierke, and W. Y. Hsu In Perfluorinated Ionomer Membranes: Eisenberg, A., Yeager H. L., ACS Symposium Series No. 180; *American Chemical Society*: Washington, DC, **1982;** Chapter 13, 283.

40. W. Y. Hsu, and T. D. Gierke. *J. Membr. Sci*., **1983**, 13, 307.

41. T. D. Gierke, G. E. Munn, F. C. Wilson. *J. Polym. Sci., Polym. Phys.,* **1981**, 19, 1687.

42. H. L. Yeager and A. Steck. *J. Electrochem. Soc.,* **1981**, 128, 1880.

43. E. Roche, J. M. Pineri, R. Duplessix, and A. M. Levelut. *J. Polym. Sci., Polym Phys. Ed*.,**1981**, 19, 1.

44. E. Roche, J. M. Pineri, R. Duplessix, A. M. Levelut. *J. Polym. Sci., Polym. Phys. Ed*., **1982**, 20,107.

45. M. Fujimura, T. Hashimoto, and H. Kawai. *Macromolecules.* **1981**, 14, 1309.

46. M. Fujimura, T. Hashimoto, and H. Kawai. *Macromolecules.* **1982**, 15, 136.

47. C. L. Marx, D. F. Caulfield, and S. L. Cooper. *Macromolecules.* **1973**, 6, 344.

48. W. J. MacKnight, W. P. Taggart, and R. S. Stein. *J. Polym. Sci., Part C.* **1974**, 45, 113.

49. E. J. Roche, R. S. Stein, T. P. Russell, and W. J. MacKnight. *J. Polym. Sci., Polym. Phys. Ed.,* **1980**, 18, 1497.

50. H. W. Starkweather. *Macromolecules* **1982**, 15, 752.

51. S. Kumar, and M. Pineri. *J. Polym. Sci., Polym. Phys. Ed.,* **1986***,* 24, 1767.

52. B. Dreyfus, G. Gebel, P. Aldebert, M. Pineri, M. Escoubes, and M. Thomas. *J. Phys. France.* **1990**, 51, 1341.

53. E. M. Lee, R. K. Thomas, A. N. Burgess, D. J. Barnes, A. K. Soper, and A. R. Rennie. *Macromolecules.* **1992**, 25, 3106.

54. P. Aldebert, B. Dreyfus, and M. Pineri. *Macromolecules.* **1986**, 19, 2651.

55. B. Loppinet, G. Gebel, and C. E. Williams. *J. Phys. Chem. B*. **1997**, 101, 1884.

56. B. Loppinet, and G. Gebel. *Langmuir.* **1998**, 14, 1977.

57. G. Gebel, and R. B. Moore. *Macromolecules.* **2000**, 33, 4850.

58. G. Gebel, and J. Lambard. *Macromolecules.* **1997**, 30, 7914.

59. L. Rubatat, A –L. Rollet, G. Gebel and O. Diat. *Macromolecules.* **2002**, 35, 4050.

60. L. Rubatat, G. Gebel, and O. Diat. *Macromolecules.* **2004**, 37, 7772.

61. F. P. Orifino, and S. Holdcroft. *J. New Mater. Electrochem. Syst.,* **2000**, 3, 287.

62. P. J. James, T. J. McMaster, J. M. Newton, and M. J. Miles. *Polymer.* **2000**, 41, 4223.

63. M. H. Kim, C. J. Glinka, S. A. Grot, and W. G. Grot. *Macromolecules.* **2006**, 39, 4775.

64. K. S. Rohr, and Q. Chen. *Nature Mat.,* **2008**, 7, 75.

65. K. S. Rohr. *J. Appl. Cryst.,* **2007**, 40, 16.

66. K. S. Rohr, and Q. Chen. *Macromolecules.* **2004**, 37, 5995.

67. K. S. Rohr, and Q. Chen. *Macromol. Chem. Phys.* **2007***,* 208, 2189.

68. P. Choi, N. H. Jalani, and R. Datta. *J. Electrochem. Soc.* **2005**, 152, E123.

69. Yu. M. Volfkovich, V. S. Bagotzky, V. E. Sosenkin, and E. I. Shkolnikov. *Sov. Electrochem.,* **1980**, 16, 1620.

70. Yu. M. Volfkovich, and V. S. Bagotzky. *J. Power Sources.* **1994**, 48, 327.

71. J. Divisek, M. Eikerling, V. Mazin, H. Schmitz, U. Stimming, and Yu. M. Volfkovich. *J. Electrochem. Soc.,* **1998**, 145, 2677.

72. H. L. Yeager and A. Steck. *Anal. Chem.,* **1979**, 51, 862.

73. A. Steck, and H. L. Yeager. *Anal. Chem.,* **1980***,* 52, 1215.

74. T. A. Zawodzinski, Jr., T. E. Springer, J. Davey, R. Jestel, C. Lopez, J. Valerio, and S. Gottesfeld. *J. Electrochem. Soc.,* **1993**, 140, 1981.

75. T. A. Zawodzinski Jr., M. Neeman, L. Sillerud, and S. Gottesfeld. *J. Phys.Chem.,* **1991***,* 95, 6040*.*

76. K. D. Kreuer. Solid State Ionics. **1997**,97,1.

77. J.-C. Perrin, S. Lyonnard, F. Volino, and A. Guillermo. *Eur.Phys.J-Special topics* **2007**, 141, 57.

78. J.-C. Perrin, S. Lyonnard, and F. Volino. *J.Phys.Chem.C.* **2007**, 111, 3393.

79. F. Volino, J.-C. Perrin, and S. Lyonnard. *J. Phys. Chem.B*. **2006**,110,11217.

80. http://www-llb.cea.fr/fr-en/activ05-06/p068-069.pdf

81. A. M. Pivovar and B. S. Pivovar. *J. Phys. Chem. B.* **2005**, 109,785.

82. D. Rivin, C. E. Kendrick, C. W. Gibson and N. S. Schneider. *Polymer* **2001**, 42, 623.

83. J-C. Perrin, S. Lyonnard, A. Guillermo,and P. Levitz. *J. Phys. Chem. B.* **2006***,* 110, 5439.

84. A-L. Rollet, J-P. Simonin, P. Turq, G.Gebel, R. Kahn, A. Vandais, J-P. Noël, C. Malveau, and D. Canet. *J. Phys. Chem. B.* **2001**, 105, 4503.

85. H. Yoshida, and Y. Miura. *J. Membr.Sci.,* **1992**, 68, 1.

86. M. Pineri, F. Volino, and E. Escoubes. *J. Polym. Sci., Polym.Phys. Ed.,* **1985**, 23, 2009.

87. M. Saito, K. Hayamizu, and T. Okada. *J. Phys. Chem. B.* **2005**, 109, 3112.

88. K. Nakamura, T. Hatekeyama, and H. Hatekeyama. *Polymer.* **1983**, 24, 871.

89. Y. S. Kim, L. Dong, M. A. Hickner, T. E. Glass, V. Webb, and J. E. McGrath. *Macromoleucles.* **2003**, 36, 6281.

90. A. Siu, J. Schmeisser, and S. Holdcroft. *J. Phys. Chem B.* **2006**, 110, 6072.

91. M. Cappadonia, J. W. Erning, and U. Stimming. *J. Electroanal. Chem.* **1994**, 376, 189.

92. P. Choi, and R. Datta. *J. Electrochem. Soc.,* **2003***,* 150, E601.

93. P. Choi, N. H. Jalani, and R. Datta. *J. Electrochem. Soc.,* **2005**, 152, E84.

94. A. Z. Weber, and J. Newman. *J. Electrochem. Soc*., **2003**, 150, A1008.

95. M. H. Eikerling, and P. Berg. *Soft Matter.* **2011**, 7, 5976.

96. A. Stassi, L. Gatto, E. Passalacqua, V. Antonucci, and A. S. Arico. *J. Power Sources.* **2011***,* 196, 8925.

97. M. Wakizoe, O. A. Velev, S. Srinivasan. *Elecrochim. Acta.* **1995***,* 40, 335.

98. M. Gebert, A. Ghielmi, L. Merlo, M. Corasaniti, and V. Arcella. *ECS Trans.,* **2009,** 26, 279.

99. J. Lin, Y. Liu, and Q. M. Zhang. *Polymer.* **2011**, 52, 540.

100. M. Emery, M. Guerra, G. Haugen, K. Hintzer, K. H. Lochhaas, P. Pham, D. Pierpnt, M. Schberg, A. Thaler, M. Yandrasits, and S. Hamrock. *ECS Trans*., **2007**, 11, 3.

101. K. D. Kreuer, M. Schuster, B. Obliers, O. Diat, U. Traub, A. Fuchs, U. Klock, S. J. Paddison, and J. Maier. *J. Power Sources.* **2008,** 178, 499.

102. P. L. Antonucci, A. S. Arico, P. Creti, E. Ramunni, V. Antonucci. *Solid State Ionics.* **1999**, 125, 431.

103. B. Baradie, J. P. Dodelet, D. Guay. *J. Electroanal. Chem*., **2000**, 489, 101.

104. K. A. Mauritz, I. D. Stefanithis, Garth L. Wilkes, Hao-Hsin Huang. *J. Appl. Polym. Sci.,* **1995***,* 55, 181.

105. R. V. Gummaraju, R. B. Moore and K. A. Mauritz. *J. Polym. Sci. B Polym. Phys.*, **1996**, 34**,** 2383.

106. W. Apichatachutapan, R. B. Moore and K. A. Mauritz. *J. Appl. Polym. Sci.,* **1996**, 62, 417.

107. P. L. Shao, K. A. Mauritz and R. B. Moore. *Chem. Mater.*, **1995**, 7, 192.

108. P. L. Shao, K. A. Mauritz and R. B. Moore. *J. Polym. Sci. B. Polym. Phys.*, **1996**, 34**,** 873.

109. M. Watanabe, H. Uchida, Y. Seki, M. Emori and P. Stonehart. *J. Electrochem Soc.,* **1996***,* 143**,** 3847.

110. M. Miyake, J. S. Wainright, and R. F. Savinell. *J. Electrochem. Soc.,* **2001***,* 148, A898.

111. W.G. Grot. *Chem. Ind.,* **1985**, 19, 647.

112. F. Wang, M. Hickner, Y. Seung Kim, T. A. Zawodzinski, J. E. McGrath. *J.Membr.Sci.* **2002**, 197, 231.

113. D. Poppe, H. Frey, K. D. Kreuer, A. Heinzel, and R. Mülhaupt. *Macromolecules.* **2002**, 35, 7936.

114. B. Lafitte, L. E. Karlsson, P. Jannasch. *Macromol. Rapid Commun*., **2002**, 23, 896.

115. Y. Z. Meng, S. C. Tjong, A. S. Hay and S. J. Wang. *J. Polym. Sci. Part A: Polym Chem.*, **2001**, 39, 3218.

116. L. Jörissen, V. Gogel, J. Kerres, J. Garche. *J. Power Sources.* **2002**, 105, 267.

117. C. Genies, R. Mercier, B. Sillion, N. Cornet, G. Gebel, and M. Pineri. *Polymer.* **2001**, 42, 359.

118. J. Wang , X. Yue , Z. Zhang , Z. Yang , Y. Li , H. Zhang , X. Yang , H. Wu , and Z. Jiang. *Adv. Funct. Mater*., **2012**, 22, 4539.

119. A. Roy, M. A. Hickner, X. Yu, Y. Li, T. E. Glass, and J. E. McGrath. *J. Polym.Sci. Part B: Polym. Phys.,* **2006**, 44, 2226.

120. Y. A. Elabd, E. Napadensky, C. W. Walker, and K. I. Winey. *Macromolecules.* **2006**, 39, 399.

121. M. J. Park, K. H. Downing, A. Jackson, E. D. Gomez, A. M. Minor, D. Cookson, A. Z. Weber, and N. P. Balsara. *Nano Lett.,* **2007***,* 7, 3547.

122. L. Rubatat, C. Li, H. Dietsch, A. Nykänen, J. Ruokolainen and R. Mezzenga. *Macromolecules* **2008**, 41, 8130.

123. L. Rubatat, Z. Shi, O. Diat, S. Holdcroft, and B. J. Frisken. *Macromolecules.* **2006**, 39, 720.

124. T. Saito, H. D. Moore, and M. A. Hickner. *Macromolecules.* **2010**, 43, 599.

125. M. J. Park, and N. P. Balsara. *Macromolecules.* **2008***,* 41, 3678.

126. B. Bae, K. Miyatake, and M. Watanabe. *ACS Appl.Mater.Int.,* **2009***,* 1, 1279.

127. F. S. Bates, and G. H. Fredrickson. *Phys. Today.* **1999**, 52, 32.

128. Z. Shi, and S. Holdcroft. *Macromolecules.* **2005***,* 38, 4193.

129. Y. Yang, Z. Shi, and S. Holdcroft. *Macromolecules.* **2004**, 37, 1678.

130. J. Gao, D. Lee, Y. S. Yang, S. Holdcroft, B. J. Frisken. *Macromolecules*. **2005**, 38, 5854

131. M. J. Park, and N. P. Balsara. *Macromolecules.* **2010**, 43, 292.

132. L. Chen, D. T. Hallinan, Jr. Y. A. Elabd, and M. A. Hillmyer.*Macromolecules.* **2009**, 42, 6075.

133. H. Uehara, M. Kakiage, M. Sekiya, T. Yamagishi, T. Yamanobe, K. Nakajima, T. Watanabe, K. Nomura, K. Hase, and M. Matsuda. *Macromolecules.* **2009***,* 42, 7627.

134. S. J. Paddison, and J. A. Elliott. *J. Phys. Chem.A.* **2005,** 109, 7583.

135. S. J. Paddison and J. A. Elliott. *Solid State Ionics.* **2006**, 177, 2385.

136. S. J. Paddison and J. A. Elliott. *Solid State Ionics.* **2007**, 178, 561.

137. H. Danneel. *Z. Elecktrochem.* **1905**, 11, 249.

138. E. HÜckel. *Z. Elecktrochem.* **1928**, 34, 546.

139. J. D. Bernal and R. H. Fowler. *J. Chem. Phys.,* **1933**, 1, 515.

140. M. Eigen and L. de Maeyer. *Proc. Roy.soc. of London Ser. A.* **1958**, 247, 505.

141. N. Bjerrum. *Science.* **1952**, 115, 385.

142. S. Scheiner. *Annu.Rev.Phys.Chem.,* **1994**, 45, 23.

143. K. Luth, and S. Scheiner. *J. Phys. Chem*., **1992**, 97, 7507.

144. M. J. Frisch, J. E. Del Bene, J.S. Binkley, and H. F. Schaefer III. *J. Chem. Phys.,* 1986, 84, 2279.

145. Y. Xie, R. B. Remington, and H. F. Schaefer III. *J. Chem. Phys.,* **1994**, 101, 4878.

146. M. D. Newton, and S. Ehrenberg. *J. Am.Chem.Soc.,* **1971**, 93, 4971.

147. M. D. Newton. *J. Chem. Phys*., **1977**, 67, 5535.

148. D. Marx. *ChemPhysChem.,* **2006**, 7, 1848.

149. A. J. Huneycutt, R. J. Saykally. *Science.* **2003**, 299, 1329.

150. E. Sphor, P. Commer, and A. A. Kornyshev. *J.Phys. Chem.,* **2002**, 106, 10560.

151. M. Eikerling, A. A. Kornyshev, and E. Spohr. *Adv. Polym. Sci.,* **2008**, 215, 15.

152. M. E. Tuckerman, D. Marx, M. L. Klein, M. Parrinello. *Science*. **1997**, 275, 817.

153. M. E. Tuckerman, K. Laasonen, M. Sprik and M. Parrinello. *J. Chem. Phys.,* **1995**, 103, 150.

154. D. Marx, M. E. Tuckerman, J. Hutter and M. Parrinello. *Nature.* **1999***,* 397, 601.

155. D. Marx, M. E. Tuckerman, M. Parrinello. *J. Phys. Condens. Matter*., **2000**, 12, A153.

156. C. J. D. von Grotthuss. *Ann. Chim. LVIII.* **1806**, 54.

157. N. Agmon. *Chem. Phys. Lett.,* **1995***,* 244, 456.

158. N. Agmon. *J. Phys. Chem.,* **1996**,100, 1072.

159. M. E. Tuckerman, K. Laasonen, and M. Parrinello. *Nature.* **2002**, 417, 925.

160. M. E. Tuckerman, K. Laasonen, M. Sprik and M. Parrinello. *J. Phys. Chem*., **1995**, 99, 5749.

161. C. Heitner-Wirguin. *J. Membr. Sci.,* **1996**, 120, 1.

162. G. Zundel. *Adv. Chem. Phys.,* **2000**,111, 1.

163. M. Eigen. *Angew. Chem. Int. Ed.,* **1964**, 3, 1

164. P. A. Giguère. *J. Chem. Educ.,* **1979**, 56, 571.

165. M. E. Tuckerman, K. Laasonen, M. Sprik and M. Parrinello. *J. Chem.Phys.,* **1995**, 103**,** 150.

166. A. Warshel, and R. M. Weiss. *J. Am. Chem. Soc.,* **1980**, 102, 6218.

167. U. W. Schmitt and G. A. Voth. *J. Phys. Chem. B* **1998**, *102*, 5547.

168. U. W. Schmitt and G. A. Voth. *J. Chem. Phys.* **1999**, *111*, 9361.

169. U. W. Schmitt and G. A. Voth. *Israel J. Chem.* **1999**, *39*, 483.

170. T. J. F. Day, U. W. Schmitt, and G. A. Voth. *J. Am. Chem. Soc.,* **2000**,*122*, 12027.

171. T. J. F. Day, A. V. Soudackov, M. Čuma, U. W. Schmitt, and G. A.Voth. *J.Chem. Phys.,* **2002**, *117*, 5839.

172. R. Vuilleumier, and D. Borgis. *J. Mol. Struct.,* **1997**, *436-437*, 555.

173. R. Vuilleumier, and D. Borgis. *J. Phys. Chem. B.* **1998**, *102*, 4261.

174. R. Vuilleumier, and D. Borgis. *J. Chem. Phys.,* **1999**, *111*, 4251.

175. R. Vuilleumier, and D. Borgis. *Israel J. Chem.,* **1999**, *39*, 457.

176. O. Markovitch, H. Chen, S. Izvekov, F. Paesani, G. A. Voth, and N. Agmon. *J. Phys. Chem. B.* **2008,** *112,* 9456.

177. M. E. Tuckerman, D. Marx, M. Parrinello. *Nature.* **1999**, 397, 601.

178. B. Winter, M. Faubel, I. V. Hertel, C. Pettenkofer, S. E. Bradforth, B. Jagoda-Cwiklik, L. Cwiklik, and P. Jungwirth. *J. Am. Chem. Soc.,***2006**, *128*, 3864.

179. B. Kirchner. *ChemPhysChem.,* **2007**, *8*, 41.

180. T. A. Zawodzinski Jr., M. Neeman, L. Sillerud, and S. Gottesfeld. *J. Phys.Chem.,* **1991**, 95, 6040.

181. S. J. Paddison, and J. A. Elliott. *J. Phys. Chem.A.* **2005,** 109, 7583.

182. S. J. Paddison. *J. New Mater. Electrochem. Syst*., **2001**, 4, 197.

183. M. Laporta, M. Pegoraro, and L. Zanderighi. *Phys. Chem. Chem. Phys.,* **1999**, 28, 4619.

184. M. Eikerling, S.J. Paddison, and T.A. Zawodzinski. *J. New Mater. Electrochem. Sys.,* **2002**, 5, 15.

185. J. Clark II, S.J. Paddison, M. Eikerling, M. Dupuis, Michel and T.A. Zawodzinski. *J. Phys. Chem. A.* **2012,** 116, 1801.

186. M. Eikerling and A.A. Kornyshev. *J. Electroanal. Chem.,* **2001**, 502, 1.

187. M. Eikerling, A.A. Kornyshev, A. M. Kuznetsov, J. Ulstrup, and S. Walbran. *J. Phys. Chem. B.* **2001**, 105, 3646.

188. M. Eikerling, S. J. Paddison, L. R. Pratt, and T. A. Zawodzinski. *Chem. Phys. Lett.,* **2003**, 368, 108.

189. R. Car, and M. Parrinello. *Phys. Rev. lett.,* **1985**, 55, 2471. http://www.cpmd.org/.

190. P. Hohenberg, and W. Kohn. *Phys. Rev. B.* **1964**, 136, 864.

191. W. Kohn, and L. Sham. *Phys. Rev. A.* **1965**, 140, 1133.

192. D. Marx, and M. Parrinello. *Z. Phys. B.* **1994**, 95, 143.

193. M. E. Tuckerman, D. Marx, M. L. Klein, and M. Parrinello. *J. Chem. Phys.,***1996**, 104, 5579.

194. M. E. Tuckerman. *J. Phys. Condens. Matter.* **2002**, 14, R1297.

195. J. B. Spencer, and J-O. Lundgren. *Acta. Cryst. B.* **1973**, 29, 1923.

196. R G. Delaplane, J-O. Lundgren, and I. Olovsson. *Acta. Cryst. B.* **1975**, 31, 2202.

197. J-O. Lundgren. *Acta. Cryst. B.* **1978**, 34, 2428.

198. R L. Hayes, S. J. Paddison, and M. E. Tuckerman. *J. Phys. Chem. B.* **2009**, 113, 16574.

199. R L. Hayes, S. J. Paddison, and M. E. Tuckerman. *J. Phys. Chem. A.* **2011**, 115, 6112.

200. E. Spohr, P. Commer, and A. A. Kornyshev. *J. Phys. Chem. B*. **2002**, 106, 10560.

201. S. Walbran, and A. A. Kornyshev. *J. Chem. Phys.,* **2001***,* 114, 10039.

202. P. Commer, A. G. Cherstvy, E. Spohr and A. A. Kornyshev. *Fuel Cells.* **2002***,* 2, 127.

203. M. Eikerling, A. A. Kornyshev, and U. Stimming. *J. Phys. Chem. B.* **1997**,101, 10807.

204. M. Eikerling, Yu. I. Kharkats, A. A. Kornyshev, and Yu. M. Volfkovich. *J.Electrochem. Soc.,* **1998**, 145, 2684.

205. M. Eikerling, A. A. Kornyshev, and E. Spohr. *Adv.Polym.Sci.* **2008**, 215, 15.

206. A. Y. Mulkidjanian, J. Heberle, and D. A. Cherepanov. *Biochim.Biophys. Acta.* **2006***,* 1757, 913.

207. J. Heberle, J. Riesle, and G. Thiedemann, D. Oesterhelt, and Norbert, A. Dencher. *Nature.* **1994**, 370, 379.

208. J. Zhang, and P. R. Unwin. *Phys. Chem. Chem. Phys*., **2002**, 4, 3814.

209. J. Zhang, and P. R. Unwin. *J. Am. Chem. Soc,.* **2002**, 124, 2379.

210. S. Serowy, S. M. Saparov, Y. N. Antonenko, W. Kozlovsky, V. Hagen, and P. Pohl. *Biophys. J.* **2003**, 84, 1031.

211. J. Teissie, M. Prats, S. Soucaille, and J. F. Tocanne. *Proc. Natl. Acad. Sci*., **1985**, 82, 3217.

212. A. Polle, and W. Junge. *Biophys. J.* **1989**, 56, 27.

213. V. B. P. Leite, A. Cavalli and O. N. Oliveira. Jr., *Phys. Rev. E.* **1998**, 57, 6835.

214. O. N. Oliveira, Jr. and A. Cavalli. *J. Phys. C.* **1993**, 5, A307.

215. P. Luckham, J. Wood, S. Froggatt, and R. Swart. *J. Colloid Interface Sci.,* **1993**, 156, 164.

216. E. Dupart, B. Agricole, S. Ravaine, C. Mingotaud, O. Fichet, P. Delhaes, H.Ohnuki, G. Munger, and R. M. Leblanc. *Thin Solid Films.* **1994**, 243, 575.

217. O. Befort, and D. Möbius. *Thin Sold Films.* **1994**, 243, 553.

218. T. Kondo, R. C. Ahuja, D. Möbius, and M. Fujihira. *Bull. Chem. Soc. Jpn.*, **1994**, 67, 315.

219. O. N. Oliveira, Jr. and C. Bonardi. *Langmuir*. **1997**, 13, 5920.

220. S. V. Mello, A. Riul, Jr., L. H. C. Mattoso, R. M. Faria, and O. N. Oliveira Jr., *Synth. Met.,***1997**, 84, 773.

221. C. J. L. Constantino, L. P. Juliani, V. R. Botaro, D. T. Balogh, M. R. Pereira, E. A. Ticianelli, A. A. S. Curvelo, and O. N. Oliveira, Jr., *Thin Solid Films.* **1996**, 284, 191.

222. P. M. Kiefer, V. B. P. Leite, and R. M. Whitnell. *Chem. Phys.***1995**, 33, 194.

223. O. Fichet, D. Ducharme, V. Gionis, P. Delhaès, and R. M. Leblanc. *Langmuir.* **1993**, 9, 491.

224. M. Taylor, H. Morgan, and O. N. Oliveira, Jr., *Biochim. Biophys. Acta.* **1991**, 1062, 149.

225. C.J. Slevin and P. R. Unwin. *J. Am. Chem. Soc.,* **2000**, 122, 2597.

226. Scanning Electrochemical Microscopy; A. J. Bard, M. V. Mirkin, Eds: M. Dekker: New York, **2001**.

227. A. J. Bard, F.-R. F. Fan, D. T. Pierce, P. R. Unwin, D. O. Wipf. *Science.* **1991**, 254, 68.

228. P. R. Unwin, and A. J. Bard. *J. Phys. Chem.* **1992**, 96, 5035.

229. A. Cavalli, and O. N. Oliveira Jr., *Rev. Sci. Instrum.,* **1995**, 66, 5567.

230. B. Gabriel and J. Teissiè. *Proc. Natl. Acad. Sci. USA* **1996**, 93, 14521.

231. R. C. Ahuja, P-L. Caruso and D. Möbius. *Langmuir.* **1993**, 9, 1534.

232. D. Bazeia, V. B. P. Leite, B. H. B. Lima, and F. Moraes. *Chem. Phys.Lett.* **2001**, 340, 205.

233. S. Pnevmatikos. *Phys. Rev. Lett.,* **1988**, 60, 1534.

234. J.-Z. Xu, and B. Zhou. *Phys. Lett. A.* **1996**, 210, 307.

235. D. Bazeia, J. R.S. Nascimento, and D. Toledo. *Phys. Lett. A.* **1997**, 228, 357.

236. U. Alexiev, P. Scherrer, R. Mollaaghababa, H. G. Khorana, and M. P. Heyn. *Proc. Natn.Acad. Sci. USA.* **1995**, 92, 372.

237. J. Matsui, H. Miyata, Y. Hanaoka, and T. Miyashita. *Appl. Mater.Interfaces.* **2011**, 3, 1394.

238. G. Gebel. *Polymer.* **2000**, 41, 5829.

239. G. Gebel, and O. Diat. *Fuel Cells*, **2005**, 5, 261.

240. A. S. Ioselevich, A. A. Kornyshev, and J. H. G. Steinke. *J. Phys. Chem. B.* **2004**, 108, 11953.

241. A. Vishnyakov, and A. V. Neimark. *J. Phys. Chem. B*. **2001**, 105, 9586.

242. M.F.H. Schuster, W. H. Meyer, M. Schuster, and K. D. Kreuer. *Chem. Mater.,* **2004**, 16, 329.

243. G. Scharfenberger, W. H. Meyer, G. Wegner, M. Schuster, K. D. Kreuer, and J.Maier. *Fuel cells.* **2006**, 6, 237.

244. Md. A. B. H. Susan, M. Yoo, H. Nakamoto, and M. Watanabe. *Chem Lett.,* **2003**, 32, 836.

245. D. A. Boysen, T. Uda, C. R. I. Chisholm, S. M. Haile. *Science*. **2004**, 303, 68.

246. T. Uda, and S. M. Hail. *Electrochem. Solid State Lett.,* **2005**, 8, A245.

247. L. Xiao, H. Zhang, E. Scanlon, L. S. Ramanathan, E. W. Choe, D. Rogers, T. Apple, B. C. Benicewicz. *Chem. Mater.,* **2005**, 17, 5328.

248. H. Ghassemi, J. E. McGrath, and T. A. Zawodzinski Jr., *Polymer.* **2006**, 47, 4132.

249. J. Ding, C. Chuy, and S. Holdcroft. *Macromolecules.* **2002**, 35, 1348.

250. A. Y. Mulkidjanian, J. Heberle, and D. A. Cherepanov. *Biochim.Biophys. Acta.* **2006**, 1757, 913.

251. J. Heberle, J. Riesle, and G. Thiedemann, D. Oesterhelt, and Norbert, A. Dencher. *Nature.* **1994**, 370, 379.

252. http://www.vasp.at/.

253. G. Kresse, and J. Hafner. *Phys. Rev. B.* **1993**, 47, 558.

254. G. Kresse, and J. Furthmüller. *Phys. Rev. B.* **1996**, 54, 11169.

255. G. Kresse, and J. Furthmüller. *Comput. Mater. Sci.,* **1996**, 6, 15.

256. P. G. Bolhuis, D. Chandler, C. Dellago, and P. L. Geissler. *Annu. Rev. Phys.Chem.,* **2002**, 53, 291.

257. C. Dellago, P. G. Bolhuis, and D. Chandler. *J. Chem. Phys.,* **1998**, 108, 9236.

258. E. Weinan, and E. V. Eijnden. *J. Stat. Phys.,* **2006**, 123, 503.

259. G. M. Torrie, and J. P. Valleau. *Chem. Phys. Lett.,* **1974***,* 28, 578.

260. G. Mills, H. Jonsson, and G. K. Schenter. *Surf. Sci.,* **1995***,* 324, 305.

261. S. J. Paddison, and J. A. Elliott. *Phys. Chem. Chem. Phys.,* **2006***,* 8, 2193.

262. M. Eikerling, S.J. Paddison, and T.A. Zawodzinski. *J. New Mater. Electrochem. Sys.,* **2002**, 5, 15.

263. A. Roudgar, S. P. Narasimachary, and M. Eikerling. *J. Phys. Chem B.* **2006**, 110, 20469.

264. S. P. Narasimachary, A. Roudgar, and M. Eikerling. *Electrochim. Acta.* **2008***,* 53, 6920.

265. A.-L Rollet, O. Diat, and G. Gebel. *J. Phys. Chem. B.* **2002**, 21, 3033.

266. D. Seeliger, C. Hartnig, and E. Spohr. *Electrochim. Acta.* **2005***,* 50, 4234.

267. N. W. Ashcroft, and N. D. Mermin, Solid State Physics. (Saunders College Publishing, 1976).

268. A. Kühnle, T. R. Linderoth, B. Hammer, and F. Besenbacher. *Nature.* **2002***,* 415, 891.

269. J. H. Larsen, and I. Chorkendorff. *Surf. Sci. Rep.,* **1999**, 35, 163.

270. Turkowski, A. Kabir, N. Nayyar, and T. S. Rahman*. J. Phys.: Condens. Matter.* **2010**, 22,462202*.*

271. Theoretical Surface Science, Axel Groß. **2009** Springer.

272. P. Hohenberg and W. Kohn. *Phys. Rev.,* **1964***,* 136, B864.

273. U. v. Barth, and L. Hedin. *J. Phys. C.* **1972**, 5, 1629.

274. R. O. Jones, and O. Gunnarsson. *Rev. Mod. Phys.,* **1989**, 61, 689.

275. M. C. Payne, M. P. Teter, D. C. Allan, T. A. Arias, and J. D. Joannopoulos. *Rev. Mod. Phys.,* **1992**, 64, 1045.

276. B. Hammer, L. B. Hansen and J. K. NØrskov. *Phys. Rev. B.* **1999***,* 59, 7413.

277. A. D. Becke. *Phys. Rev. A.* **1988***,* 38, 3098.

278. C. Lee, W. Yang, and R. Parr. *Phys. Rev. B.* **1988***,* 37, 785.

279. J. P. Perdew, J. A. Chevary, S. H. Vosko, K. A. Jackson, M. R. Pederson, D. J. Singh, and C. Fiolhais. *Phys. Rev B.* **1992**, 46, 6671.

280. J. P. Perdew, K. Burke, and M. Ernzerhof. *Phys. Rev. Lett.,* **1996***,* 77, 3865.

281. P. David Suresh Babu, S. Periandy, S. Mohan, S. Ramalingam, and B. G. Jaya Prakash. *Spectrochimi Acta Part A.* **2011***,* 78, 168.

282. D. R. Hamann, M. Schlüter, and C. Chiang. *Phys. Rev. Lett.,* **1979**, 43, 1494.

283. G. B. Bachelet, D. R. Hamann, M. Schlüter, and C. Chiang. *Phys. Rev. B.* **1982***,* 26, 4199.

284. L. Kleinman and D. M. Bylander. *Phys. Rev. Lett*., **1982**, 48, 1425.

285. R. Car, and M. Parinello. *Phys. Rev. Lett.,* **1985**, 55, 2471; http://www.cpmd.org/

286. H. Arstila, K. Laasonen, A. Laaksonen. *J. Chem. Phys.,* **1998**, 108, 1031.

287. N. Troullier, and J. L. Martins. *Phys. Rev. B.* **1991**, 43, 1993.

288. S. J. Paddison, L. R. Pratt, and T. A. Zawodzinski Jr., *J. Phys. Chem. A.* **2001***,* 105, 6266.

289. M. E. Tuckerman, K. Laasonen, M. Sprik and M. Parrinello. *J. Phys. Chem*., **1995**, 99, 5749.

290. N. Agmon. *J. Mol. Liquids.* **1995***,* 64, 161.

291. Y. Zhang, and Z.Xu. *American Mineralogist.* **1995***,* 80, 670.

292. R. A. Pierotti. *J. Phys. Chem.,* **1963,** 67, 1840.

293. A. H. Narten, and H. A. Levy. *Science.* **1969***,* 165, 447.

294. http://www.ks.uiuc.edu/Research/vmd/

295. A. Laio, M. Parrinello. *Lecture Notes Phys.,* **2006**, 703, 315.

296. P. M. Morse. *Phys. Rev.,* **1929**, 34, 57.

297. M. Molski, and J. Konarski. *Phys. Rev. E.* **2003**, 68, 21916.

298. S. Gejji, K. Hermansson, and J. Lindgren. *J. Phys. Chem.,* **1993**, 97, 6986.

299. A. Roudgar, S. P. Narasimachary and M. Eikerling. *J. Chem. Phys. Letts*., **2008** 457, 347.

300. S. Vartak, A. Roudgar, A. Golovnev, and M. Eikerling. *J. Phys. Chem. B.* **2013**, 117, 583.

301. http://www.cp2k.org

302. J. VandeVondele, J. Hutter, M.Krack, F. Mohamed, M. Parrinello, and T. Chassaing. *J. Comput. Phys. Commun*., **2005**, 167, 103.

303. A. Golovnev, and M. Eikerling. *J. Phys.: Condens. Matter.* **2013**, 25, 045010.

304. S. Fujita, A. Koiwai, M. Kawasumi, and S. Inagaki. *Chem. Mater*., **2013**, 25, 1584.

.

.